2016

Geologic Extremes of the NW Himalaya: Investigations of the Himalayan Ultra-high Pressure and Low Temperature Deformation Histories

Dennis Girard Donaldson
Louisiana State University and Agricultural and Mechanical College

GEOLOGIC EXTREMES OF THE NW HIMALAYA: INVESTIGATIONS OF THE HIMALAYAN ULTRA-HIGH PRESSURE AND LOW TEMPERATURE DEFORMATION HISTORIES

A Dissertation

Submitted to the Graduate Faculty of the
Louisiana State University and
Agricultural and Mechanical College
in partial fulfillment of the
requirements for the degree of
Doctor of Philosophy

in

The Department of Geology and Geophysics

by
Dennis G. Donaldson Jr.
B.S., Virginia State University, 2009
August 2016

Dedicated to Jaime, Eliya, Noah, my siblings and parents.

ACKNOWLEDGEMENTS

I am very pleased that I have had a rewarding journey during this chapter of my life with the Department of Geology and Geophysical at Louisiana State University. I would not be here right now if it wasn't for Dr. Alex Webb, Dr. Barb Dutrow, Dr. Phil Bart, and the many other colleagues and friends I've had the great fortune of meeting.

I would like to thank the Louisiana State Board of Regents, as well as the National Science Foundation for funding my research. Words cannot express my gratitude.

I would like to thank Rick Young, Andrew Kylander-Clark, Brad Hacker and Carrie Menold for assisting and providing valuable guidance throughout my research.

I extend my appreciation to my fellow graduate students, Dian He, Cindy Colon, and the many undergraduates who have been in our cluster.

Finally, I would like to express my deep love and gratitude to my wife Jaime, my daughter Eliya and my son Noah.

TABLE OF CONTENTS

ABSTRACT

This dissertation focuses on two extremes of orogenic development in the Himalaya: the timing of early ultra-high pressure related tectonics and the subsequent emplacement of the high grade Greater Himalayan Crystallines.

The Himalayan orogeny is one of if not the best example of ongoing collisional systems, marked by the ongoing convergence of the Indian and Asian continents. The presence of coesite in the Tso Morari complex respresents subduction of the Indian continental crust to ultrahigh-pressure (UHP) conditions. However, the timing of UHP metamorphism is debated, creating an uncertainty in the calculation of subduction and exhumation rates. Petrologic and geochronologic analyses of eclogitic zircon and rutile from two samples—a kyanite bearing white mica schist and a garnet-biotite schist were conducted to constrain the timing and duration of the UHP metamorphic event. Titanite analyses from quartzofeldspathic gneiss constrain timing of exhumation and record the regional amphibolite-facies metamorphism. Petrology and U-Pb analyses and observations reveal peak metamorphic histories in rutile-bearing metapelites. Ages in rutile bearing samples are 50.3 ± 0.85 Ma and 47.60 ± 0.52 Ma. This geochronology provides insight into the suite of geochronometers already published in previous Tso Morari studies, but additional thermobarometry is needed to strongly correlate potential UHP ages with UHP conditions.

How the Greater Himalayan Crystalline was emplaced; and how much shortening was accomplished since the initial collision are debated. Three models; the Channel Flow model, Tectonic Wedging and Wedge extrusion models all have specific predictions of the spatial setting of the Greater Himalayan Crystalline relative to overlying stratigraphy. Here we show that the emplacement of the Greater Himalayan Crystalline is consistent with the predictions of

Tectonic Wedging through structural mapping and sampling. The shortening budget of the Himalaya experiences approximately a 2,000 km deficit between plate convergence and crustal shortening recorded in the geologic record. It has recently been proposed in the Greater Indian Basin model that this can be attributed by 2675 ± 700 km of North-South extension of the Greater Indian margin in the late Mesozoic. The extension resulted into creating a Tethyan subcontinent that collided with Asian around 50 Ma followed by India around 25 Ma. Our field mapping is inconsistent with the two collision sequence predicted by the Greater Indian Basin hypothesis. Additionally the amount of shortening predicted by the Greater Indian Basin hypothesis greatly exceeds the shortening recorded by our line-length balancing of the Tethyan stratigraphy.

CHAPTER 1: INTRODUCTION

1.1 UHP Metamorphism

Ultrahigh pressure metamorphism is characterized by the subduction of continental rocks to coesite stable depths of at least 2.7 GPa or 90km (Chopin, 1984; O'Brien et al., 2001). Observed at convergent plate boundaries, UHP metamorphic terranes develop through the ongoing subduction of oceanic crust followed by collision and subduction of island arcs and continents. The occurrence of UHP material has been found and collectively recognized in many places; West Greenland; Qingling, China; Western Gneiss Region, Norway; Bohemian Massif, Poland; Dabie-Sulu, China; Tso Morari, India; Kaghan Valley, Pakistan; Dora Maira, Italy and much more. In these instances felsic material is subducted to UHP depths. While it is unknown how much resides in the mantle, a significant amount exhumes and outcrops in the upper crust along with mafic material from the mantle. The process of eclogitization is responsible for the occurrence of most mafic material. It is characterized by the metamorphic facies change where plagioclase is no-longer stable in mafic rocks. The absence of plagioclase should be replaced by the presence of jadeite and quartz. True eclogites should have garnet along with pyroxene, typically with jadeite and omphacite end-members (Bucher and Grapes, 2011). Though the occurrence of eclogite and coesite are diagnostic, they are not the only indicators of UHP metamorphism. Microdiamonds with the stability of over 150km at depth have been located in the Bohemian Massif and Lago di Cignana, Italian Western Alps (Liou et al., 2014). In Kaghan Valley, Si-rich phengite indicates UHP conditions through phase equilibrium modelling (Wilke et al., 2010). In addition to the diagnostic mineral species and phase equilibria that indicate UHP metamorphism, certain minerals can be used as geochronometers to constrain the timing of metamorphic events in the UHP path. Zircon has been the most successful geochronometer due

to its refractory nature and high closure temperature, approaching 1000 ºC depending on grain size (Cherniak, 2000). It has been successfully employed as a geochronometer in Kaghan Valley, NW Himalaya Pakistan, as it hosted a coesite inclusion. Spot dating close that inclusion gave an UHP age of ~46 Ma (Kaneko et al., 2003). The successful constraint of UHP metamorphism has implications for constraining other phenomena, such as the timing of collision between convergent boundaries (Leech et al., 2005). This is of particular importance in Tso Morari, NW Himalaya India, where the timing of UHP is debated.

1.2 Himalayan UHP Metamorphism

Remnants of UHP metamorphism in the Himalaya occurs along strike and ~10km south of the Indus Suture Zone on the Indian continent. As discussed above the timing of UHP metamorphism in Kaghan Valley is constrained at 46 Ma while the timing of UHP metamorphism at Tso Morari is debate between ~53, ~50 and ~46 Ma (Leech et al., 2005, St-Onge et al., 2013, Donaldson et al., 2013). Under the premise that UHP timing can be used to constrain the collision timing of convergent boundaries, Himalayan UHP and collision timing falls into two endmembers, synchronous and anachronous. Determination between the two gives insight of the dynamics of Himalayan UHP metamorphism, collision timing and possibly geometry. In Chapters 1 we investigate the timing of UHP metamorphism of Tso Morari by the use of eclogitic zircon. In Chapter 2 we look to further constrain the UHP timing of Tso Morari by using rutile and titanite as geochronometers in metapelitic and eclogitic rocks.

1.3 Himalayan Orogenesis

1.3.1 Shortening and Development

Shortening is a term derived through the processes of contractional tectonics. Measured shortening quantifies the amount of horizontal compressive deformation accommodated by the

crust or lithosphere. Shortening can be accomplished on the outer layers of the lithosphere, which is known as thin-skinned deformation. However deep thick-skinned tectonics can incorporate basement rocks in the orogenic process. The Himalayas is a thin-skinned orogen created through the continent-continent collision of India and Asia which also shows signs of thick-skinned tectonics through the involvement of high grade metamorphic rocks (It involves three tectonostratigraphic groups and two major faults, the Lesser Himalayan Sequence (LHS), the Greater Himalayan Crystallines (GHC) and the Tetyhan Himalayan Sequence (THS) (Le Fort, 1975). The Lesser Himalaya Sequence consist of low-grade metamorphic rocks. The Greater Himalaya Crystallines are a complex consisting of high grade gneisses, pelites. The Tethyan Himalaya Sequence consists of rocks derived from marine sedimentation during the prominence of the Tethyan sequence prior to collision (Le Fort, 1975). The two faults divide these rocks into their sequential packages. The division between LHS and the GHC is accomplished by the Main Central Thrust (MCT). The South Tibet Detachment (STD) defines the diffuse boundary between the GHC and the THS (Yin, 2006).

1.3.2 Two Collision Greater Indian Basin Model

The idea that subducted India may be partially comprised of oceanic plate was developed by van Hinsbergen et al. (2012) into the two-collision model (or “Greater India basin” model-GIB). In this model, a “Tibetan Himalaya” plate consisting of the Tethyan Himalayan Sequence plus most or all of the Greater Himalayan Crystalline complex rifted from northern India in the Early Cretaceous. The rifting produced the oceanic Greater India basin between the two plates. The Tibetan Himalaya plate collided with Asia at ca. 50 Ma, followed by collision of the Lesser Himalaya with the amalgamated Tibetan Himalaya and Asia at 25-20 Ma. The suture zone of this

second collision must be cryptic, but is predicted to occur within the lower Greater Himalayan Crystalline complex and/or Main Central thrust zone.

A means of testing this model are structural balancing. This approach is to identify opportunities to measure un-appraised, large Himalayan shortening and integrate results into the geological shortening budget. The eastern Ladakh – Chamba region offers two such opportunities. First, Himalayan shortening budgets might greatly increase if ultrahigh-pressure terranes and overlying thrust sheets developed in the early collision are incorporated into balancing efforts. Preliminary quantifications of shortening across relevant areas – Tso Morari (in eastern Ladakh) and Kaghan Valley (Pakistan) regions - suggest 100s of km increases to Himalayan shortening budgets (Guillot et al., 2003; Leech et al., 2005). Unfortunately these efforts are schematic and have suffered from large uncertainties in basic kinematics (e.g., cf. O'Brien, 2006 vs. Leech et al., 2006), and perhaps for these reasons have been neglected (e.g., Long et al., 2011a; van Hinsbergen et al., 2011a). Second, current balanced sections across the superstructure, i.e., the Tethyan Himalayan Sequence, only span the northern portions of these rocks (e.g., Ratschbacher et al., 1994; Corfield and Searle, 2000; Murphy and Yin, 2003). Shortening estimates across this unit may be doubled by detailed work across its southern portions. To investigate the GIB model structural mapping was conducted along a continuous portion of the Tethyan Himalayan sequence. Further insights on this research and other methodologies are discussed in further detail in Chapter 4.

1.3.3 Models of Himalayan Development

The Himalayan strucuture consists of three units separated by two faults. The outter most unit is the Tethyan Himalayan Sequence and consists of low-grade sedimentary rocks. The interior component, the Greater Himalayan Crystalline Complex (GHC) consists of higher grade

crystallines. Remarkably below the GHC is the Lesser Himalayan Sequence which is another low grade sedimentary sequence. This geometry is positioned in a way that it follows the infrastructure concept proposed by Culshaw et al., (2006). Three tectonic models, Wedge Extrusion; Channel Flow; and Tectonic Wedging all propose different processes as responsible for the emplacement of the infrastructure 1) Wedge extrusion models show these rocks extruded southwards between the superstructure and the Indian craton (now represented by the subsequently accreted Lesser Himalayan Sequence) as a northward-tapering wedge (Burchfiel and Royden, 1985). The South Tibet detachment is a normal fault during this extrusion. Many recent workers associate these kinematics with critical taper – Coulomb wedge theory (e.g., Robinson et al., 2006; Kohn, 2008; Zhang et al., 2011), which suggests that normal faulting may occur during collapse of over-thickened thrust wedges (e.g., Davis et al., 1983; Dahlen, 1990). 2) In channel flow – focused denudation models, the high grade rocks tunnel southwards during the Eocene- Oligocene, a process driven by the lateral pressure gradient created by the gravitational potential difference between the Tibetan plateau and its margins (e.g., Beaumont et al., 2001; 2004; Godin et al., 2006). During this stage the South Tibet detachment is sub-horizontal and could perhaps be considered a crustal-scale backthrust. Subsequently this material is exhumed by enhanced erosion across a narrow zone where precipitation is focused along the topographic front of the orogen (e.g., Beaumont et al., 2001; Hodges et al., 2001; Clift et al., 2008). During this second, extrusive phase, the South Tibet detachment is a normal fault. 3) Tectonic wedging models show southwards emplacement of the Greater Himalayan Crystalline rocks entirely below the Earth surface (Yin, 2006; Webb et al., 2007; 2011a). The South Tibet detachment is a backthrust, and current exposure of high grade rocks results from post-early/middle Miocene erosion and footwall deformation. Therefore unlike other models, this model lacks an extrusive

phase. Model kinematics may be comparable to the early tunneling phase of channel flow, albeit with different timing (early to middle Miocene vs. Eocene-Oligocene motion). The same approach used to investigate the viability of the GIB model above is useful to investigate the three Himalayan development models. Structural mapping, along with other methodologies are discussed in more detail in chapter 3.

CHAPTER 2
PETROCHRONOLOGY OF ULTRAHIGH-PRESSURE HIMALAYAN ECLOGITE

2.1 Introduction

The Himalaya represent the front of the India-Asia collision, and are dominantly composed of material scraped off the subducting Indian plate (Yin, 2006) (Figure 2.1). Closure of the Tethys Ocean, which separated the two continents, involved accretion of multiple intraoceanic arcs, and possibly microcontinents, before culminating in continent-continent collision (Mahéo et al., 2004; van Hinsbergen et al., 2011a). At least 12 phenomena have been proposed to indicate the initial collision of India and Asia (see reviews by Rowley, 1996; Yin and Harrison, 2000; Guillot et al., 2003; Najman, 2006; van Hinsbergen et al., 2011a): (1) cessation of marine sedimentation or change in sedimentary style; (2) mixing of Indian and Asian detritus; (3) sediment from one plate deposited on the other; (4) deposition of one sedimentary unit on both plates; (5) ultrahigh-pressure (UHP) metamorphism of Indian supracrustal rocks; (6) slowing of plate convergence; (7) reorganization of some or all of the global plate circuit; (8) equivalence of paleolatitudes of northernmost precollisional India with southernmost precollisional Tibet; (9) transfer of fauna from one plate to the other; (10) emplacement of mélange; (11) change of characteristics in upper plate magmatism; and (12) shortening of the northern Indian margin. Dating these phenomena has yielded interpreted collision ages ranging from 70 to 35 Ma; most workers favor ages of ca. 55–50 Ma. An outstanding question regarding the initiation of collision is how its timing varied along strike. Constraints on the timing of UHP metamorphism suggest that subduction of Indian crust began ~7 m.y. later in the northwest than it did in the southeast (dates of ca. 46 Ma at the Kaghan Valley, Pakistan, versus ca. 53 Ma at Tso Morari, a lake in Ladakh, India; Kaneko et al., 2003; Leech et al., 2005). However, dates from Tso Morari have little petrogenetic information to

support their connection to eclogite facies metamorphism (O'Brien, 2006). In order to better constrain the timing of UHP metamorphism at Tso Morari, we present coupled U/Th-Pb and rare earth element (REE) data from 108 analyses of 103 zircons in 2 eclogites.

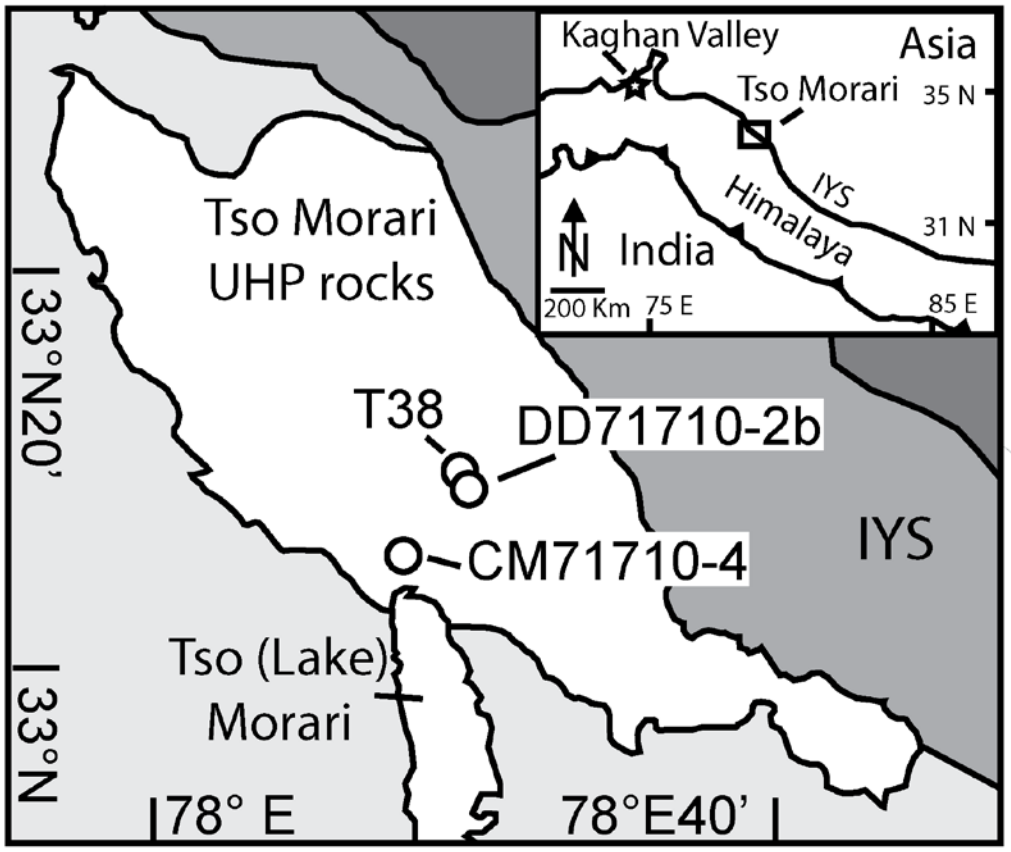

Figure 2.1. Sample location map, Tso Morari, India. Inset shows ultrahigh-pressure (UHP) locations in the Himalaya. ISZ—In- dus-Yarlung suture separating Indian and Asian rocks; KV—Kaghan Valley; TM—Tso Morari; PK—Pakistan; NP—Nepal; MFT— Main Frontal thrust; LB—Ladakh Batholith; THS—Tethyan Himalayan Sequence. Sample T38 is a quartzofeldspathic gneiss dated by Leech et al. (2005); sample L08–03A is a mafic eclogite sample analyzed by St- Onge et al. (2013); samples CM71710–4 and DD71710–2b are eclogites analyzed in this study. GPS coordinates for DD71710–2B and CM71710–4 are 33°08.959′N, 078°21.439′E and 33°07.230′N, 078°17.090′E, respectively. Map modified from Epard and Steck (2008).

2.2 Geologic Setting and Petrology

UHP rocks occur in two locations south of the Indus suture zone, which separates Indian and Asian rocks: in the Kaghan Valley of northern Pakistan, and north of Tso Morari in northwestern India (Figure 2.1). Ultrahigh pressures are confirmed by preserved coesite (O'Brien et al., 2001; Sachan et al., 2004). UHP rocks crop out within dominantly felsic Indian supracrustal rocks (e.g., de Sigoyer et al., 2004; Wilke et al., 2010a). Pressure-temperature histories of the two UHP terranes are remarkably similar (e.g., Wilke et al., 2010a): (1) UHP conditions of ~2.7–3.6 GPa, 640–760 °C, (2) cooling during initial decompression to ~0.9–1.7 GPa, 500–640 °C, and (3) reheating at ~0.8–1.2 GPa, 650–720 °C. However, the timing of UHP metamorphism at the two sites may differ.

Two scenarios have been advanced: UHP metamorphism at 47–46 Ma at both localities (e.g., Kaneko et al., 2003; O'Brien, 2006; Wilke et al., 2010b), or 47–46 Ma at Kaghan Valley and 54–53 Ma at Tso Morari (e.g., Leech et al., 2005, 2007; Guillot et al., 2007). The Kaghan Valley UHP event is well constrained at 46.2 ± 0.7 Ma (2 [illegible]Pb dating of zircon rims containing coesite inclusions (Kaneko et al., 2003). This is supported by a thermal ionization mass spectrometry date of 46.4 ± 0.1 Ma from eclogite zircon, a multipoint allanite Th-Pb isochron of 46.4 ± 0.9 Ma, and 40Ar/39Ar phengite plateau dates of 47.3 ± 0.3 Ma and 47.5 ± 0.5 Ma (Parrish et al., 2006, Wilke et al., 2010b). Despite multiple efforts, similarly straightforward dates have not been obtained for Tso Morari UHP rocks. Sm-Nd garnet-glaucophane–whole rock, Lu-Hf garnet–omphacite–whole rock, and U-Pb allanite dating all yielded 55 Ma dates for interpreted UHP mineral growth, but with large uncertainties of 7–17 m.y. (de Sigoyer and Chavagnac, 2000). Analyses (15) of metamorphic zircon rims from a quartzofeldspathic gneiss yielded a range of dates with clusters at 53.3 ± 0.7 Ma (3 analyses),

50.0 ± 0.6 Ma (5 analyses), and 47.5 ± 0.5 Ma (Leech et al., 2005, 2007), but interpretation of these dates is controversial (O'Brien, 2006; see Figure DR1 in the Appendix).

The apparent difference in the time of UHP metamorphism between Kaghan Valley and Tso Morari may indicate diachronous collision of an irregular Indian margin with a >500 km promontory (Guillot et al., 2007), or separate accretion events (Lister et al., 2001; White and Lister, 2012), of which only the younger may represent collision. Alternatively, the existing geochronology permits that the Kaghan and Tso Morari UHP metamorphism both occurred ca. 47 Ma (Kaneko et al., 2003; O'Brien, 2006) and might together signal continent-continent collision.

2.3 Methods

Methods U–Pb zircon petrochronology was performed at the University of California, Santa Barbara LASS lab (http://sites.google.com/site/icpgeolucsb/) using a Nu Plasma HR MC-ICPMS, a Nu AttoM SC-ICPMS (Nu Instruments Ltd., Wrexham, UK) and an Analyte 193 excimer ArF laser-ablation system equipped with a HeLex sample cell (Photon Machines, San Diego, USA). The analytical setup is described in Table 1. The ablated aerosol is carried by He from the sample cell to a mixing bulb in which the sample + He is mixed with Ar to stabilize the aerosol input to the plasma. The He-Araerosol is immediately split upon exiting the mixing bulb, with approximately half the ablation stream directed to each ICPMS. Laser energy is set to 4 mJ, which, once transmitted into the sample chamber, equates to ~0.1 μm/pulse; repetition rate is set to 4 Hz; single-ablation duration was 20–25 seconds; and spot diameters ranged from 12-14 μm with depths of ~8 μm. U–Pb dates were obtained with the Nu Plasma, equipped with four low-mass side electron multipliers for simultaneous measurement of 208Pb, 207Pb, 206Pb and 204Pb; 238U and 232Th were measured on Faraday cups equipped with 1011-ohm resistors. The

Nu AttoM was used in "E-Scan" mode to measure REE and Hf concentrations. Because standard analyses are matrix-matched (see below), internal standardization was unnecessary. Sample analyses were preceded by a 10-second baseline measurement, and unknown analyses were corrected with the 91500 zircon standard (Wiedenbeck et al. 1995) every 7 measurements (~5 min.). For quality control, the zircon reference material GJ1 (601 Ma, Jackson et al., 2004) was run after each 91500 analysis, and yielded a 06Pb/238U age of 609.8 ± 2.5 Ma (n = 34; MSWD = 1.5; in-run error). The Plešovice reference material (Slama et al., 2008) was also analyzed throughout the analytical session and yielded a concordia age of 337.6 ± 0.9 Ma (n = 27; MSWD = 0.76; in-run error). Post-data processing was performed using Iolite (Paton et al., 2010), and concordia plots were produced with Isoplot (Ludwig, 2003).

2.4 Petrochronology

To address the uncertainty in UHP timing, U/Th-Pb and REE zircon data were acquired via laser ablation–split-stream inductively coupled plasma–mass spectrometry (for analytical methods see the Data Repository). This approach enables analysis of U/Th-Pb ratios and REE abundances from the same volume of material. In situ analyses were obtained from thin sections of samples CM71710–4 and DD71710–2b, collected ~10 km apart in the Tso Morari UHP terrane (Figure 2.1). Both samples consist of garnet, omphacite, phengite, rutile, quartz, zoisite, amphibole, and sodic augite–plagioclase symplectite, with trace phases of zircon, pyrite, and titanite after rutile (Figure DR2). Inclusion-rich idioblastic pale red garnet cores record prograde metamorphism; the UHP and initial decompression periods described here are primarily evinced by (1) inclusion-poor colorless garnet rims and omphacite, and (2) sodic augite–plagioclase symplectite, respectively (Figure DR2) (cf. de Sigoyer et al., 1997; O'Brien, 2006; Konrad-Schmolke et al., 2008). Analyses were obtained from matrix zircon (33% of analyses) and zircon

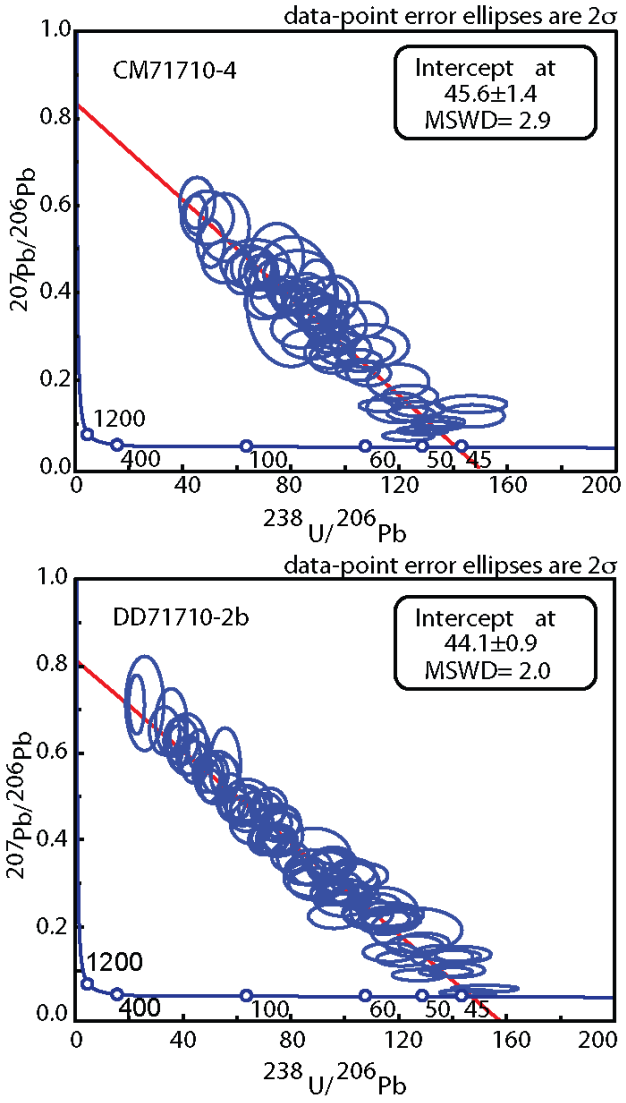

Figure 2.2. Zircon isochron dates. Tera- Wasserburg concordia plots of U-Pb data uncorrected for common Pb. Lower inter- cept dates of best-fit lines through all data are noted in the upper right. MSWD—mean square of weighted deviates.

included in UHP garnet (15%), omphacite (49%), and other phases (3%) (Figure DR2; Table DR1). Cathodoluminescence images of zircons in both samples reveal complex zoning, indicating protracted zircon growth (Figure DR3). Zircons in both samples are typically 12–30 µm across, necessitating a laser spot size of ~12–14 µm. Because of the small laser spot size, the

uncertainty on the 206Pb/238U ratio of the secondary standards was 5%; this error was added in quadrature to each analysis.

U-Pb isotopic results (Table DR1) are reported in Tera-Wasserburg concordia plots (Figure 2.2), as well as histograms and relative probability functions of 207Pb-corrected dates (Ludwig, 2009) (Figure 2.3).

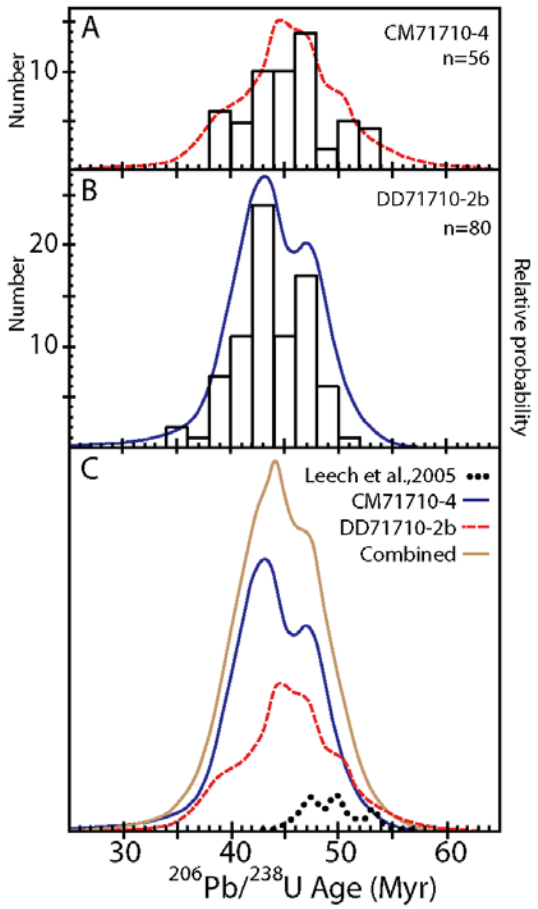

Figure 2.3. U-Pb zircon dates. Probability density functions (PDFs) and histograms of 238U/206Pb dates (207Pb-corrected). Dates are concordia lower intercept dates along the line extending from common Pb through each datum. A: CM71710–4. Green line is PDF curve, n is number of analyses, histogram bin size is 2 Ma. Assumed value for common 207Pb/206Pb = 0.838 is taken from the fit in Figure 2, and is indistinguishable from the Stacey-Kramers (1975) model value. B: DD71710–2b. Blue line is PDF curve, n is number of analyses, histogram bin size is 2 Ma, common 207Pb/206Pb = 0.806 (using the Stacey-Kramers model value of 0.838 changes the spot dates by an average of<1.6m.y.).C:PDFs for both samples, individually and combined (orange curve), T38 from Leech et al. (2005) (dotted line, n = 15), and for zircons analyzed in mafic eclogite sample L08–03A from St-Onge et al. (2013) (light-blue dotted curve).

Data are plotted as chondrite-normalized values (Figure 2.4) and are reported in Table DR2. Because the analyzed zircons are small and have low U concentrations (median value = 53 ppm), the radiogenic/common Pb ratios are relatively low. As a consequence, each sample yields an array of analyses distributed between common Pb (207Pb/206Pb = 0.838 for CM71710–4 and 0.806 for DD71710–2b) and concordia. The samples have low Th/U ratios (□0.35) and simi individual REE patterns. The 207Pb-corrected dates for CM71710–4 and DD71710–2b span ca. 53–37 Ma, peaking ca. 47–43 Ma (Figure 2.3). The mean square of weighted deviates (MSWD) values of the weighted mean dates for CM71710–4 (45.3 ± 1.6 Ma, MSWD = 3.4, n = 47) and DD71710–2b (44.2 ± 1.2 Ma, MSWD = 2.4, n = 61) (Figure 2.2) indicate that the analyses do not represent single populations. Aside from a few anomalies, the REE patterns for both samples display similar characteristics, a distinct lack of a Eu anomaly and flat heavy REE slopes (Figure 2.4).

2.5 Discussions and Conclusions

The ca. 53–37 Ma range and ca. 47–43 Ma peak of 207Pb-corrected dates of the 108 U-Pb zircon analyses (Figure 2.3) represent protracted zircon growth or recrystallization. This is demonstrated by the elevated MSWD values for the weighted mean date of both samples (Figure 2.2) and the complex zircon zoning patterns (Figure DR3). Most of the dates likely reflect UHP and/or prograde zircon (re)crystallization because (1) the REE data indicate (re)crystallization in the presence of garnet and absence of plagioclase (Figure 2.4; Table DR2), and (2) 64% of the dates were obtained from zircon included in garnet and omphacite (Figure DR2; Table DR1). The zircon dates are not correlated with their textural setting (e.g., as matrix grains or included grains) (Figure DR4). We interpret the upper limit of the date peak (i.e., ca. 47 Ma) as the oldest age of UHP metamorphism at Tso Morari.

The much smaller Kaghan Valley data set reported by Kaneko et al. (2003) has coesite included in zircon rims with a Tera-Wasserburg intercept age of 45.9 ± 0.73 Ma (MSWD = 2.3, n = 8). The remarkable similarity in the geochronologic data between the Tso Morari and Kaghan Valley eclogites, coupled with the coesite inclusion record from Kaneko et al. (2003) and the REE chemistry and textures of the Tso Morari zircons, indicates generally synchronous subduction of the two Himalayan UHP sites. Eclogite facies metamorphism lasted from ca. 47 to 43 Ma. This eliminates the need to explain a >5 m.y. difference in UHP timing using models featuring multiple accretion events or an irregular northern margin of India (e.g., Guillot et al., 2007; White and Lister, 2012). If UHP metamorphism occurs along the leading edge of a continental margin, it will postdate initial continent subduction by ~1–4 m.y., depending on convergence velocity and subducting slab dip (Kaneko et al., 2003; Guillot et al.,; Leech et al., 2005; Table DR3). Therefore, the Himalayan UHP record is consistent with initiation of Indian subduction at 51–47 Ma. The timing of the India-Asia collision initiation is a key parameter for models of Himalayan-Tibetan orogenic evolution (e.g., Beaumont et al., 2001), post collisional shortening estimates from plate circuit reconstructions (van Hinsbergen et al., 2011b), tectonics-linked climatic shifts (Raymo and Ruddiman, 1992; Kutzbach et al., 1993), drainage evolution of Asian river systems (Brookfield, 1998), paleo-ocean water chemistry and currents (Garzanti et al., 1987; Raymo et al., 1988; Beck et al., 1998), and faunal exchange between the continents (Clyde et al., 2003). The proposed ages of the initiation of collision range from 70 to 35 Ma (see reviews discussed herein), and it is possible that multiple continental fragments were accreted during this time (White and Lister, 2012; van Hinsbergen et al., 2012). All of the evidence for a pre–50 Ma collision can be interpreted to record arc accretion (e.g., Cai et al., 2011; van Hinsbergen, 2011b). Initial collision as young as 35 Ma is precluded by plate circuit

reconstructions (Dupont-Nivet et al., 2010; van Hinsbergen et al., 2011a).

A ca. 50 Ma India-Asia collision is supported by the cessation of marine sedimentation, paleomagnetic reconstructions, the deposition of Asia-sourced sediment on the Indian plate, and mixing of Indian and Asian detritus (Zhu et al., 2005; Najman et al., 2010; van Hinsbergen et al., 2011b; Wang et al., 2011). Previous interpretations of Himalayan UHP metamorphism involved an ~7 m.y. interregnum between a ca. 53 Ma event at Tso Morari and a ca. 46 Ma event at Kaghan Valley (Kaneko et al., 2003; Leech et al., 2005) that was interpreted to reflect

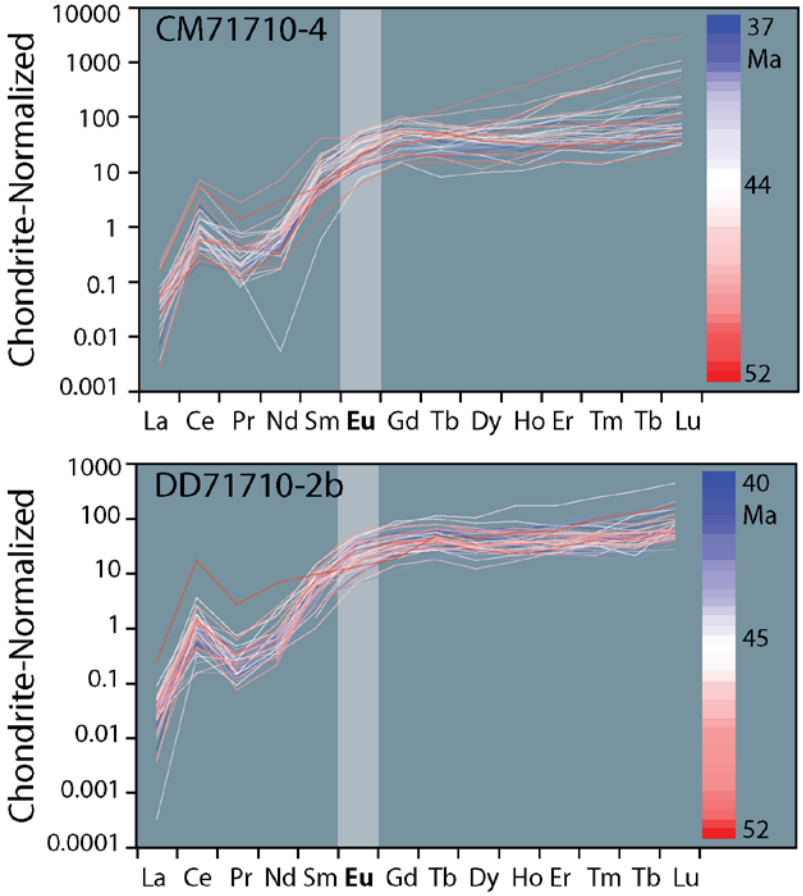

Figure 2.4. Rare earth element diagrams. Colors represent associated U-Pb data. Blue dates are older, red are younger.

continental subduction of a jagged Indian margin (Guillot et al., 2007) or separate accretion events (White and Lister, 2012). Our documentation of a single phase of eclogite facies metamorphism at these 2 localities separated by ~450 km instead is consistent with the initiation of northwest India-Asia collision synchronously along the margin ca. 50 Ma.

CHAPTER 3
INVESTIGATION OF MULTI-STAGE METAMORPHISM: TSO MORARI, NW HIMALAYAN GEOCHRONOLOGY

3.1 Introduction

3.1.1 Ultra-high Pressure Metamorphism in the Western Himalaya

The subduction of continental rocks to depths of 90 km or more where coesite is stable defines, in part, ultrahigh-pressure metamorphism (UHP) and is prevalent in convergent tectonic boundaries worldwide (e.g., Chopin, 1984; Smith 1984; Wang et al., 1989; de Sigoyer et al., 1997; O'Brien et al., 2001). Because the rocks in some UHP terrains represent the leading edge of continental subduction—constraining the timing of UHP metamorphism may also help constrain the timing of continental subduction and exhumation.

UHP terrains have compelling characteristics, some of which are explained by models that group UHP terrains by size (e.g., Kylander-Clark et al., 2012); mechanism of exhumation (e.g,, Hacker and Gerya, 2013); and exhumation rate (e.g., Kylander-Clark et al., 2013; Hacker and Gerya, 2013). Published exhumation rates at Tso Morari vary, from as slow as 7 mm/a as fast as 140 mm/a (Table 1).

Table 1: Convergence and exhumation rate estimations from previous UHP Himalayan workers

	Convergence	Peak Pressure	Peak Temperature	Exhumation	Peak Metamorphic Timing
de Sigoyer et al., 2004	>100 mm/a	>20 kbar	550 ± 50 °C	7 - 1.2 mm/a	
Leech et al., 2005	69 mm/a	>27 kbar	>750 °C		~53 Ma
St-Onge et al., 2013		25.5-27.5 kbar	630-645 °C	12 mm/a	~50 Ma
Donaldson et al., 2013					~46 Ma
Wilke et al., 2015		44-48 kbar	560-760 °C	90-140 mm/a	

The Tso Morari Gneiss dome is situated in the Tso Morari UHP terrane, located near Ladakh, NW India, approximately 10 kilometers southwest of the Indus-Yarlung suture zone (Figure 3.1). This UHP terrane is fault bounded by Tethyan Sequence on its southern flanks, while on its northern flanks it is bounded by ophiolites and the Ladakh batholith.

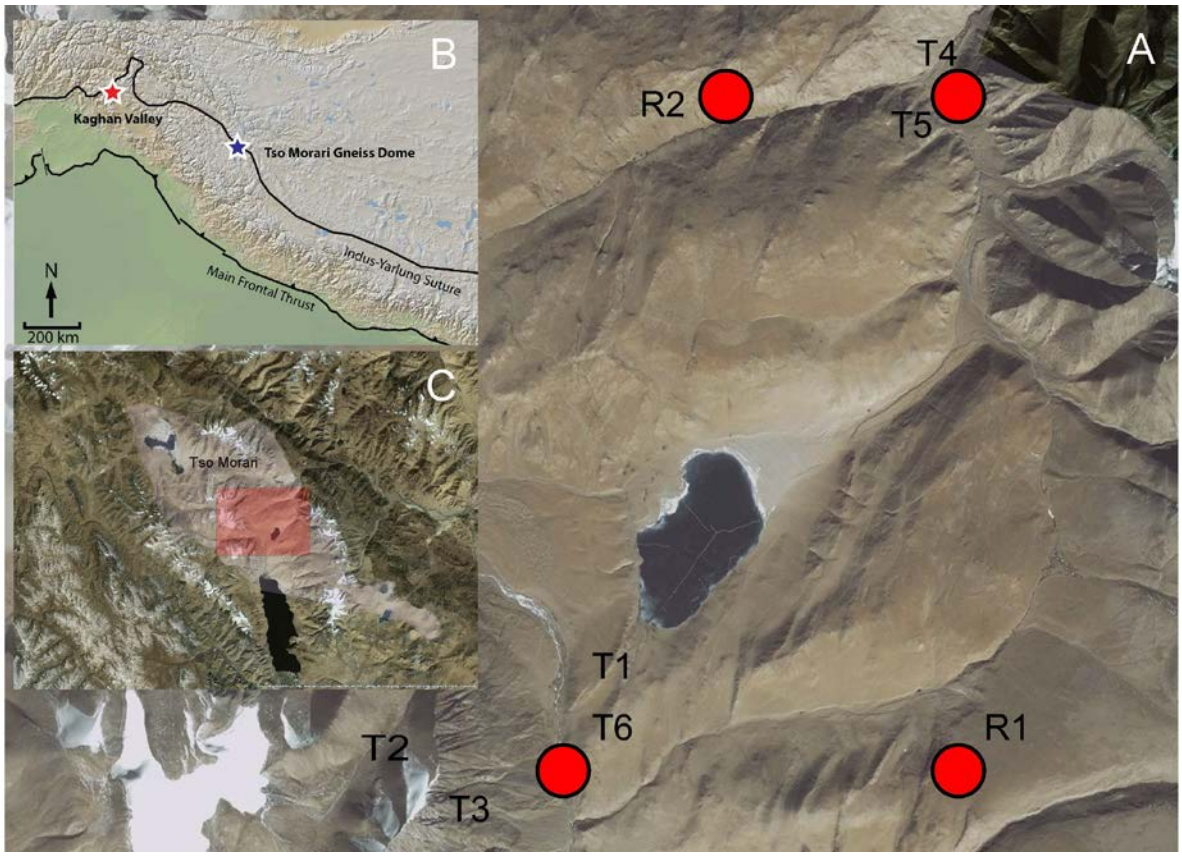

Figure 3.1 A) Map of Tso Morari Gneiss Dome. Red circles are sample locations B) Location of Kaghan Valley and Tso Morari, C) Zoomed image of Tso Morari

It is composed of crystalline rocks of the Cambro-Ordovician gneiss sequence with protolith affinity to the Haimanta/Phe formation of the Tethyan Sequence (e.g. Epard & Steck, 2008; Wilke et al., 2015). Low-grade metamorphosed rocks include greywacke, carbonates, slates and relatively undeformed granite. Mafic eclogite occurs sparsely throughout the terrane, hosted by quartzo-feldspathic gneiss. Most of the information describing UHP metamorphism in

Tso Morari is derived from mafic eclogite that is accessible near roads (Leech et al., 2005; St-Onge et al., 2013; Donaldson et al., 2013; Wilke et al., 2015). The Tso Morari Gneiss dome, and its pressure-temperature-time (P-T-t) history, provides insight into the UHP metamorphism along the Himalaya front.

3.1.2 Previous P-T Calculations

The P-T conditions of the Tso Morari Gneiss Dome have been studied extensively (Girard & Bussy, 1999: de Sigoyer et al., 2000; Schlup et al., 2003; Leech et al., 2005, O'Brien, 2006; St-Onge et al., 2013; Donaldson et al., 2013; Wilke et al., 2015). Two heating events have been proposed, one at UHP conditions and a retrograde event at lower pressures. Prograde metamorphism has been determined to have a maximum age of 58.0 ± 2.2 Ma from the U/Pb analyses of zircon inclusions in garnet cores from mafic eclogite where the host garnet recorded a pressure of 21.5 ± 1.5 kbar and temperature of 535 ± 15 °C (St-Onge et al., 2013). Other peak (UHP) conditions calculated vary over a range: 20 ± 2 kbar at 550 ± 50°C (Guillot et al., 1997), 20 ± 3 kbar at 580 ± 60°C (de Sigoyer et al., 1997), 25.5-27.5 kbar at 630-645 °C (St-Onge et al., 2013), >28 kbar at >640 °C (Sachan et al., 2004), >28 kbar at 700–800 °C (Mukherjee & Sachan, 2001), to >39 kbar at >750 °C (Mukherjee et al., 2003; Mukherjee & Sachan, 2009), 44-48 kbar at 560-760 °C (Wilke et al., 2015). These pressures naturally divide interpreted depth of UHP metamorphism into two groups, 100 km and ~150km.

Using various mineral assemblages from,eclogite, metapelites and gneiss, a retrograde overprint has been estimated at 9 ± 3 kbar and 610 ± 70°C (de Sigoyer et al., 1997), 630 ± 30 °C (Guillot et al., 1997) and ~12 kbar and ~750 °C (Mukherjee & Sachan, 2009), 7-13 kbar and 665-755 °C (St-Onge et al., 2013), 12-17 kbar and 550-750 °C (Wilke et al, 2015). Although conditions determined for retrograde metamorphism vary among previous workers, a prominent

feature in the mafic eclogites is a retrograde reheating event that occurs during a second stage of amphibole crystallization around ~44 Ma (de Sigoyer et al., 2000, Wilke et al., 2015). This event is interpreted to be coincident with a slowing in exhumation rate as Tso Morari settled at midcrustal depths (ibid).

Calculations from an isochemical phase diagram in St-Onge et al. (2013), predict a thermal maximum of 725 ± 50°C for amphibolite facies metamorphism in the host gneiss. This temperature is consistent with the thermal history predicted from eclogite samples from the same sampling location (de Sigoyer et al., 2000, St-Onge et al., 2013, Wilke et al., 2015). The eclogites in this particularly popular sampling location are the only lithology to have recorded the reheating event. Remarkably, in the Kaghan Valley, Pakistan, a similar reheating event has been recorded in what rocks with the growth of second stage amphibole and ilmenite after rutile (Wilke et al., 2010b).

3.1.3 Previous Geochronology

The timing of UHP metamorphism in Tso Morari Gneiss dome in the NW Himalaya (Figure 1), which records UHP metamorphism, is subject to debate. Previous work has suggested three different age interpretations for timing of UHP metamorphism: (1) U/Pb SHRIMP analyses of zircon separates from quartzofeldspathic gneiss yield an age of 53.3 ± 0.7 Ma, which is interpreted as timing of peak pressure (Leech et al., 2005); (2) U/Pb SHRIMP analyses of in-situ zircon from a mafic eclogite yield an age of 50.8 ± 1.4 Ma (St-Onge et al., 2013); and (3) coupled *in situ* U-Pb and REE, LA-ICP-MS analyses of zircon from mafic eclogites give an UHP age estimate around ~46 Ma (Donaldson et al., 2013). These UHP ages vary over a 7 Ma period, beyond the error of any analyses. In contrast, the UHP terrain in Kaghan Valley, Pakistan, has UHP metamorphism well-constrained at 46.2 ± 0.7 Ma from the U-Pb analyses of zircon rims

hosting coesite (Kaneko et al., 2003). The new UHP P-T estimates from Wilke et al., (2015) along with the different proposed UHP timings, suggest cooling rates up to 210 °C/Ma (Table 1).

Constraining the UHP timing in Tso Morari terrane may help constrain: (1) If the timing of UHP metamorphism across the Himalaya from where to where was a contemporaneous event or varied along the front which has implications for tectonic models of collision and subduction; (2) the burial and exhumation rates of the Tso Morari UHP rocks; and (3) the geometry of the initial collision and early development of the NW Himalaya. This study attempts to refine both timing and duration of subduction and exhumation of the Tso Morari terrane by obtaining U-Pb ages from rutile and titanite.

3.1.4 Rutile and Titanite Geochronology

Rutile (TiO_2) and titanite ($CaTiSiO_5$) both contain U and Pb that can be used for age dating (Mezger et al., 1991, Spencer et al., 2013). Dating the metamorphic rutile and titanite may provide information to constrain the UHP age at Tso Morari. Studies in the Western Gneiss Region, Norway show that rutile and titanite closure temperatures can effectively bracket the timing of UHP metamorphism (Kylander-Clark et al., 2008). Large mineral grains retain their Pb more readily and thus have a higher closure temperature than smaller grains (e.g., Cherniak, 1993; Kylander-Clark et al., 2008; Spencer et al., 2013). Therefore, ages from large grains should reflect the crystallization age and not the cooling age if the system remained closed. The cooling age of a mineral is interpreted as the time when it passes through its nominal closure temperature (Dodson, 1973). For 100 μm radius rutile and titanite grains cooling at 50°C/Ma, the closure temperatures are 686 ± 45°C and 635 ± 30°C respectively (Warren et al., 2012). The closure temperature of Pb in rutile is similar to the peak temperature recorded at Tso Morari, but pressures used to calibrate the diffusion of Pb in rutile was significantly less at 1 atmosphere

(Cherniak, 2003). It is possible that rutile is more resistant to Pb loss through volume diffusion at high to ultra-high pressures requiring higher closure temperatures. This is presented in the Arrhenius pressure dependent equation in Fick's Law, where diffusivity may decrease with increasing pressure. If higher closure temperatures are required, the rutile in Tso Morari may represent crystallization with respect to the published P-T estimates.

To investigate whether a similar history to Khagan Valley is documented in Tso Morari, rutile and titanite are dated from varying rock types to determine their crystallization or cooling age. Using the data presented below, we suggest the timing of UHP metamorphism and provide exhumation rates of Tso Morari.

3.2 Geologic Background

3.2.1 Lithologic Descriptions and Petrography

Samples were initially investigated using a petrographic microscope to determine mineralogy, textures, overprinting relationships, alteration features and identify samples containing rutile and titanite or further study rutile was analyzed from rocks R1 and R2, while titanite was analyzed from rock samples T1-T6 (Figure 2).

Sample R2 is white-mica schist consisting of kyanite, zircon, clinopyroxene, white micas, rutile, and quartz (Figure 3.2a-f). Oxides are present sporadically and occur over the 200µm scale. White mica is dominant in R2, 500µm thick layers of white mica are common throughout the sample and define a foliation (Figure 3.2C). Kyanite is subhedral to anhedral, with the grains commonly larger than 100µm. Rutile is euhedral to anhedral with sizes that range from 20 - 100µm. Acicular rutile occurs throughout the sample and occur along the cleavage of white mica grains.

Sample R1 is a biotite-garnet schist with biotite, white mica species, garnet, amphibole, rutile and zircon. Add: Briefly describe the textuers and any Cross cutting relations because these bear on pro/retrograde assemblages. Garnet porphyroblast reach up to a centimeter in size. White mica and biotite are throughout the sample defining the dominant foliation, with biotite in contact at garnet grain boundaries. Rutile grains are typically oriented within the dominant metamorphic fabric as defined by phyllosilicates (Figure 3.2g-m).

T1 is quartzofeldspathic gneiss with minor tourmaline. T2 was sampled from an eclogite boudin and consists of amphibole, rutile, biotite and titanite as major phases (Figure 3.2N. showing replacement textures). Titanite rimming rutile is apparent throughout the sample.

T3, also sampled from an eclogite boudin, consists of rutile, amphibole, biotite, garnet, and titanite and pyroxene. In T3 the amphibole shows signs of exsolution and titanite rimming rutile is observed (Figure 3.2O).

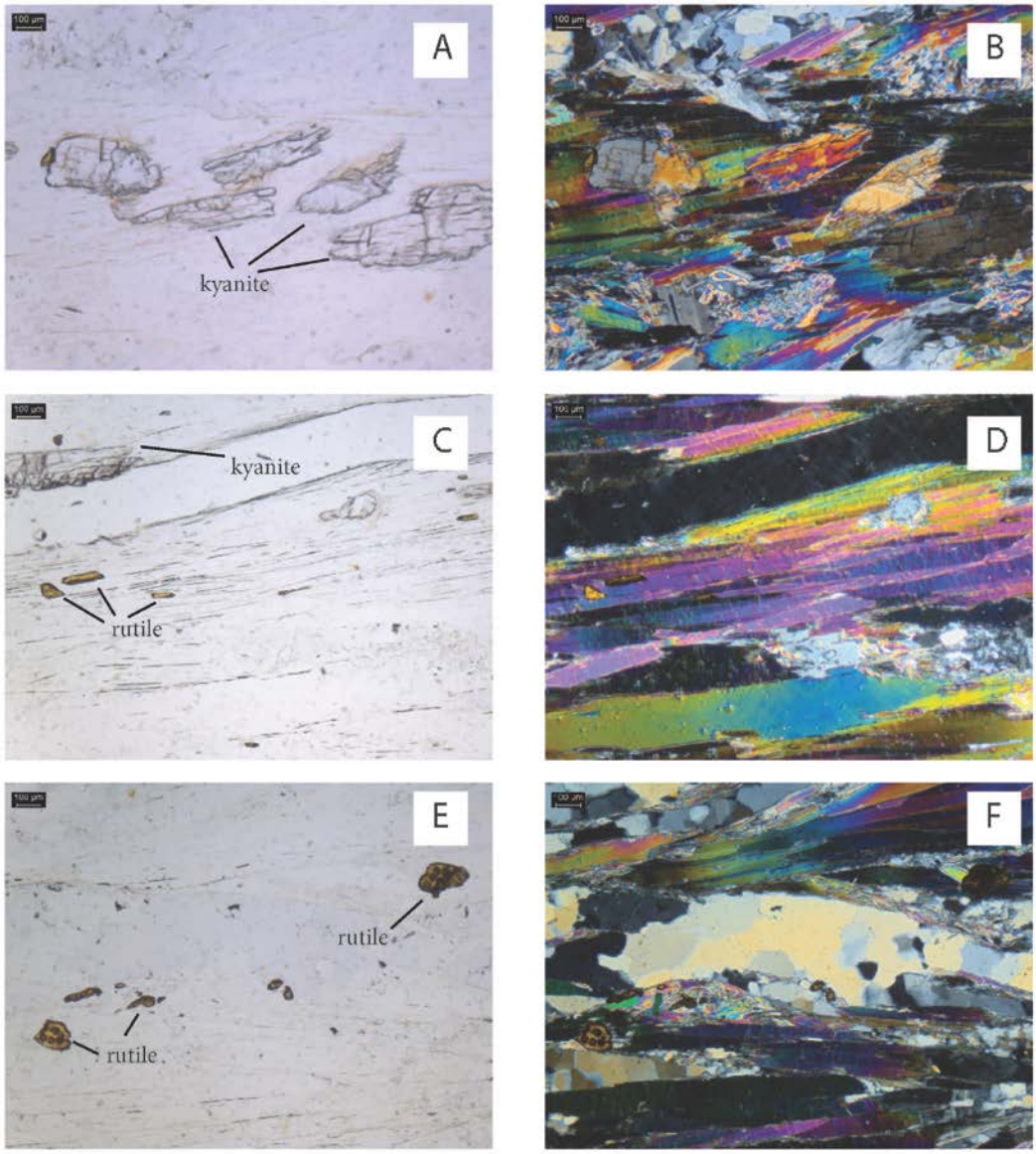

Figure 3.2 Plane polar and Cross Polar images of sample R2 A-B) Image of Kyanite grains surrounded by white mica and quartz. C-D) Prismatic rutile and bladed kyanite. E-F) Mixture of equant and prismatic rutile. G-H) Spot analyses of R2 in plane and cross-polarized light. I-H) Spot analyses of R2 in plane and cross-polarized light. K-L) Biotite rimming garnet shown in plane and cross-polarized light. M) R1 sample showing amphibole grain included in garnet, and biotite after garnet. N) Sample T2 with biotite and muscovite grains. Titanite rims equant rutile grains. O) Sample T3 showing blue-green amphibole present with biotite and titanite rimming rutile. P) Sample T3 showing similar relationships as (O). Q) Sample T5 showing analyses spots of titanite, and tourmaline grain. R) Analyses spots of sample T5.

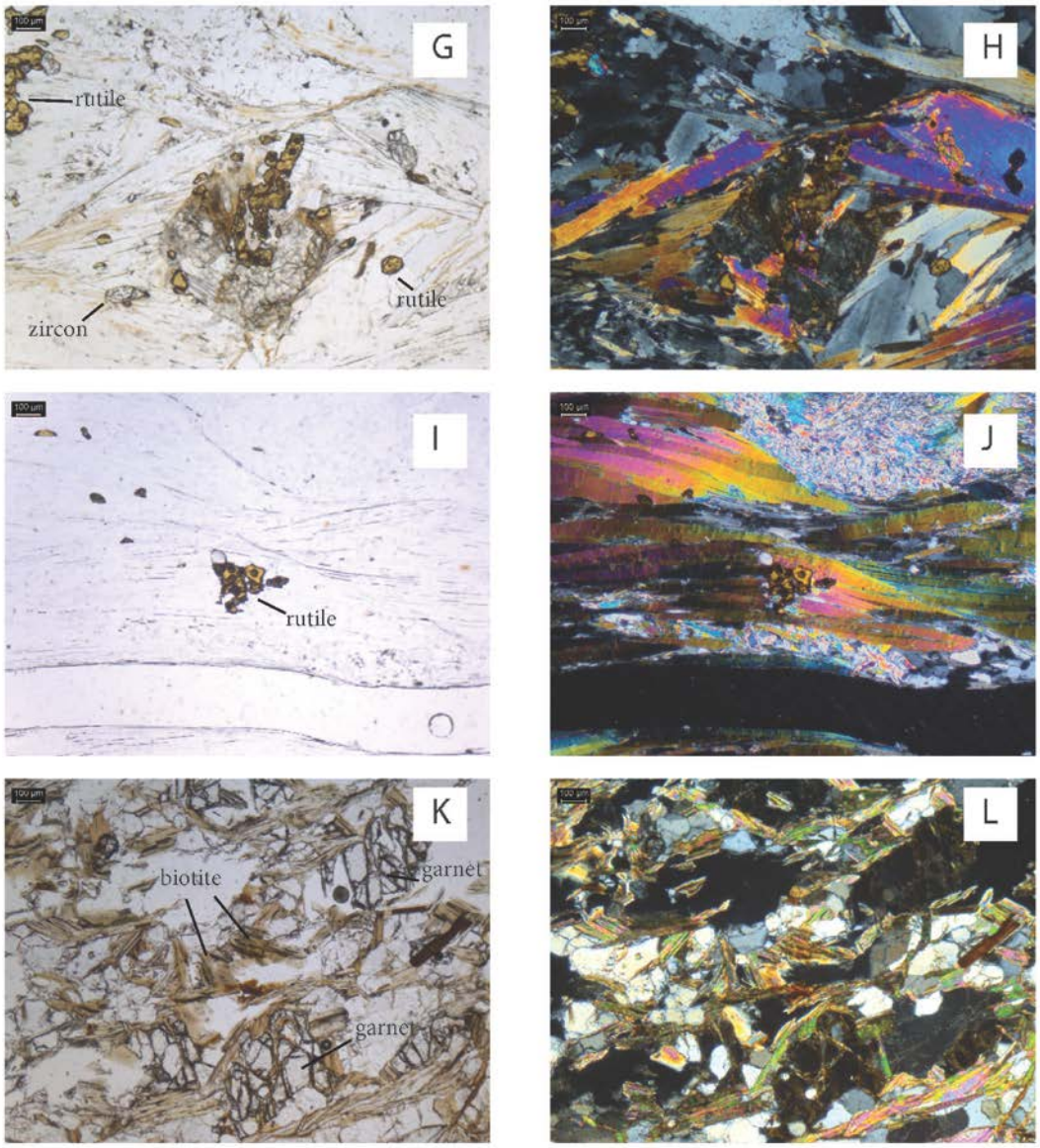

Figure 3.2 continued

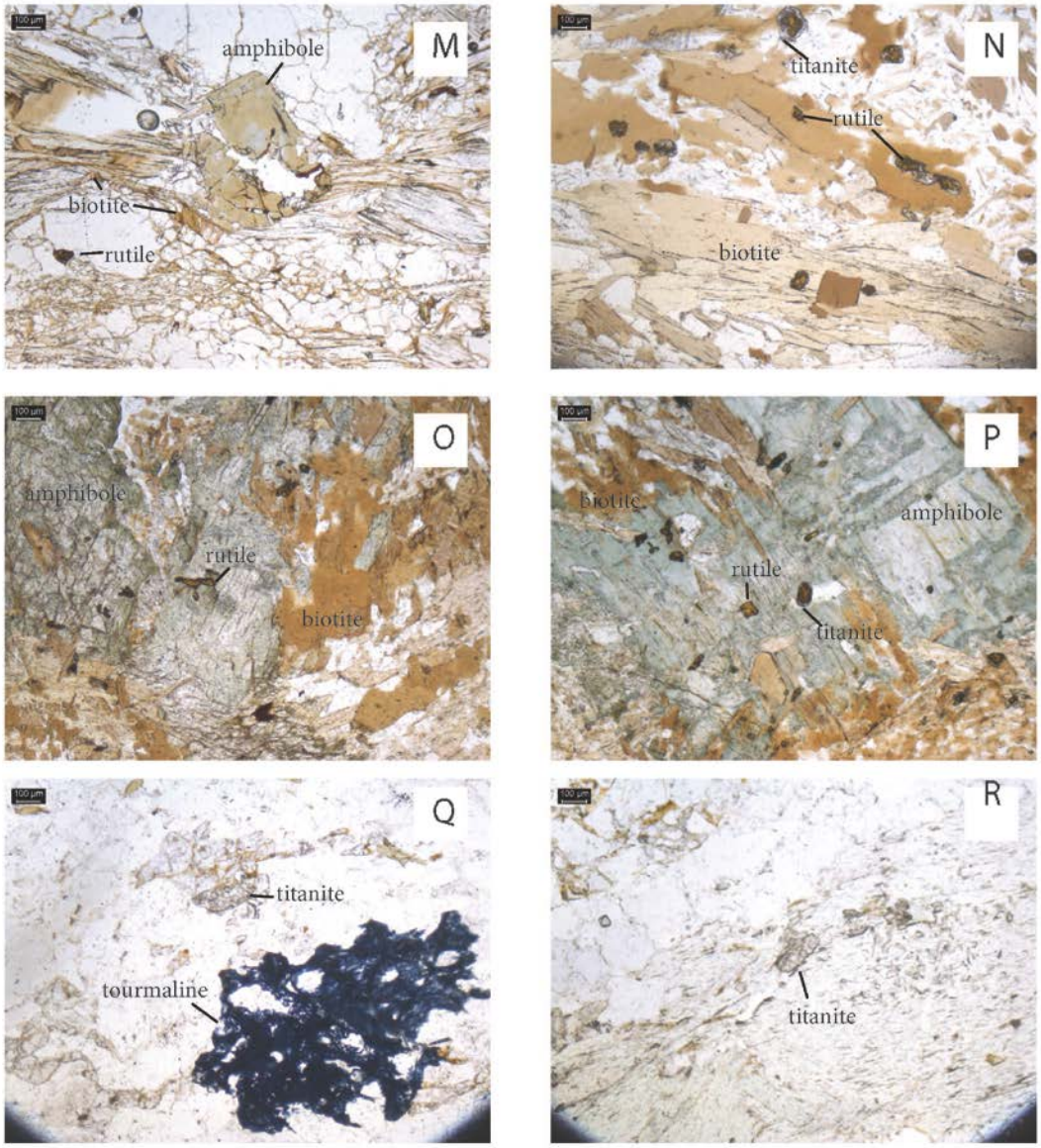

Figure 3.2 continued

T4, sampled from an eclogite boudin, consists of rutile, titanite, amphibole, garnet, pyroxene and biotite. Amphibole in sample T4 shows signs of exsolution similar to sample T3 and titanite rimming rutile is observed.

T5 is a quartzofeldspathic gneiss consisting of quartz, plagioclase, muscovite, titanite, apatite, minor zircon and tourmaline. The tourmaline is patchy with a dark blue color in plane polarized light (Figure 3.2Q).

T6 is a quartzofeldspathic gneiss consisting of qtz, fsp, muscovite, titanite, apatite, and minor zircon (Figure 3.2R). These samples are the basis for age determinations.

3.3 Methods

3.3.1 Geochronology

U-Pb analyses of rutile and titanite in the suite of samples took place at the University of California, Santa Barbara LASS Laboratory using a Nu Plasma HR MC-ICP-MS following the procedures of Kylander-Clark et al. (2013). Samples were ablated via an Analyte 193 eximer ArF laser-ablation system equipped with a HeLex sample cell. Laser energy was set to 4 mJ, which, once transmitted into the sample chamber, equates to ~0.1 µm/pulse; repetition rate was 4 Hz; single-ablation duration was 20–25 seconds; and spot diameters were 30 µm. Depending on size, some grains were shot multiple times- up to 6 spots per grain. U–Pb measurements were obtained with the Nu Plasma, equipped with four low-mass side electron multipliers for simultaneous measurement of ^{208}Pb, ^{207}Pb, ^{206}Pb and ^{204}Pb; ^{238}U and ^{232}Th were measured on Faraday cups equipped with 1011-ohm resistors. Internal standardization was unnecessary because the standard analyses were matrix-matched. Sample analyses were preceded by a 10-second baseline measurement, and unknown analyses were corrected with the R10 rutile standard and BLR titanite standard. Post-data processing was performed using Iolite (Paton et al., 2010), and Concordia plots were produced with Isoplot (Ludwig, 2003).

3.4 Results

3.4.1 Geochronology

In situ analyses of rutile were performed on thin sections from samples R1 and R2, while titanite *in situ* analyses were obtained on samples T1, T2, T3, T4, T5, and T6. Size of analyzed grains typically were >100µm. All samples were collected in the central part in the Tso Morari UHP terrane (Figure 3.1C). U-Pb isotopic results for all samples are presented in Tera-Wasserburg Concordia plots (Figure 3.3), probability density functions (PDF) of ^{207}Pb corrected dates (Ludwig, 2009) (Figure 3.4), and in supplementary tables (Appendix Table 2).

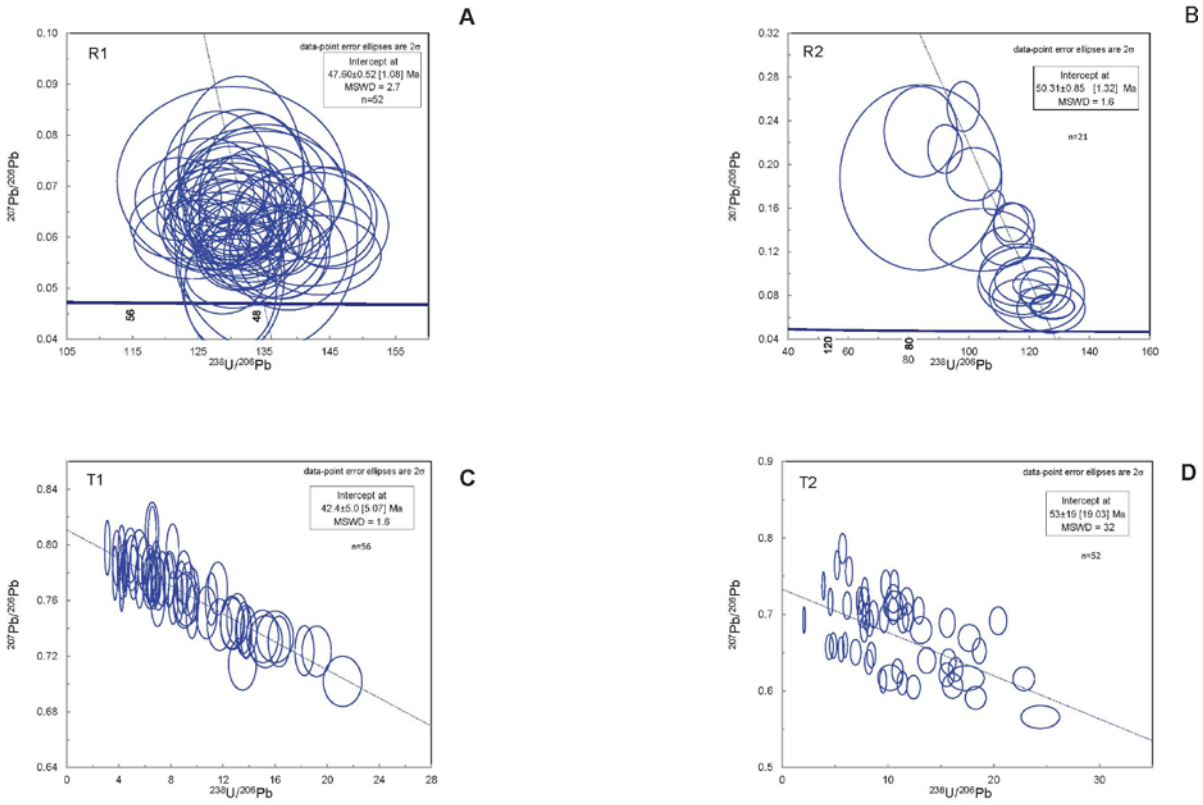

Figure 3.3 Rutile and titanite isochron dates. Tera-Wasserburg Concordia plots of U-Pb data uncorrected for common-Pb. Lower intercept dates of best fit lines through all data are noted in upper right of each plot. MSWD-mean square weighted deviates.

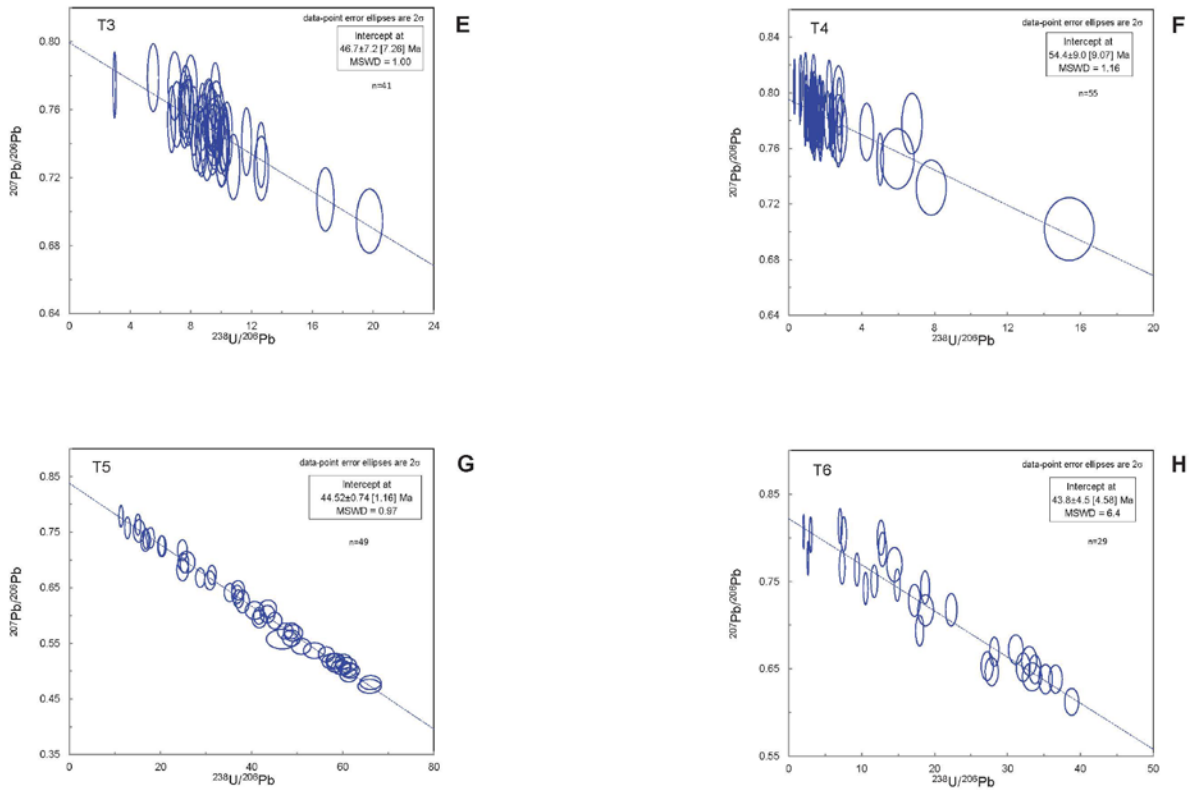

Figure 3.3 continued

All uncertainties are given at the 95% confidence or 2σ level. Rutile in eclogitic samples analyzed yielded very low U ppm counts. Due to this feature, rutile in retrogressed eclogite was not analyzed in eclogite samples T2, T3, and T4.

Rutile U/Pb intercept ages are 47.60 ± 0.52 Ma [mean square of weighted deviates (MSWD) = 2.7] for sample R1 and 50.31 ± 0.85 (MSWD = 1.6) for sample R2 (Figure 3.3). Samples T1, T2, and T3 yielded respective rutile U/Pb intercept ages of 42.4 ± 5.0 Ma (MSWD = 1.6), 53 ± 19 Ma (MSWD = 32), and 46.7 ± 7.2 Ma (MSWD = 1).

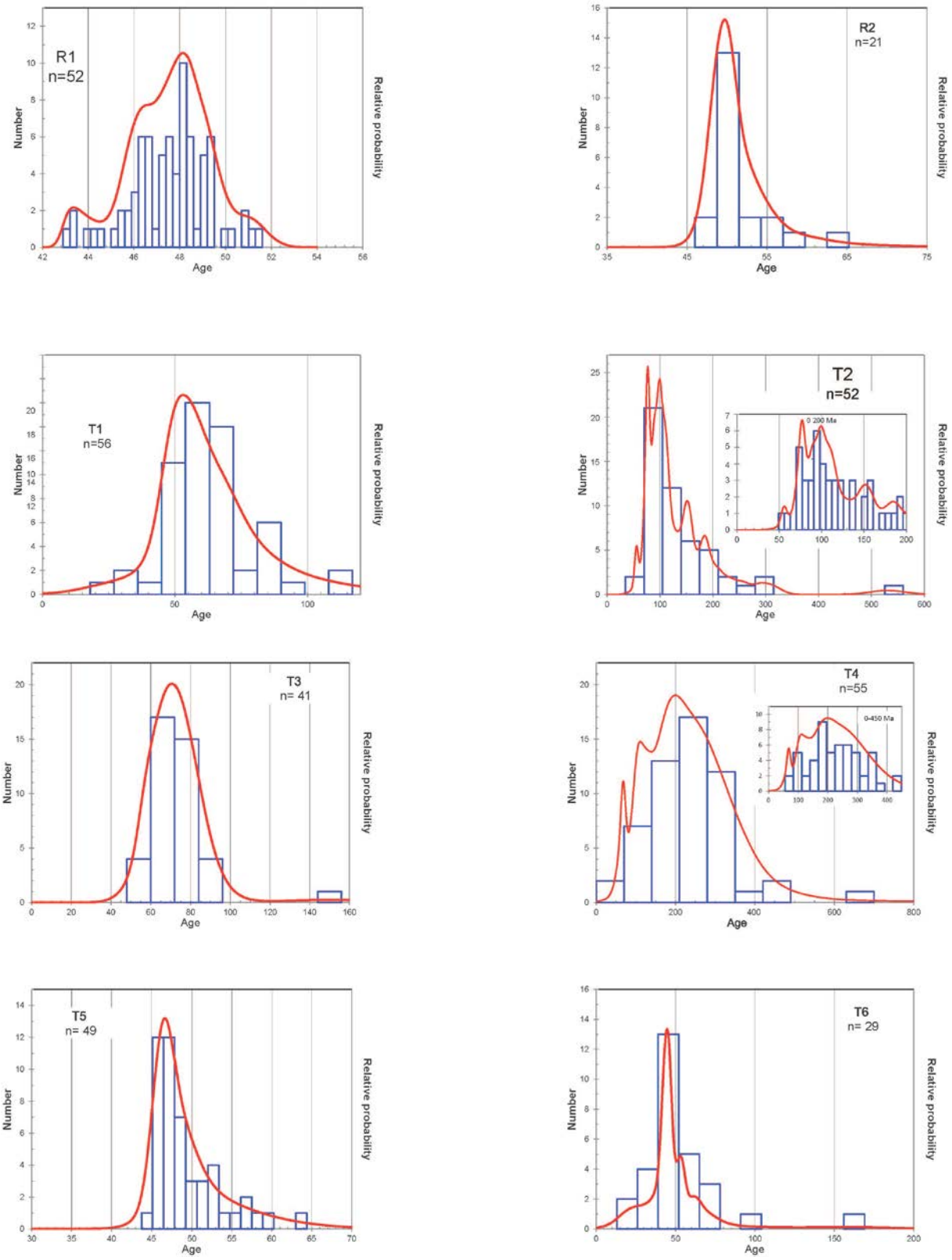

Figure 3.4 Probability Density Functions of rutile and titantie samples X-Axis is 207/Pb-corrected ages of individual analyses. Y-Axis is the number of analyses.

Samples T4, T5 and T6 yielded respective titanite U/Pb intercept ages of 54.4 ± 9.0 Ma (MSWD = 1.16), 44.52 ± 0.74 Ma (MSWD = 0.97), and 43.8 ± 4.5 Ma (MSWD = 6.4). The arrays of analyses in all samples were anchored to Stacey-Kramers (1975) model value of 0.838. MSWD values for all samples can be found in Figure 3.3, however the analyses on samples T3, T5 and T4 show values proximal to 1. Generally MSWD values approaching 1 represent single growth populations or a good statistical fit to the analytical uncertainty, while large values indicate multiple populations or an observed scatter that exceeds what is predicted by the analytical uncertainty (e.g., Wendt and Carl, 1991, Schoene et al., 2013).

3.5 Discussion

3.5.1 Geochronology

From the eight analyses of rutile, three reliable ages were available from samples R1, R2 and T5. U-Pb rutile dating of the R1 and R2 rocks reveal early Eocene crystallization ages of 47.6 and 50.3. Both ages have errors under ± 1 Ma with MSWD values above 1, such that they do not lie within error of one another.

The T5 titanite U-Pb date reveals a narrow age range compared to the other titanite analyses with an MSWD of approximately 1 and an age error less than ± 1 Ma. Other titanite samples will be discussed briefly below.

3.5.2 Titanite Geochronology

Quartzofeldpathic gneiss samples T1, T5 and T6 gave no clear indication of metamorphism above amphibolite grade based on petrographic observations. Higher- grade minerals such as garnet and pyroxene have not been identified and rutile is not present. The age population of T1 shows a fairly consistent trend when observing the 42.4 ± 5.0 Ma intercept age (Figure 3.3.). Samples T5 and T6 show similar characteristics as T1 in that the bulk of ages are

Cenozoic. T5 has an MSWD of .97 suggesting it is a single population and its intercept age is within error of previously interpreted amphibolite metamorphism at ~44 Ma (de Sigoyer et al., 2000, St-Onge et al., 2013, Wilke et al., 2015).

As the eclogite and gneiss likely experienced the same P-T path due to their proximal spatial relationship, the titanite likely grew during retrograde heating. Assuming that the gneiss and eclogite followed similar P-T paths, we suggest that titanite here experience temperatures above the closure temperature for titanite and were effectively reset, making the ~44 Ma age for T5 a cooling age.

Several samples display large uncertainties and therefore do not provide additional age constrains. These large errors apparent in many of the titanite samples are likely a result of common Pb, Strong age interpretations from T6 cannot be made due to its large uncertainty and high MSWD (Figure 3.4). Likely the titanites represent multiple metamorphic age populations and/or growth events. Because of the large uncertainty of ±19 Ma and MSWD of 32 in sample T2, no additional age constraints are provided. Sample T3 has a MSWD value of 1, which implies the analyses represent a single population (Wendt and Carl, 1991). Given its large error of ± 7.2 however, no reliable age interpretations of T3 can be made. Sample T4 with an age of ~54.4 ± 9 Ma and MSWD of 1.19 is subject to an age uncertainty that is also too large to make contributive interpretations. In summary, titanite in Tso Morari grew through multiple metamorphic events, some of which predate all the debated ages assigned to UHP metamorphism. The youngest age is consistent with the upper crustal heating event at 46-42 Ma that followed UHP metamorphism.

3.5.3 Rutile Analyses

Sample R1 age of 47.60 ± 0.52 Ma and MSWD of 2.7 indicates that multiple populations of rutile grew within a narrow time frame or that there was protracted growth of rutile during a metamorphisc event (Figure 3.3.) the PDF for R1 shows the range of ages span from ~43-51 Ma, with the bulk of ages occurring between 49-46 Ma. This data suggests that the bulk of rutile growth occurred during this time and likely is coincident with high-pressure metamorphism. This age is similar to the UHP age suggested by eclogitic zircon (Donaldson et al., 2013). Therefore this age range is interpreted to represent a short period of protracted prograde growth to UHP metamorphism.

Sample R2 age of 50.31 ± 0.85 Ma, MSWD of 1.6 and PDF indicates multiple populations or a short period of protracted rutile growth in the sample (Figs. 3.3, 3.4). The R2 PDF has a strong peak around 50 Ma. The total age range is 46-65 Ma. The age of R2 compared to zircon ages from Donaldson et al., (2013) suggests that rutile grew during prograde metamorphism. The strongest interpretations that can be made about R1 and R2 are that they both experienced protracted rutile growth with peaks around 48 and 50 Ma—supported by the peaks in the probability density functions for both rutile samples (Figure 3.4).

When compared to the Donaldson et al., (2013) interpreted UHP age of 46 Ma, the rutile presented in this study suggests prograde-UHP growth at 50 Ma and 47 Ma. The results of this study may guide the data collection in future studies and improve the prograde P-T-t path at Tso Morari.

3.6 Conclusions

Analyses of rutile and titanite from Tso Morari provide additional context about the age of metamorphic events in Tso Morari Gneiss dome terrane. Briefly state what this is…protracted

growth, retrograde phase. However these data lack the thermobarmetric constraints that place the rutile and titanite in the petrologic context and in specific metamorphic P-T space. With intensive thermobarometry and petrology, the possibility of better constraining UHP metamorphism at Tso Morari may arise.

CHAPTER 4
INVESTIGATION OF HIMALAYA DEVELOPMENT: SHORTENING AND GHC EMPLACEMENT

4.1 Introduction

Our understanding of the total shortening budget in the Himalaya is not well understood, and it has been argued that the geological shortening budget grossly underestimates the shortening recorded by plate circuit reconstructions (Klootwijk et al., 1992; Decelles et al., 2002,). A new model for Himalayan tectonic assembly, the Greater Indian Basin tectonic (GIB) model predicts the roughly 2,350 km of missing crustal shortening can be explained by the extension of a "Greater Indian Basin". In this model, the Tethyan Himalayan Sequence (± the Greater Himalayan Crystalline complex) which now dominates the northern Himalaya rifted from the northern margin of India in the Mesozoic, opening an ocean basin, then collided with Asia at ~52 Ma (Van Hinsbergen et al., 2012, Donaldson et al., 2013). Final closure of India with Asia is speculated to occur at ~25 Ma. Although no such suture has yet been identified, it is postulated that it lies immediately atop, within, or immediately below the Greater Himalayan Crystalline complex (Van Hinsbergen et al., 2012; DeCelles et al., 2014). The proposed closure of the "Greater India Basin" between the northern "Himalayan" terrane and the rest of the Indian continent would account for the missing shortening because closure of an oceanic basin via subduction leaves only fragmentary, incomplete shortening records.

Another possible explanation for the difference between the paleomagnetically-constrained plate circuit shortening and the geological shortening is that the balanced (geological) shortening estimates may be incomplete due to erosion of, and/or failure to recognize key shortening records (Webb, 2013). For example, in the northwest Himalaya between the Indus suture zone and the Himalayan front there is a continuous sequence of low

grade metamorphic and sedimentary rocks (Figure 4.1), but the southern extent of this sequence remains unassessed in shortening budgets, in large part because the affinity of these rocks has been in dispute (see below, and Webb et al., 2011). We look to test this proposed extra shortening of the GIB model by determining the amount of shortening in this southern unassessed region.

The overall tectonic geometry of the Himalaya allows us to consider an infrastructure – superstructure concept for the development of the range. This concept follows the model presented by Culshaw et al., (2006). The 'infrastructure' represents the high grade lower component of the orogen. The 'superstructure' represents the lower grade rocks that cover the 'infrastructure'. The infrastructure in the Himalaya consists of the medium to high grade Greater Himalayan Crystalline (GHC) complex which lies tectonostratigrahically beneath the low grade Tethyan Himalayan Sequence (THS) superstructure. The South Tibet detachment marks the zone of decoupling separating the two domains (e.g., Kellett and Grujic, 2012).How the Himalaya kinematically came to form its structural relationship between the superstructure and the infrastructure is still questioned.

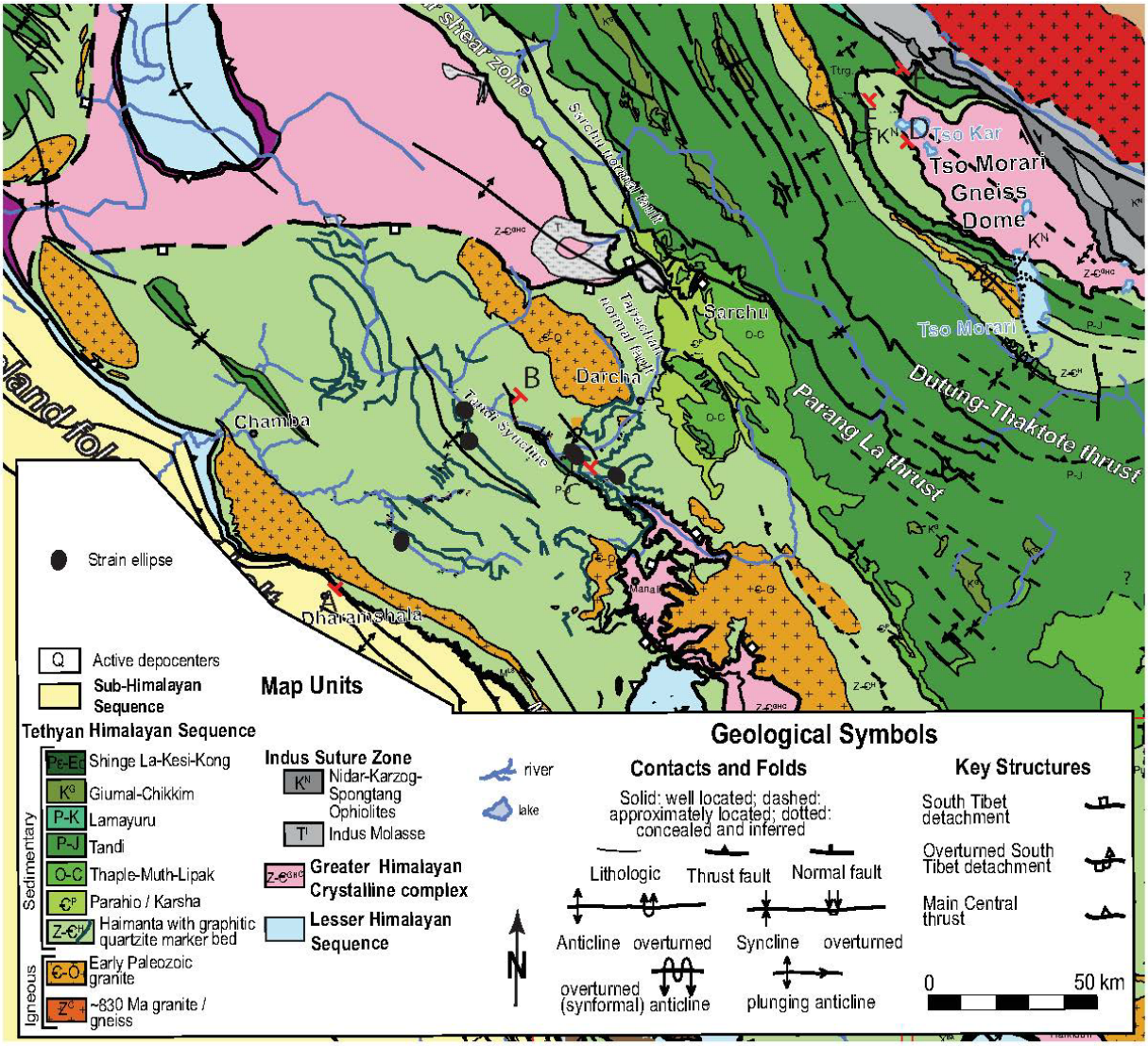

Figure 4.1 Geologic map of Lahaul-Chamba and Tso Morari Region

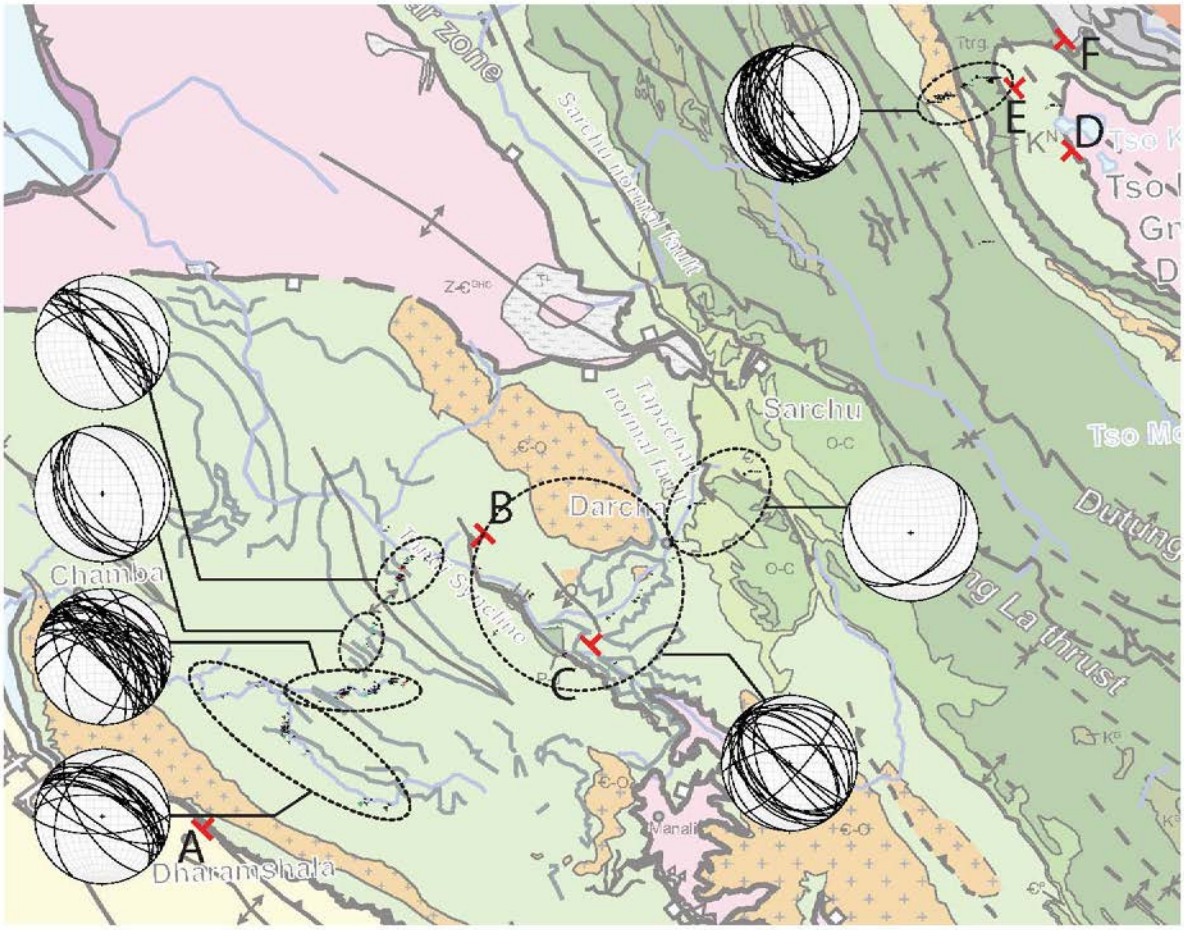

Figure 4.1 continued

Three tectonic models, Wedge Extrusion; Channel Flow; and Tectonic Wedging all propose different processes as responsible for the emplacement of the infrastructure (Figure 4.2): 1) Wedge extrusion models show these rocks extruded southwards between the superstructure and the Indian craton (now represented by the subsequently accreted Lesser Himalayan Sequence) as a northward-tapering wedge (Burchfiel and Royden, 1985). The South Tibet detachment is a normal fault during this extrusion. Many recent workers associate these kinematics with critical taper – Coulomb wedge theory (e.g., Robinson et al., 2006; Kohn, 2008; Zhang et al., 2011), which suggests that normal faulting may occur during collapse of over-thickened thrust wedges (e.g., Davis et al., 1983; Dahlen, 1990). 2) In channel flow focused

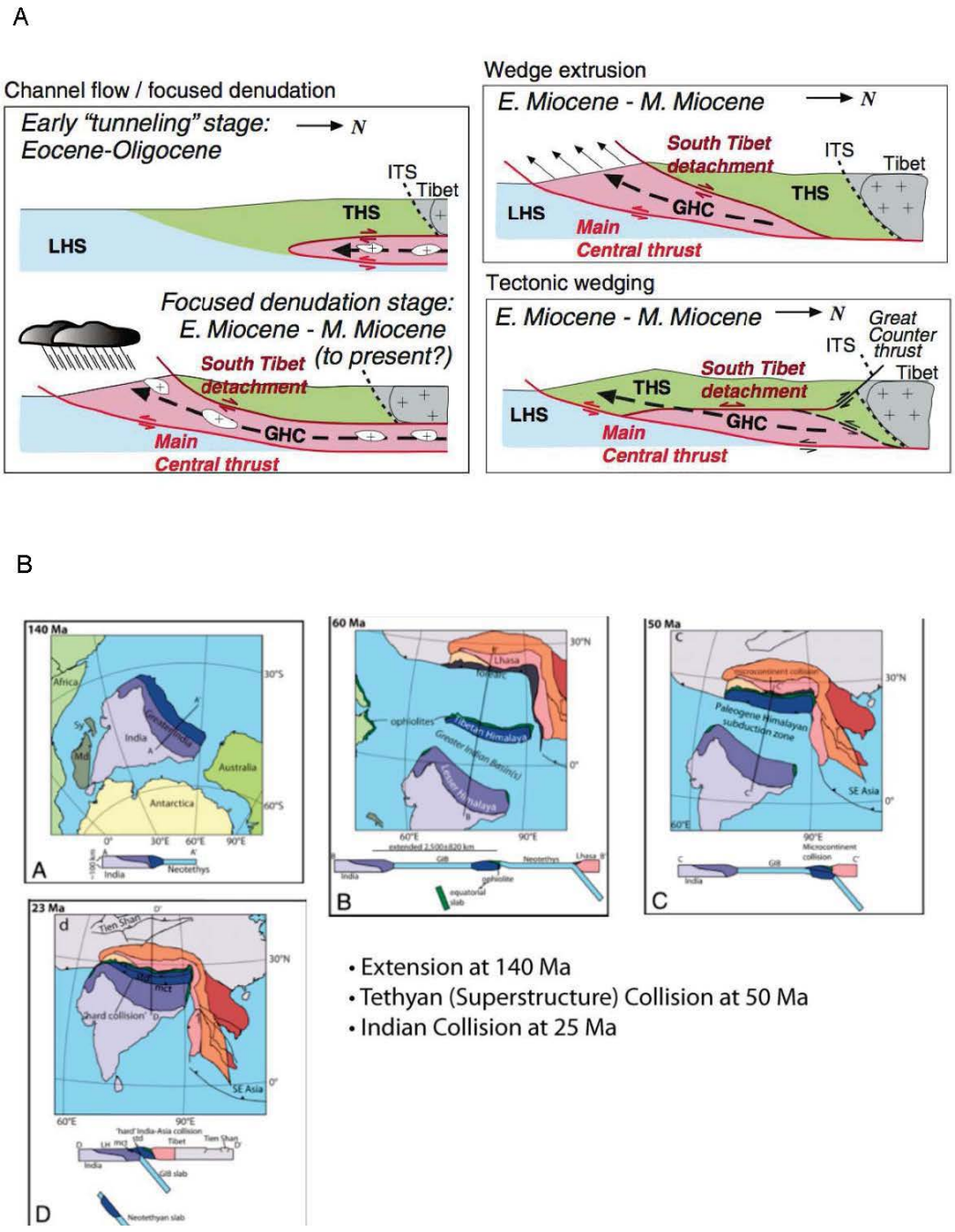

Fig. 4.2 A) Tectonic Models for superstructure emplacement and Indian-Asia Collision. B) Greater Indian Basin Model.

denudation models, the high grade rocks tunnel southwards during the Eocene- Oligocene, a process driven by the lateral pressure gradient created by the gravitational potential difference between the Tibetan plateau and its margins (e.g., Beaumont et al., 2001; 2004; Godin et al.,

2006; Long and McQuarrie., 2010). During this stage the South Tibet detachment is sub-horizontal and operates as a crustal-scale backthrust (see Figure 3A of Beaumont et al., 2001). Subsequently this material is exhumed by enhanced erosion across a narrow zone where precipitation is focused along the topographic front of the orogen (e.g., Beaumont et al., 2001; Hodges et al., 2001; Clift et al., 2008). During this second, extrusive phase, the South Tibet detachment is a normal fault. 3) Tectonic wedging models show southwards emplacement of the Greater Himalayan Crystalline rocks entirely below the Earth surface (Yin, 2006; Webb et al., 2007; 2011a). The South Tibet detachment is a backthrust, and current exposure of high-grade rocks results from post-early/middle Miocene erosion and footwall deformation. Therefore unlike other models, this model lacks an extrusive phase. Model kinematics may be comparable to the early tunneling phase of channel flow, albeit with different timing (early to middle Miocene vs. Eocene-Oligocene motion).

Extrusion models predict that the Greater Himalayan 'infrastructure' is emplaced at the surface in the early or middle Miocene. This prediction may fail or be strongly limited across the study region of eastern Ladakh – Chamba because of the strip of continuous THS 'superstructure' rocks recognized here from the suture zone region to the foreland (Figure 4.1, 4.2) (e.g., Fuchs and Linner, 1995). This strip appears to currently cover the high grade rocks across the Chamba region and may have covered all high grade rocks across the entire region until ~11 to 5 million years ago (Webb, 2013). Alternatively, some workers consider the southern half of this 'superstructure' strip to be Greater Himalayan Crystalline complex (e.g., Searle et al., 2007). All workers nonetheless agree that the much of the southern and northern portions of the strip is dominated by anchizone to greenschist facies meta- sedimentary rocks (e.g., Frank et al., 1973; 1995; Spring et al., 1993; Girard et al., 2001). Alternate extrusion

models have been put forward here showing that normal faulting at the top of the extruding zone may displace superstructure in the footwall (e.g., Epard and Steck, 2004).

This study looks to examine the stratigraphic continuity of the THS by analyzing a transect from the suture zone through the foreland. In this transect the infrastructure is predicted to be exposed according to the Wedge Extrusion and Channel Flow models. The Tectonic Wedging model predicts a THS continuity. To test extrusion models and the GIB model structural mapping was conducted along three transects that represent the apparent continuously exposed THS from the Indus suture Zone through the Lahul-Chamba Regions to the South. Reconstruction of THS throughout these transects should at least increase the upper crustal shortening budget since present reconstructions only account for the northern end of the THS. This exercise can also test the accuracy of the proposed amount of extension developed in GIB model by comparing the reassessed shortening budget to the proposed missing shortening of the Greater Indian extension prior to collision

We will also combine field based balancing techniques with microstructural strain data to reassess shortening estimates for the NW Himalaya. A richer understanding of the meso and microscale as it pertains to overall deformation is essential in accurately assessing the shortening budget (Mitra, 1994; Long et al., 2011a). Processes such as Layer-parallel shortening, record strain on microscopic scales that when accounted for, may increase the shortening estimates of macroscopic structures (Mitra, 1994, Yonkee and Weil, 2009, Long et al., 2011a).

4.2 Geologic Background

4.2.1 Stratigraphic Units

The Himalayan orogen is dominated by four fault-bound units that were accreted from the down-going Indian plate below Asian Plate. From south to north, these units are 1) the Sub-Himalayan Sequence, foreland basin rocks accreted to the growing orogen; 2) the largely low-grade Lesser Himalayan Sequence, main locus of orogenic growth via fold-thrust belt development since the Middle Miocene; 3) the high-grade Greater Himalayan Crystalline complex, bound below and above by the km-scale Main Central thrust and South Tibet detachment (STD) shear zones, respectively; and 4) the largely low-grade Tethyan Himalayan Sequence (THS), deformed in an Eocene-Oligocene fold-thrust belt (Heim and Gansser, 1939; Gansser, 1964; Le Fort, 1975; Hodges, 2000; DeCelles et al., 2001; Yin, 2006). These units and their bounding structures tend to dip shallowly to the north, but are commonly tilted into other orientations (e.g., Valdiya, 1980; Gleeson and Godin, 2006; Jessup et al., 2008). The Indus-Yarlung suture zone separates these rocks from the Asian plate to the north, and is generally marked by the south-dipping, north-directed Great Counter thrust along its southern boundary (Yin et al., 1994; 1999; DeCelles et al., 2011). The Main Central thrust, South Tibet detachment, and Great Counter thrust were active during the Early to Middle Miocene (Burchfiel and Royden, 1985; Burchfiel et al., 1992; Hodges et al., 1992; 1996; Harrison et al., 2000; Searle, 2010; DeCelles et al., 2011).

The THS is a thick tectonostratigraphic section that overlies GHC. The Pre-Cambrian-Cambrian Haimanta group (also known as the Phe formation) is the lowermost section of the THS. Ordovician granite intrusions are at the base of the lower Haimanta. Below, I provide an overview of the THS stratigraphy across NW India:

4.2.2 Lower Haimanta

The lower Haimanta represents upwards to 5 km of monotonous meta-sandstones, meta-siltstones, meta-graywacke and meta-pelites(Frank et al., 1995; Steck, 2003). Sedimentary structures include; flute clasts, graded bedding, crossbedding and other indicators of a turbidite environment.

4.2.3 The Middle Haimantas

The Middle Haimantas begin with the Manjir Conglomerate, a massive thick sequence diamictites interpreted as glaciomarine sediments (Frank et al., 1995). The Manjir consist of boulder slates and other matrix supported clasts (reference picture of large clasts). Observed clasts include quartzites, feldspar grains, large mica books and other detrital grains. Overlying the Manjir Conglomerate is a relatively thin carbonate layer, followed by more meta-graywackes and sandstones (Fuchs and Linner, 1995, Frank et al., 1995, Steck, 2003).

4.2.4 The Upper Haimantas

The late Pre-Cambrian-Early Cambrian Upper Haimantas are similar to the Lower Haimantas, in that it consists of monotonous graywackes, slates, sandstones, carbonates and sericite layers. Additionally there is a graphitic quartzite marker horizon which is highly distinct from the surrounding strata via its yellow and rusty red weathering patterns.

4.2.5 Upper Tethyan Formations

The Parahio Formation additionally known as the Karsha Formation is Middle to Late Cambrian in age. Its thickness is approximately 800m. It consists of fine sandstones, micaceous siltstones, dolomites, stramatolite limestones, and black schists. Occurrence of rare fossils is also prevalent (Nanda & Singh 1977, Steck, 2003). The Thaple-Muth-Lipak succession begins with the Ordovician Thaple Formation. It consists of red, green and white conglomerates and

sandstones. The thickness of the Thaple in some areas approaches 1500 meters (Steck, 2003 and references within). The Devonian Muth Formation has a thickness of ~80 m and consists of quartzite. It is useful as marker horizon within the Thaple-Muth-Lipak succession (Gnasser, 1964; Stoliczka, 1965; Steck, 2003). The Middle Devonian-Early Carboniferous Lipak Formation overlying the Muth Formation consists of carbonates, evaporates, and igneous dikes. The formation is up to 250 m in thickness (Nanda and Singh, 1977; Steck, 2003). The Permian-Jurassic Tandi Group consists of shelf sedimentary rocks such as carbonates, arenites, black shales, quartzites, and shales. In places it reaches thicknesses of approximately 1900 m (Steck, 2003). The Cretaceous Giumal-Chikkim Succession consist of sandstones and limestones approaching 400 m in thickness. It overlies the Spiti shale which is part of the Tandi Group.

4.3 Methods

4.3.1 Field Mapping

Previous mapping illustrations provides the basis for the additional mapping conducted in this study (Fuchs and Linner, 1992, Frank et al., 1995; Vannay & Steck et al., 1995, Steck et al., 1998; and Steck, 2003). The new mapping explores two transects; 1) A-B in the southern Chamba Lahaul region and 2) C-D in the Lahaul to Tso Morari region (Figure 4.1). The A-B transect crosses the Pir Panjal Range through a sections of mapped graphitic quartzite, Manjir Conglomerate and other Haimanta Group rocks. The C-D section covers parts of mapped graphitic quartzite to the south, Upper Haimanta, Parahio, Thaple-Muth-Lipak, and Tandi Group rocks progressively northward. Throughout both A-B and north and south fragments of C-D, structural dip and dip direction measurements were taken on bedding, foliation, and cleavage planes. This approach was taken in the C-D section due to coverage accomplished by previous authors (McElroy et al., 1990; Fuchs and Linner 1992; Vannay and Steck, 1995, Frank et al.,

1995; Corfield and Searle, 2000; Steck, 2003; Epard and Steck, 2008). Additional measurements include fold limbs, fold axes, fault planes, and slicken fibers. Samples and their structural orientations were collected at points of interest throughout the transects. Of the collected samples 14 were adequate for microstructural strain analysis. The inadequacy of the remaining samples results from factors including insufficient grain size and inappropriate mineralogy vs. employed normalized fry and Rf/phi methods (described below) such as rocks dominated by carbonates and micaceous minerals.

Figure 4.3 A) Upper Haimanta Outcrop looking NW. Possible reverse fault shown in red. B) Looking NW Upper Haimanta outcrop with complex deformation characteristic of a fault zone. C) Outcrop of the graphitic quartzite layer looking ESE. Beneath quartzite layer outcrops black slates and carbonates. D) Outcrop of Upper Haimantas looking to the SE. Deformation with possible reverse thrust geometry. E) Folded carbonate section, annotated right image shows folded rock with ~27% shortening. G) Asymmetric fold in the road looking E. H) Isoclinal fold looking ESE. I) folding in outcrop. Total shortening in annotated image is ~32%. J) Deformation in the Upper Haimanta. K) Outcrop of repeating carbonate and micaceous layers. Repetition in rusty colored layers as well. Photo looks to the NNE. L) Isoclinal similar fold on the south valley wall of the Chandra-Bhaga River. M) Graphitic quartzite layer looking SE. N) Boudinage and similar folding in the THS outcrop, book for scale. O) Boudinage in the THS carbonate. Book for scale. P) Multiple folds in the THS outcrop. Similar folding style is dominant.

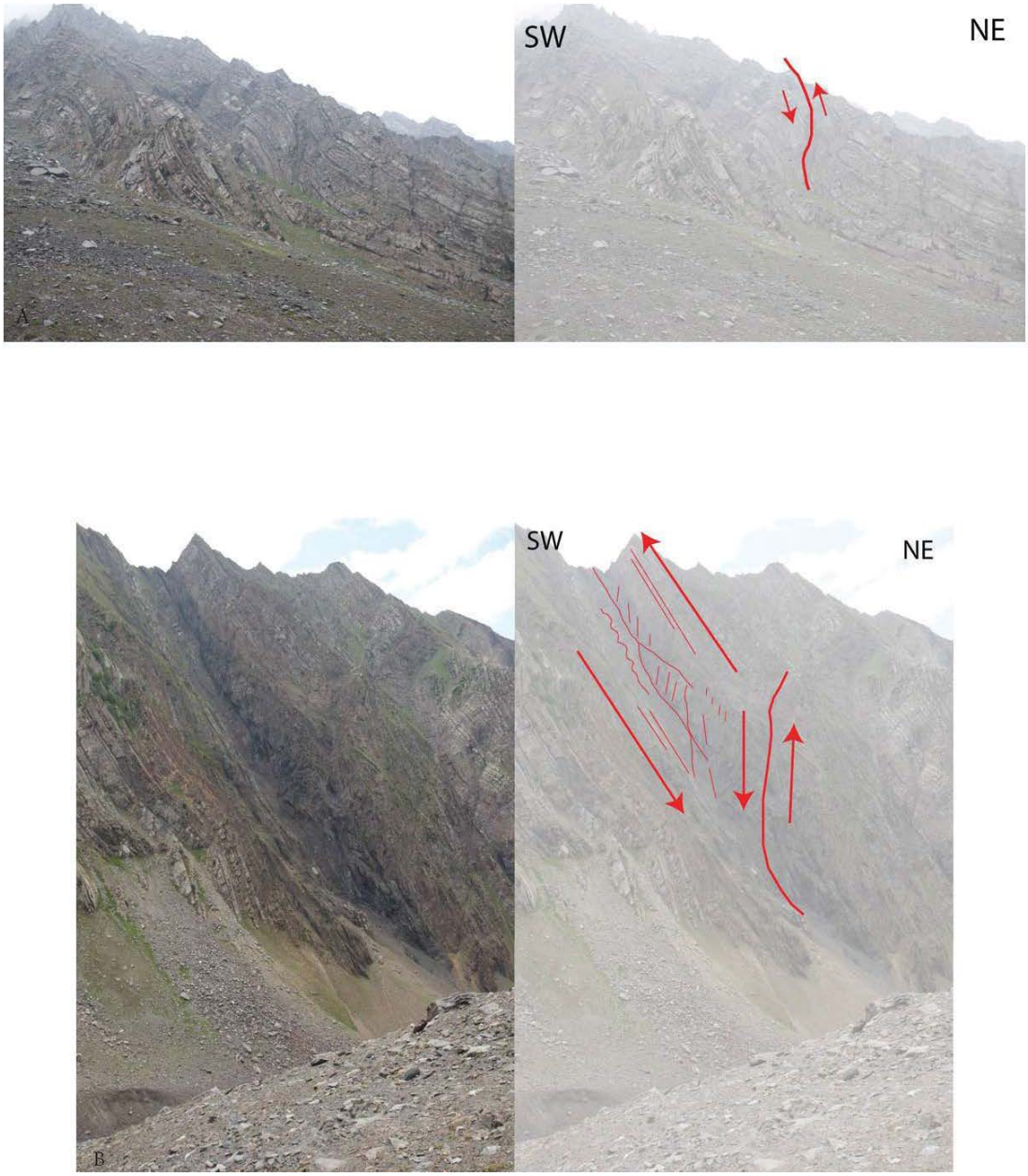

Figure 4.3 continued

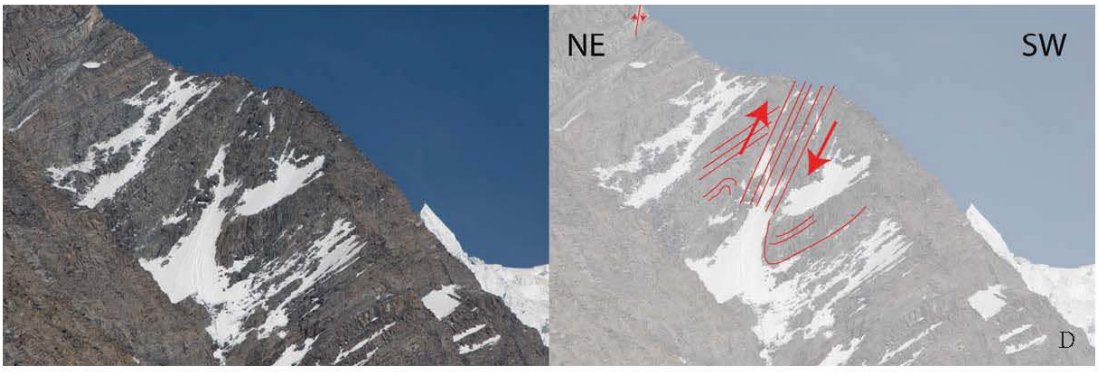

Figure 4.3 continued

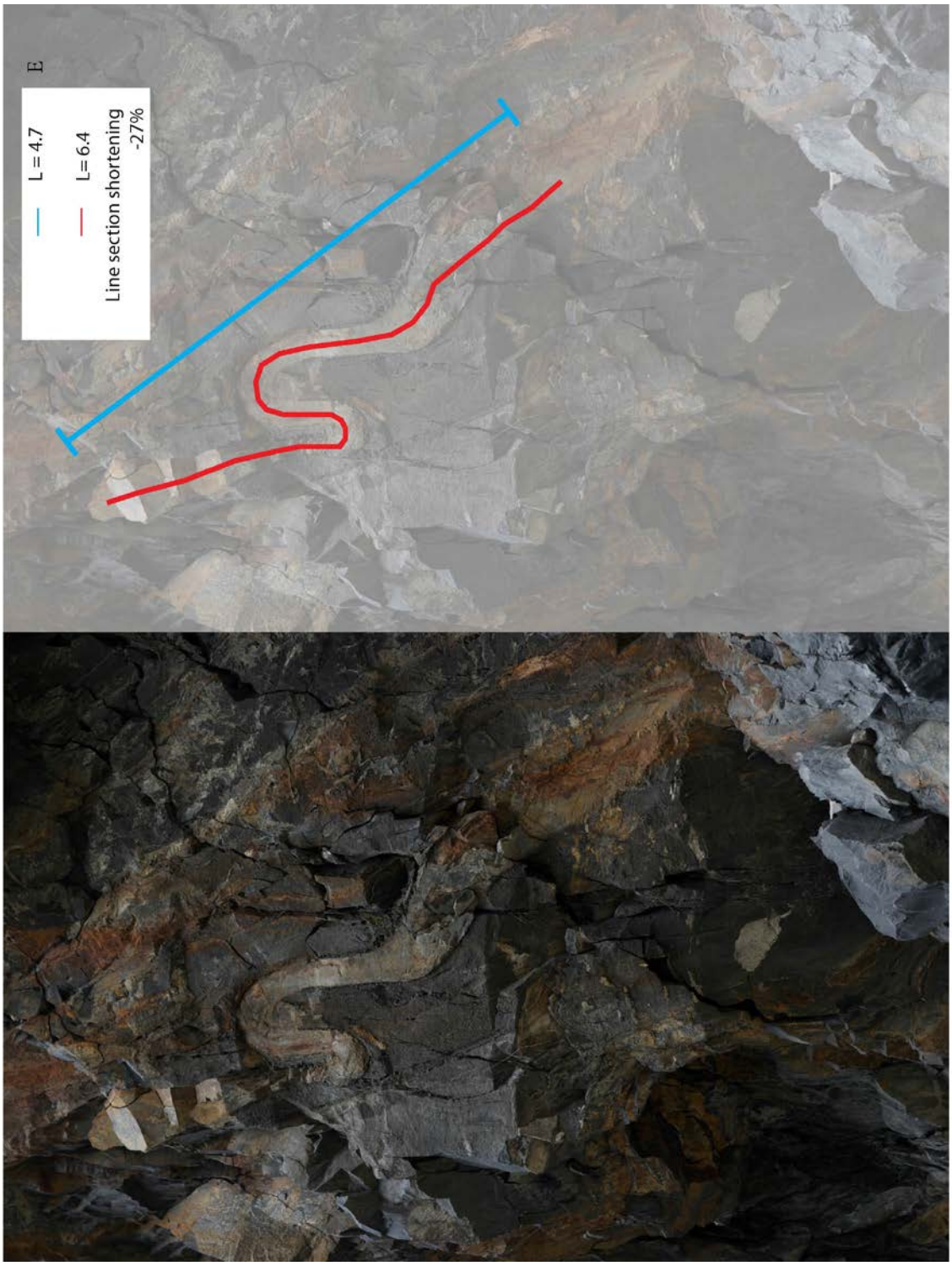

Figure 4.3 continued.

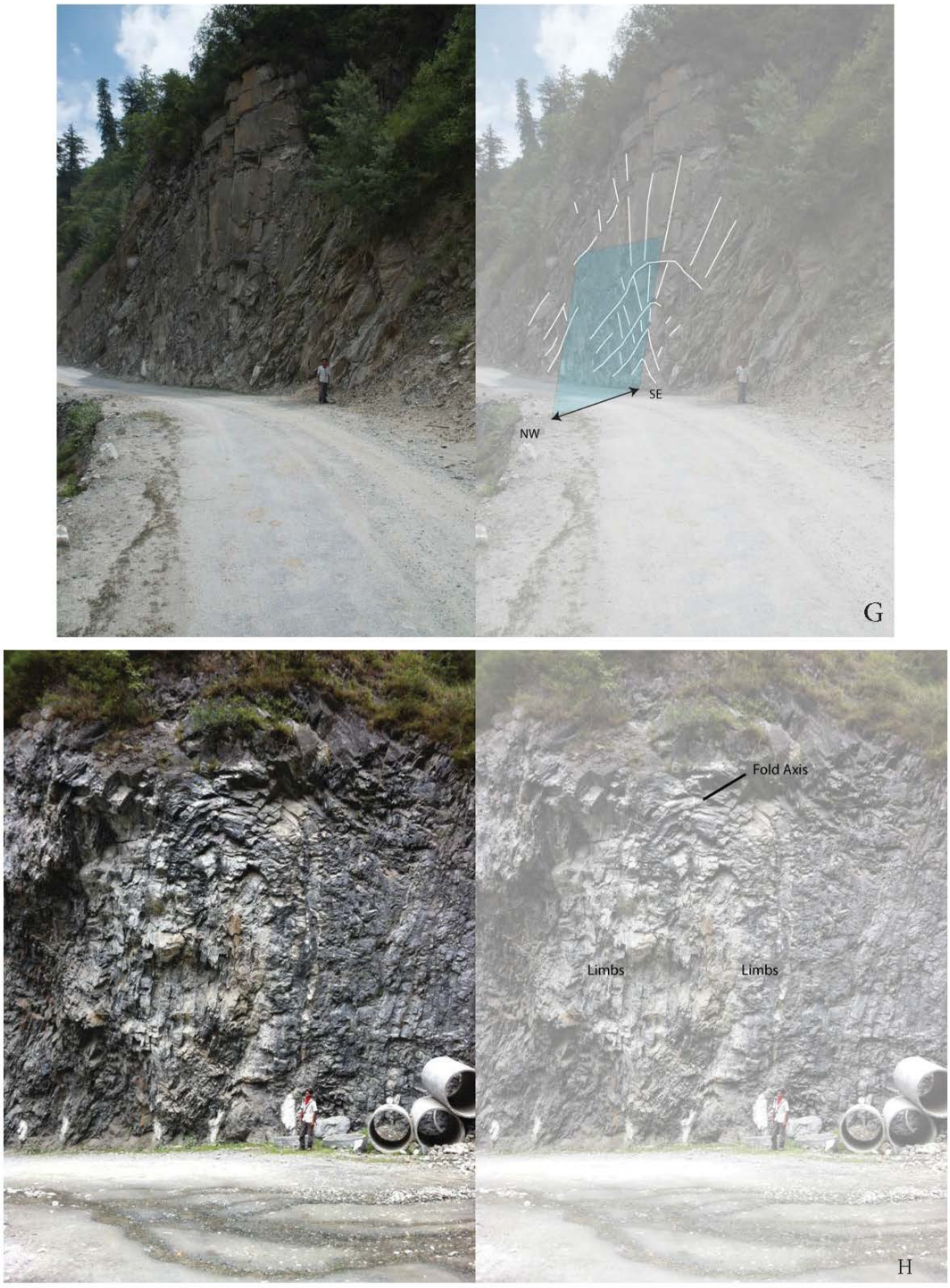

Figure 4.3 continued

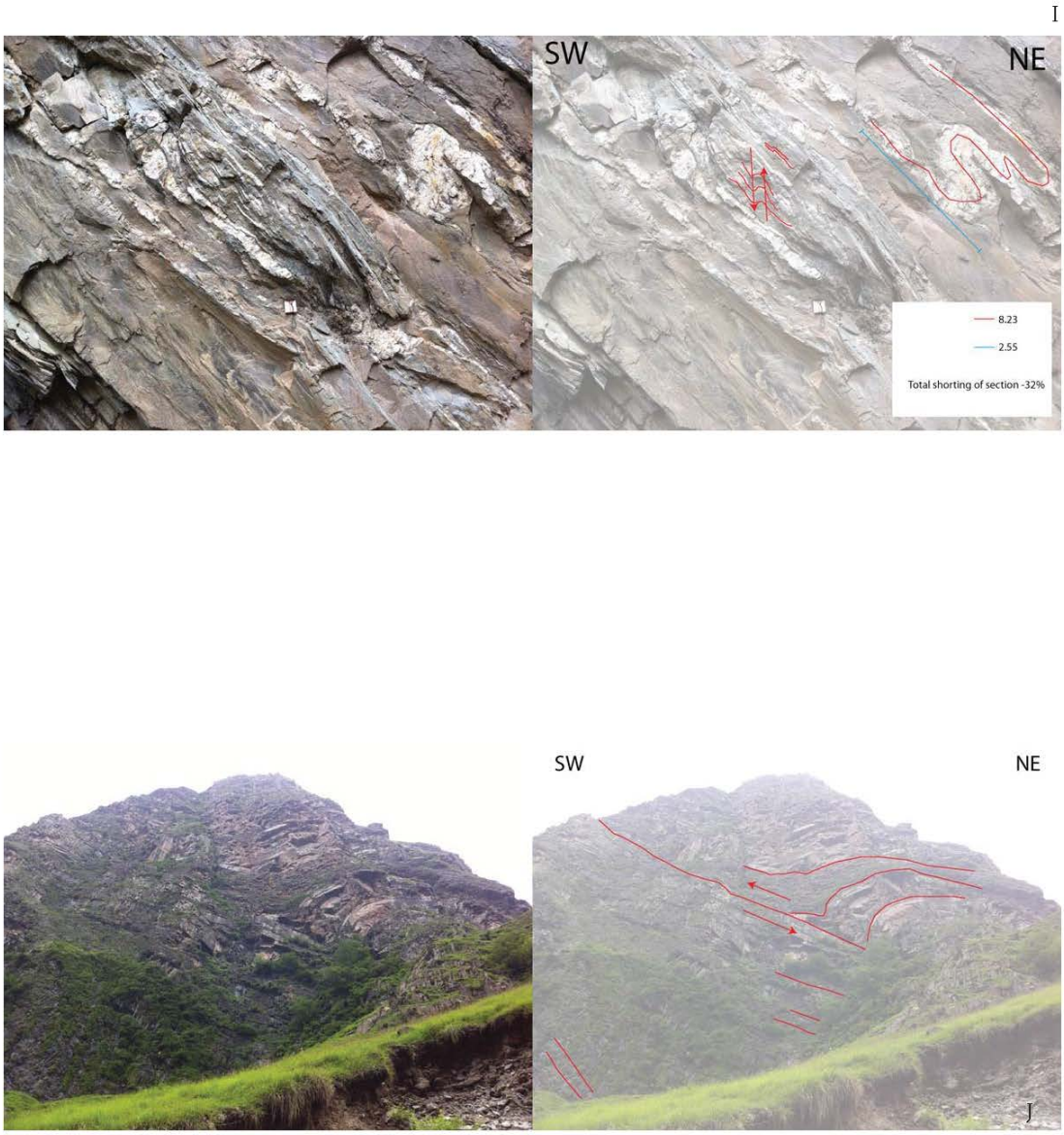

Figure 4.3 continued

Figure 4.3 continued

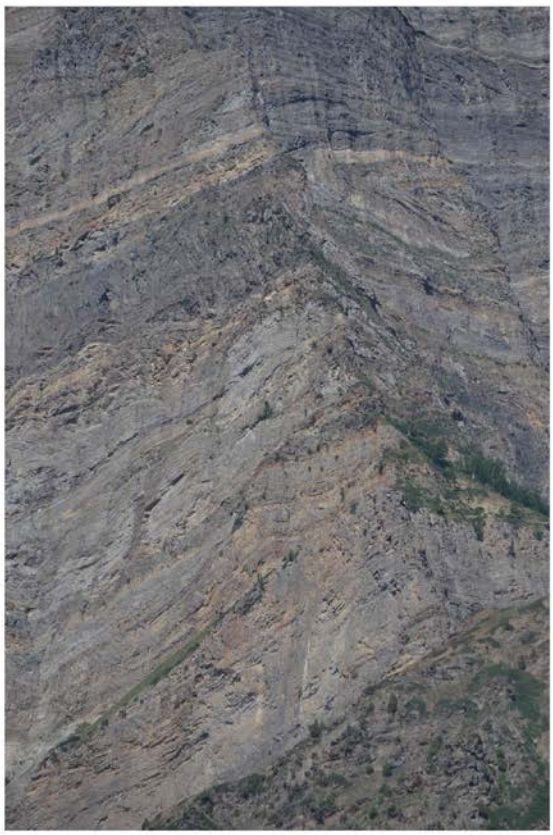

Figure 4.3 continued

Figure 4.3 continued

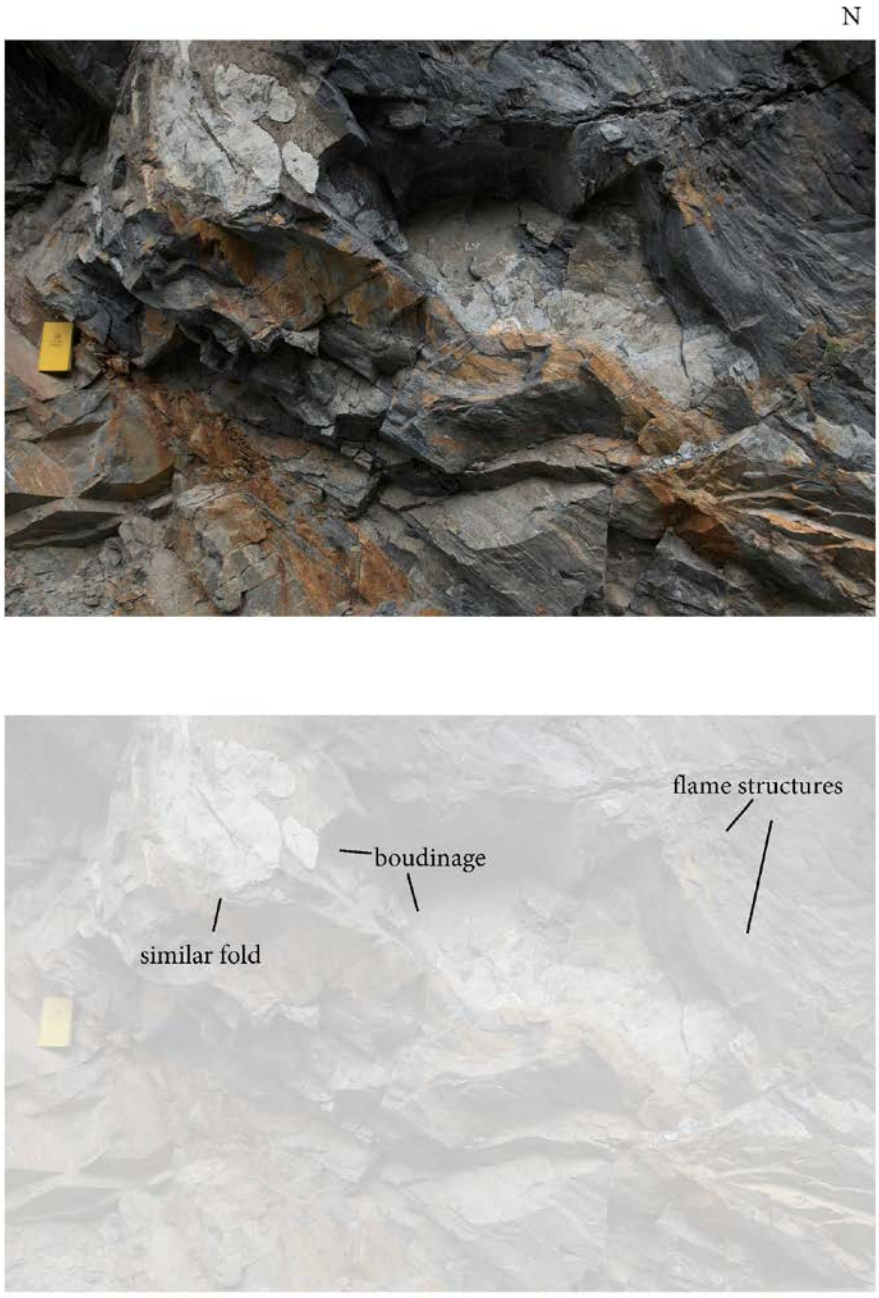

Figure 4.3 continued

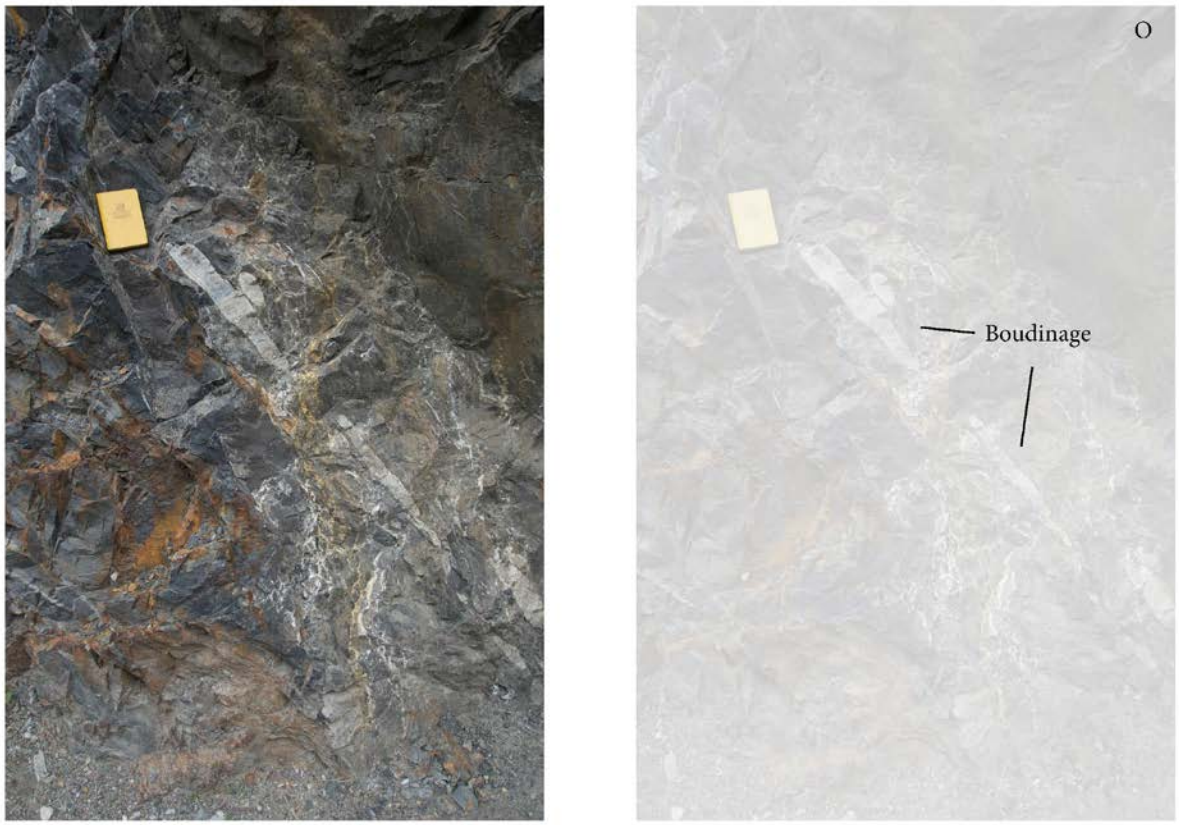

Figure 4.3 continued

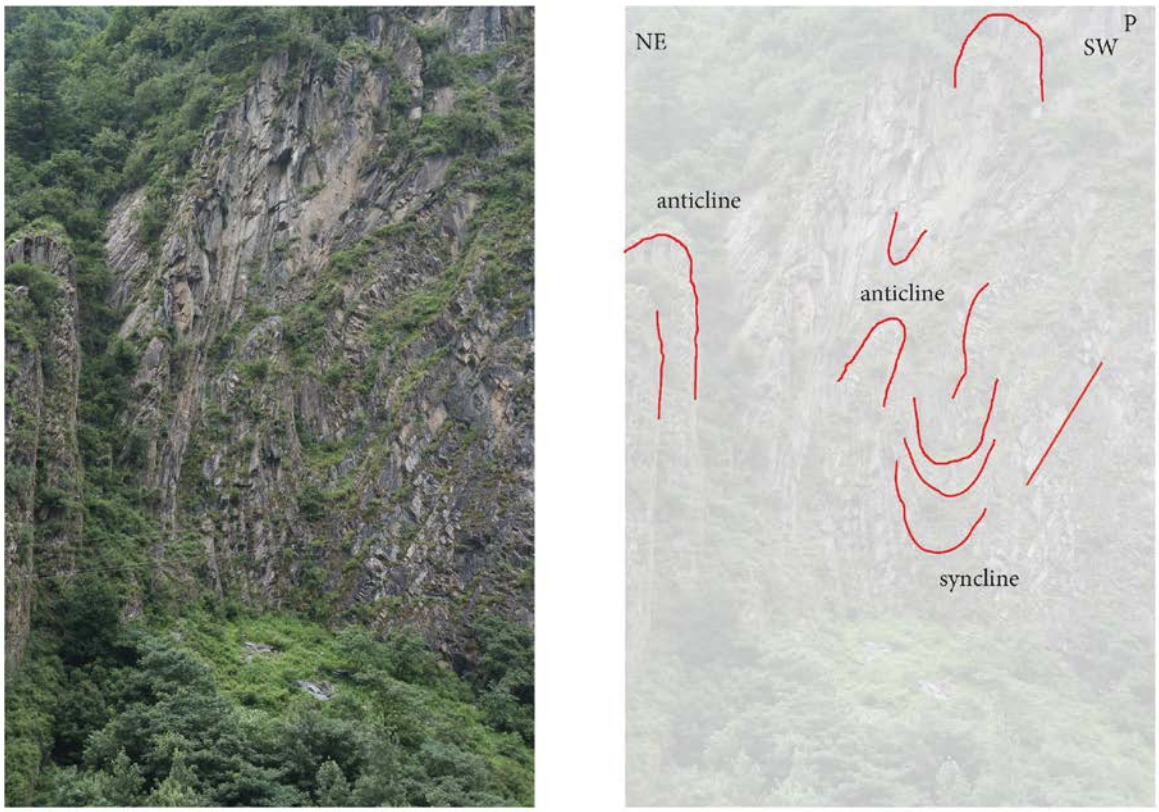

Figure 4.3 continued

4.3.2 Microstructural Work

Nine samples were analyzed using the normalized fry method. This method quantifies anticlustering of distributions of clast centers to estimate the strain ellipse in collected samples (Erslev, 1988; Long et al, 2011a). Each single analysis required graphically logging the short and long axes of ~100 quartz clasts from a thin section image. The axes vectors were input in a Matlab Algorithm. Outputs collected for this study were the Rs values for each sample.

Five samples were analyzed for the Rf/phi method. This method quantifies strain in quartz clasts that are isolated within matrix minerals such as micas in order to provide an

estimate of the strain ellipsoid. The angle of the long axes of the quartz clasts relative to the horizontal and the ratio of long to short axes were measured individually ~30 times for each sample. Rf/phi sample measurements were taken in the XZ and XY direction of the sample. XZ plane is cut parallel to lineation or the down dip direction of the sample. All calculations used the apparent dip of the transect which was orientated N 44.6° E

4.3.3 Line Length Balancing and Microstructural Strain Data.

The graphitic quartzite marker layer provides the best opportunity for line length balancing with in Transect AB and the Upper Haimanta exposures within Transect CD. Therefore, we used it and the line length of other strata to construct two line length sections representative of Transect AB and CD (Figure 4.1, Appendix Figure 4.1; McElroy et al., 1990;Fuchs and Linner 1992; Vannay and Steck, 1995, Frank et al., 1995; Corfield and Searle, 2000; Steck, 2003; Epard and Steck, 2008).

4.4 Results

4.4.1 Field Based Mapping and Geology of Study Section AB.

From south to north stratigraphic age generally decreases unless a structure is encountered. The descriptions of the geology will be referenced in regards to their occurrence in the AB transect.

The Haimanta group in the South AB study area, consist of rocks of varying types (Rattan, 1973) such as metapelites, phyllites, metasiltones, graywackes, quartzitites and carbonates and typically experiencing no higher than greenschist facies metamorphism. In South AB around the Ravi River these rocks and prevalent blueish green phyllites represent the Lower Haimantas. Some outcrops show heavy isoclinal folding in these blue-green phyllites with shortening of at least -32% (Figure 4.3I) Grade tends to coarsen upwards towards the

stratigraphically higher Manjir Conglomerate, confirming similar observations made by Frank et al., (1995). The Manjir Conglomerate is distinguishable from the main Haimantas by its thick massive boulder slates, pebbly mudstones, weak stratification, and characteristic blue quartz. Some clasts within the Manjir Conglomerate are ~10 cm long. The Upper Haimantas above the Manjir conglomerate features more greywacke, sandstones and siltstones.. The Manjir Conglomerate is structurally repeated many times in the South AB section. It occurs as the crest of an anticline exposed at Chobia pass. It is not observed farther north. Throughout the region region of its exposure this unit commonly occupies the core of large-scale asymmetric anticlines.

Thin layers of carbonates outcrop in the Upper Haimantas and at times appear near and interlayered with the graphitic quartzite marker horizon. This horizon is highly distinguishable from the rest of the Upper Haimantas by its yellow rusty weathering, even where viewed across km-scale valleys (Figure 4.3C). The graphitic quartzite marker layer zone is further characterized by graphite, sericite, and pyrite in the adjacent carbonate layers. Weathering of pyrite accomplishes the rusty yellow coloration of outcrops associated with the interlayered quartzite marker zones and carbonate rocks. Sericite schist is also locally associated with the graphitic quartzite marker layer. Focused deformation along relatively weak sericite layers accomplishes imbricate-style thrust deformation (Figure 4.3K) The carbonate layers within the Upper Haimantas experience folding as well and show alternations of light and blueish appearance. In some areas the carbonate layers repeat, marking folding and/or faulting of the layers. This is clearly evident on the South AB transect (Figure 4.3K) Carbonate layers were not as commonly observed in North AB as they were in the South AB. One apparently coherent outcrop lies right beneath the graphitic quartzite layer in the central section of AB (Figure 4.3C). There are places where the carbonate occurs, but graphitic quartzite or the sericitic layers are not visible in the

Upper Haimantas. In these instances monotonous greywacke, siltstone and mudstones are dominant.

The bedding in the South AB portion of the section typically dips to the NE. Folding and fault imbrication is top-to-the-southwest, as shown by the vergence of fault-related folds within the South AB area. The graphitic quartzite layer, carbonates and black slates of the Haimanta unit (see below) assist in the observation of many structures and repeated strata. Some outcrops of Lower Haimanta show beautiful examples of axial planar cleavage on large amplitude folds. Many varieties of folding are quite prevalent throughout South AB, especially along the route between Bharmour and Kugti. Observed folds types include recumbent, isoclinal, overturned, asymmetrical and chevron. Shearing in micaceous layers is observed in Kugti area in sericite, and black slate, near carbonate rocks (Figure 4.3K). Large scale folding to the east of Bharmour appears cliff side with large 50+ meter large amplitudes. These folds verge to the southwest. Together the structural geometries of southern AB represents a large system of SW verging deformation.

Along the southern flank of the southeast-trending hinterland stretch of the Chandra River, bedding of the Haimanta group dips steeply to the the south, and gradually becomes vertical before dipping to the NE towards the southern end of the transect. Roughly four kilometers north of Chobia Pass, outcrops of Haimanta show apparent structural repitition (Figure 4.3A). Axial planar cleavage is prevalent throughout transect AB. axial planar cleavage can be seen in a SW verging anticline syncline pair separated by an apparent SW verging shear plane (Figure 4.3D). A large shear zone marked with 5 m scale SW verging thrust horses was observed. Small scale folding develops in the footwall of this shear zone near the top of the local ridge. (Figure 4.3B).

The southern end of the CD portion of the transect is dominated by the northeast-verging Tandi Syncline. It is exposed from Rohtang pass through Tandi—from where it derives its name – and for an additional ~15 km to the northwest. In the same region, dextral transpression has been reported, as interpreted from the apparent rotation of lineation in the rocks along a northwest trending zone (Vannay & Steck, 1995). In this same region there is clear indication of deformation with the occurrence of 10 cm scale crenulation type vertical folding in beds. North of the Tandi syncline near Keylong a northeast-verging anticline occurs within the Haimanta sequence rocks. This appears to be a northerly anticline paired with the Tandi Syncline, but is less dramatically visible in the field because of pervasive outcrop-scale folding of the Haimanta rocks and the monotonous nature of the Haimanta stratigraphy versus the distinctive Tandi carbonates. Thus far this fold has only been observed along the upper eastern slope of the Bhaga River.

Further north is the Tapachan Normal fault. It dips to the northeast. Continuing north, the steep Sarchu normal fault is observed with less than 2km of total slip (Webb et al., 2011). The Parang thrust occurs northeast of the Sarchu normal fault and is SW verging. It is included in a progressive imbricate system that encompasses Permian-Jurassic carbonates to the Dutung-Thaktote fault zone further northeast. Within this region the Spiti Synclinorium is crossed. South of / structurally atop the Tso Morari gneiss dome, a recumbent anticline is folded along what is termed the Mata Nappe (Steck, 1998, and Webb et al., 2011). Here the Precambrian-Cambrian Haimanta rocks are overlain unconformably by Permian-Jurassic rocks, similar to the exposures across the Chamba region but distinct from the rich Paleozoic stratagraphic record exposed across the Spiti Synclinorium.

4.4.2 Strain Analysis

Throughout both transects sampling was conducted of the lithologies of the THS. Many samples were not suitable for the employed strain ellipsoid determination methods due to composition and insufficiently large quartz clasts (<15 µm). Successful analyses show top-SW shearing in the majority of samples. Strain rates are given in an Rs-value. Values such as 3 or 2, are considered high strain values in a sample and were likely the result of extreme thinning or flattening. Values close to 1 likely experience minimal strain on a microstructural scale. The results of 3-D rf/phi analyses and transect parallel 2-D normalized fry results are below (Figure 4.4-4.7).

10 specimens from 5 samples were analyzed (Figure 4.4 and 4.5) Sample DD71812-3c is a poorly sorted quartzite, this observation is supported by thin section. The Rs value in the XZ and YZ direction for DD71812-3c is 3.2 ± 0.11 and 2.1 ± 0.21 respectively. Hand sample shows cubic opaque minerals, which are also apparent in thin section (Figure 4.4.). Sample DD71912-10 is a phyllite with what appears to be low-grade metamorphism. A stretching lineation matches the direction of the dip orientation with an azimuth of 132 degrees. The Rs value on the XZ direction is 3.2 ± 0.45 and the RS value in the XY plane is 2.1 ± 0.18 Sample DD72212-3a is a poorly sorted meta-grewacke that exhibits foliation marked by brown possibly iron rich veins. The Rs value is 2.2 ± 0.2 in the XZ direction and 2.4 ± 0.41 in the YZ direction. Sample DD72412-5a was sampled from the Manjir conglomerate and has a Rs value of 2.3 ± 0.3 in the XZ direction and 2.3 ± in the 0.3 in the YZ direction. Sample DD080212-1 was sampled from the Manjir conglomerate along the Ravi River in the south extent of the AB transect. Angular clasts are dominant throughout the sample and make up the bulk of siliciclastics. The Rs value for the XZ plane is 2.6 ± 0.36 and the Rs value for the XY plane is 2.0 ± 0.24.

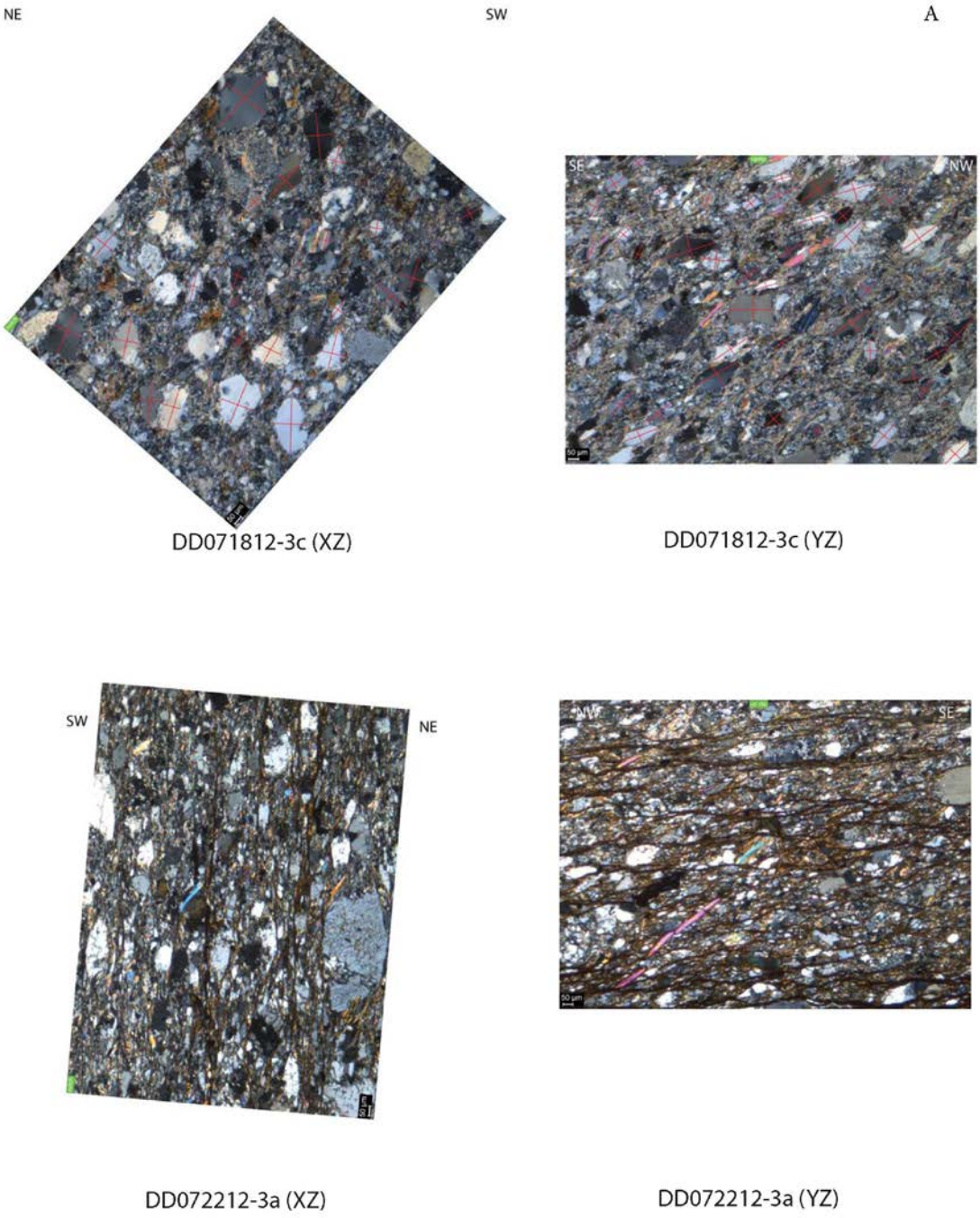

Figure 4.4 Rf/phi sample images.

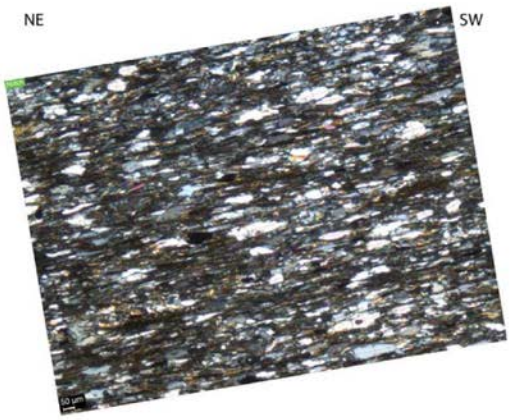

DD071912-10 (XZ)

DD071912-10 (YZ)

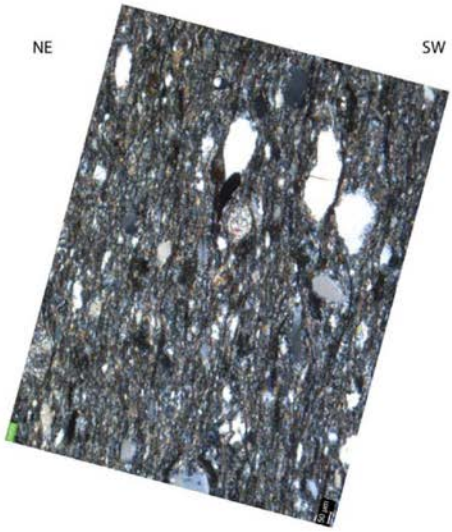

DD072412-5a (XZ)

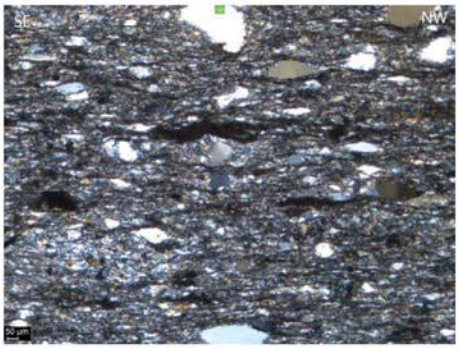

DD072412-5a (YZ)

Figure 4.4 continued

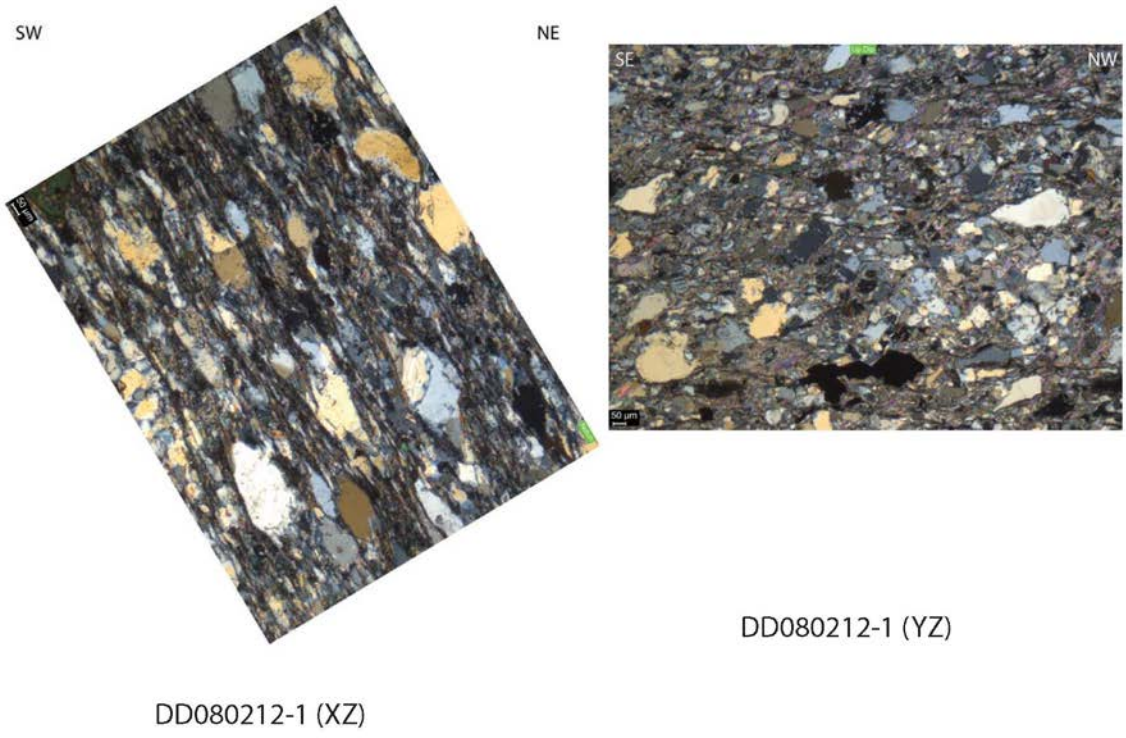

Figure 4.4 continued

Results of the normalized fry analyses taken in the XZ direction of the transect follow (Figure 4.5 and Figure 4.6). The Haimanta sample DD71912-5 has a Rs of 1.09 ± .04. Angular elongated clasts define a weak foliation between small populations of micas. Sample dd71912-6, another from the Haimanta—is a greywacke with top to the north shear sense, which was sampled from the top limb of a flexural slip fold. It has an Rs of 1.24 ± .04. Sample dd71912-7, another from the Haimanta is from a SW dipping fold limb with an Rs value of 1.07 ± .02. Whether or not this fold is flexural slip in nature or similar is hard to determine due to the extent of brittle deformation present. Sample dd72012-6, a sandstone sample within the Haimanta, has an Rs value of 1.14 ± .02. Sample dd73012-6b is a well sorted sandstone taken near heavily sheared zones of phyllite and sandstone. It has an Rs value of 1.12 ± .03.

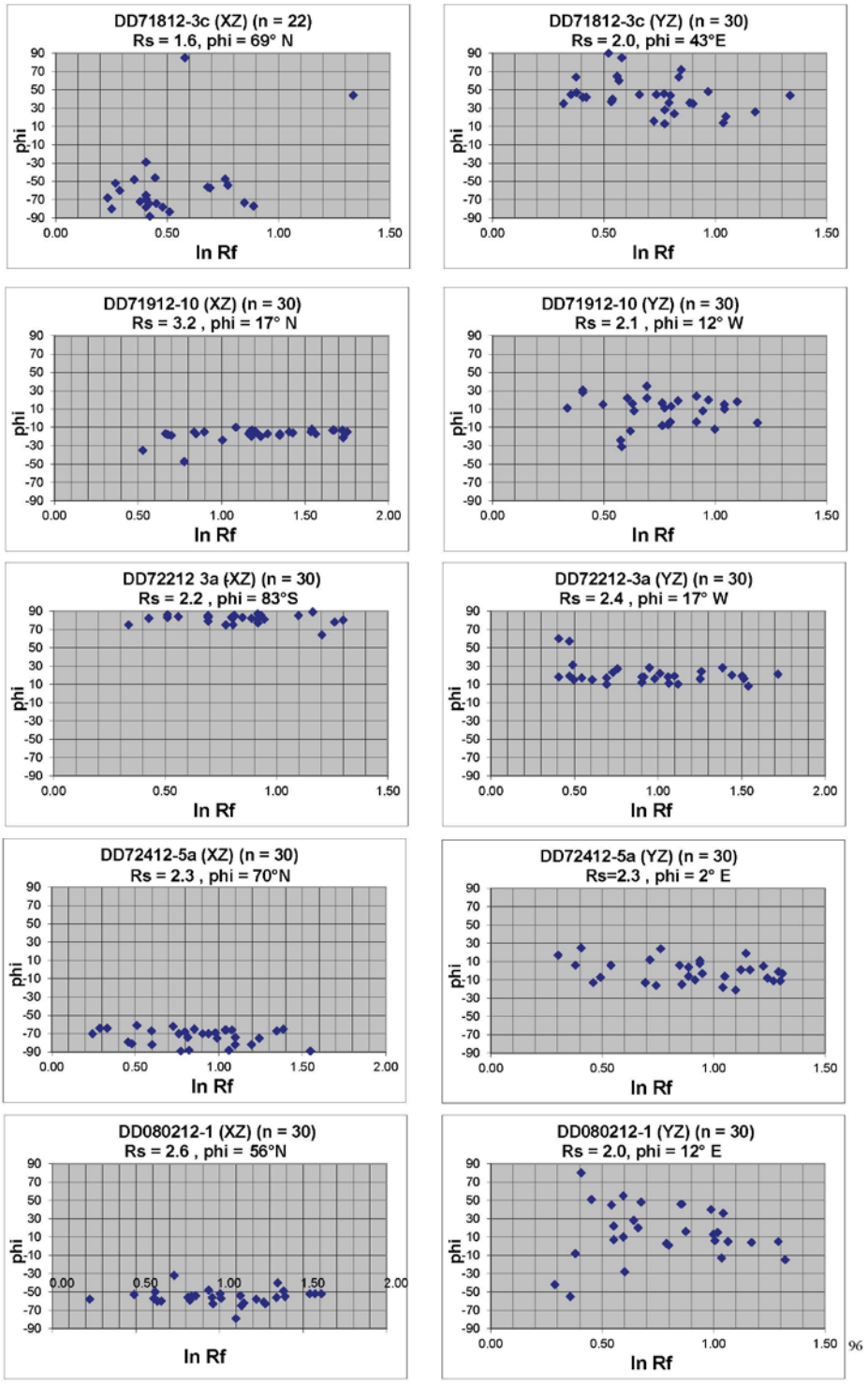

Figure 4.5 Rf-phi axial ratios and long axis orientations relative to the horizontal were used to produce the Rf-phi pot. IN the XZ plane negative phi values dip to the north, while positive values dip to the south. The XY plane expresses E-W dip directions.

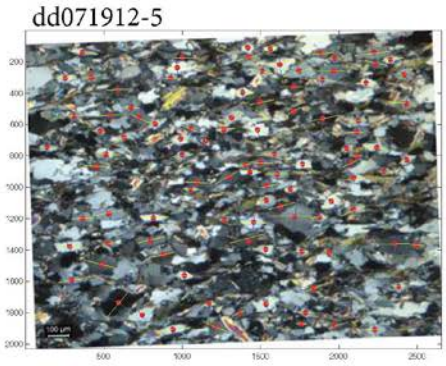

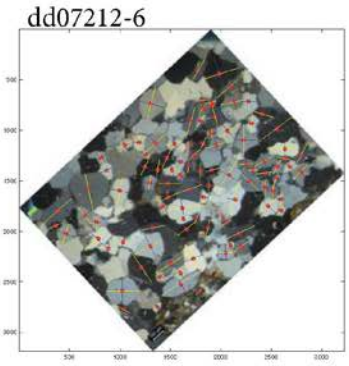

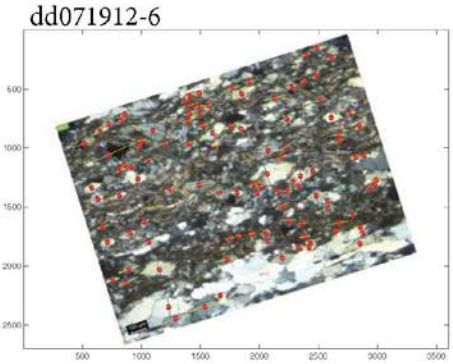

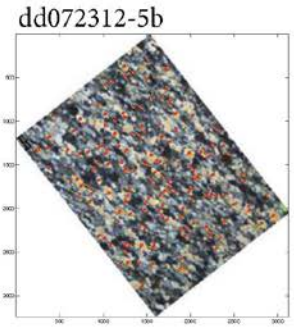

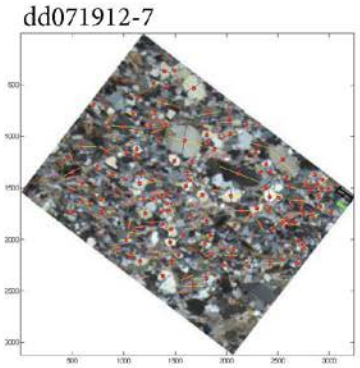

Figure 4.6 Normalized Fry Analysis Images

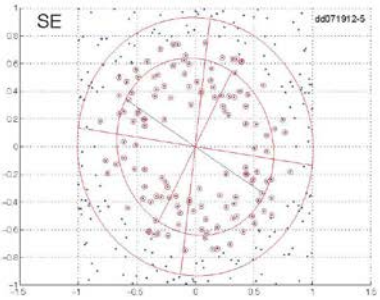

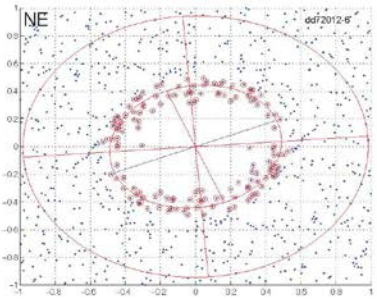

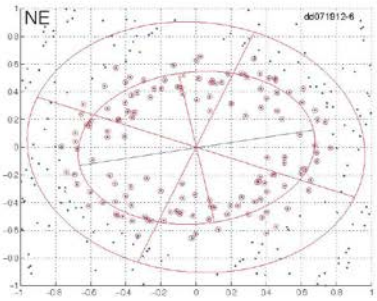

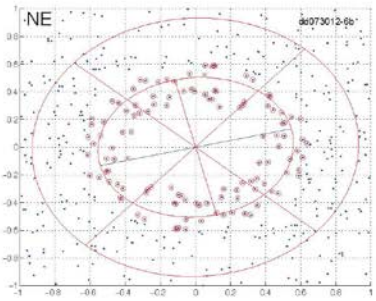

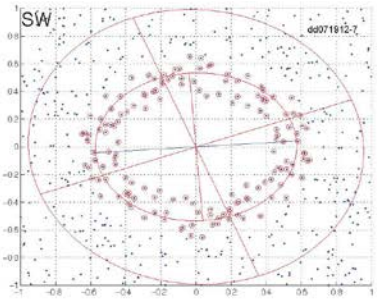

Figure 4.7 Normalized Fry strain results for six clasts dominated samples. Small blue and red lines are principle strain axes.

4.4.3 Microstructures and Regional Structures

To evaluate which type of balancing technique is most appropriate for a particular region, the variability of regional structures was taken into account. Where available, microstructures were paired with the outcrop scale structures to determine a suitable balancing technique. In the southern half of the transect AB, similar folding dominates over flexural slip folding. This is particularly apparent within the upper Haimanta, where carbonates, slates, and shales are common (Figure 4.3). Brittle deformation is pervasive where DD71812-3c was sampled. There appears to be a 2.5-meter wide isoclinal fold, which has been subjected to brittle deformation. The fold doesn't display characteristics of similar folding at outcrop scale. However, microstructures of DD71812-3c indicate that the Rs value in the YZ direction is greater than that of the XZ direction, which indicates a component of flattening strain (Figure 4.8).

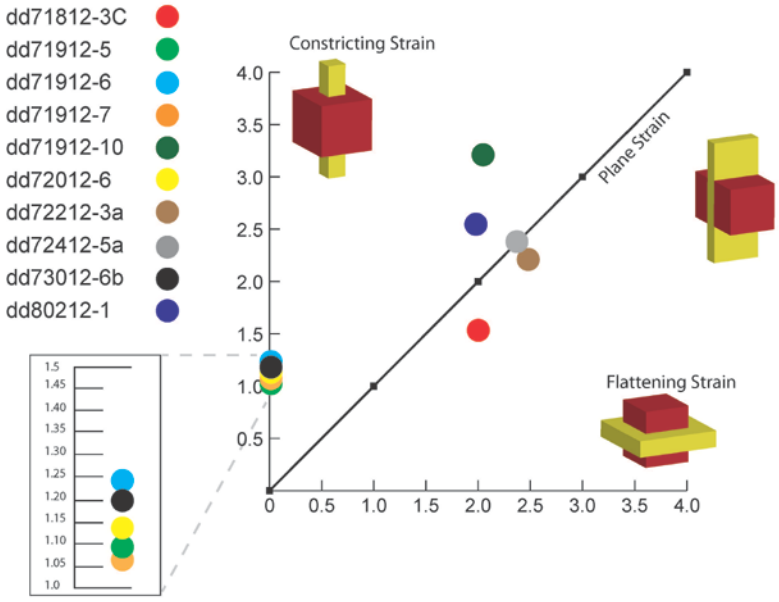

Figure 4.8 Flinn Diagram of Rs Values

Flexural slip and similar folding are apparent in the sampling area of DD71912-5. Here the rocks experienced crenulation folding with fold amplitudes of ~10 cm. DD71912-5's low XY-Rs value of 1.09 ± .04 doesn't suggest any large amounts of simple shear within these rocks or any evidence of significant thinning. DD71912-6 samples the limb of a fold, making it a good candidate to investigate fold type vs microstructural strain. Its XZ-Rs value of ~1.24 may indicate general shear occurred. DD71912-7 occurs in a similar fold. However, with its low XZ-Rs value of 1.07 it may not have been subject to much flexural flow. The area where this sample was collecteddisplays only a minimal similar folding component. Sample DD71912-10 has the highest strain with an XZ-Rs of ~3.2 and XY-Rs of 2.1. This naturally plots in the field of constriction in the Flinn diagram, which suggests that the sample was subject to layer-parallel-stretching rather than layer parallel flattening, and thinning consistent with similar folding.

DD72012-6 was sampled from an unknown subgroup of the Haimanta in depositional contact with a sandstone. Outcrop structures are consistent with minimal strain in the XZ direction, which is supported by RS value of 1.14 for DD72012-6. The outcrop location for DD72212-3a consists of slicken fibers that indicate local transport sub-parallel to the dip direction of the rock. Rs values observed in DD72212-3a are fairly close to plane strain. DD72412-5a is from the north limb of large anticline that makes up most of the Chobia ridge crest. Like the previous sample, the Rs values of this sample plot near the field of plane strain in the flinn diagram (Figure 4.8). No diagnostic features were observed on the outcrop scale to provide more microstructural context. DD73012-6b was sampled from an outcrop that contains small scale similar folding, boudinage and an intricate flame structure easily identified by color contrasts (Figure 4.3N). Sample DD080212-1 was taken from the Manjir conglomerate and shows constrictional strain (Figure 4.8).

4.4.4 Cross Sections

As summarized above the geology of transect AB consist primarily of the Haimanta group. The graphitic quartzite layer of the upper Haimanta was used as a marker layer to construct a line length balance of the Haimanta group since it is the most distinct layer that can be traced definitively throughout the relatively monotonous Haimanta Group strata (Figure 4.3). The outcrop of the marker layer was cross referenced with previous publications where Chobia Pass was traversed (Fuchs and Linner, 1992, Frank et al., 1995). Transect AB's deformed length of the graphitic quartzite layer is approximately 61 km. The restored line length of the same segment is 96 km. This equates to shortening of at least -38% in the upper Haimanta. In transect CD-EF the line length balance was measured from the top of the Haimanta formation since this region of the study had lower control on confirmed exposures of the Graphitic quartzite layer. The total undeformed distance is 147 km while the restored line length is 266 km. This equates to a shortening of at least - 44%. (Appendix 4.1). The total of both transects equate to 208 km of shortened section and 364 km of restored line length section for an approximate shortening of -43%.

4.5 Discussion and Conclusions

In this study we conducted strain analyses in the form of Rf/phi and normalized fry strain measurements that varied in terms of elongation and flattening; line-length balancing and reconstruction assessments through regional cross sections give estimations on the shortening accomplished in the THS; field mapping which confirmed the existence of continuous THS throughout the transects. All are discussed in further detail below.

4.5.1 Shortening Budget

Field mapping of the THS in the Lahaul-Chamba region was aimed to provide additional constraints on the shortening budget of India-Asia convergence. Line length shortening estimates of outcrop exposures are a minimum of -27% between Bharmour and Kugti to the east (Figure 4.3E). Along the Ravi River, isoclinal folds in outcrop experience a minimum of -32% shortening (Figure 4.3H and Figure 4.3I). Large scale isoclinal folding throughout the region may signal even greater shortening. Fault imbrication in the mica and shale rich strata in the south near the Kugti area may require additional shortening considerations (Figure 4.3K). The graphitic quartzite marker layer appears many times through the AB transect and at times in the same orientation while outcropped on the same limb of a regionally large fold (Figure 4.3B and Figure 4.3C). This relationship is interpreted as internal isoclinal folding within the km-scale regional anticline. This would suggest a large amount of shortening, the extent of which is unknown. For the southern AB transect, a shortening estimate of 30-40% would be conservative. The northern components of the study, transects CD and EF experienced lower control for graphitic quartzite outcrop exposures, however is expected to be exposed in the southern half of transect CD near the Chandra Bhaga River. Brittle deformation observed in the CD and EF transects were not readily intact to restore on a fine scale as the folds and deformation seen in the AB transect. Additional trouble occurs north of Sarchu where carbonates from the Tandi formation are pervasive and thick making stratigraphic marker horizons hard to identify.

Pairing the microstructural data with the deformation styles observed in sampled outcrop revealed that deformation styles vary throughout the length of the transect. Samples that were analyzed via the Normalized Fry method experienced stress that is mostly consistent with plane

strain. There were no examples that had a high component of flattening vs constriction. One sample in particular plotted perfectly with plane strain. One outlier had a higher component of constriction (green dot Figure 4.8). Rs/Phi samples analyzed in only the XZ direction have low Rs values not exceeding 1.5. Considering these samples were sampled in outcrops where shear structures are common, we concluded that the component of YZ stretching/flattening would be minimal and didn't include them in this study.

The presence of similar folding and brittle flexural slip type folding in the transect is of particular importance to the impact of our microstructural sampling. Original sampling plans involved a higher sampling density than what was actually permitted in the study and cannot account for a suitable assessment of a fold structure. Similar folds (flexural flow) experience thickening at the fold hinge and thinning at the fold limbs. Flexural slip folds on the other hand retain bedding thickness as folding and slip is accomplished between bedding planes. Microstructural particles behave differently between the two types but in reality some may have experience components of both in neutral surface folds (Figure 4.9). This invites even more uncertainty when evaluating the microstructural strain. In neutral surface folds the neutral surface encounters no strain, however on the margins the strain is either compressive or extensional in the X direction or opposite in the Z direction. If investigations on neutral surface folds and these features were not accounted for, it is probable that strain measurements would be assessed incorrectly.

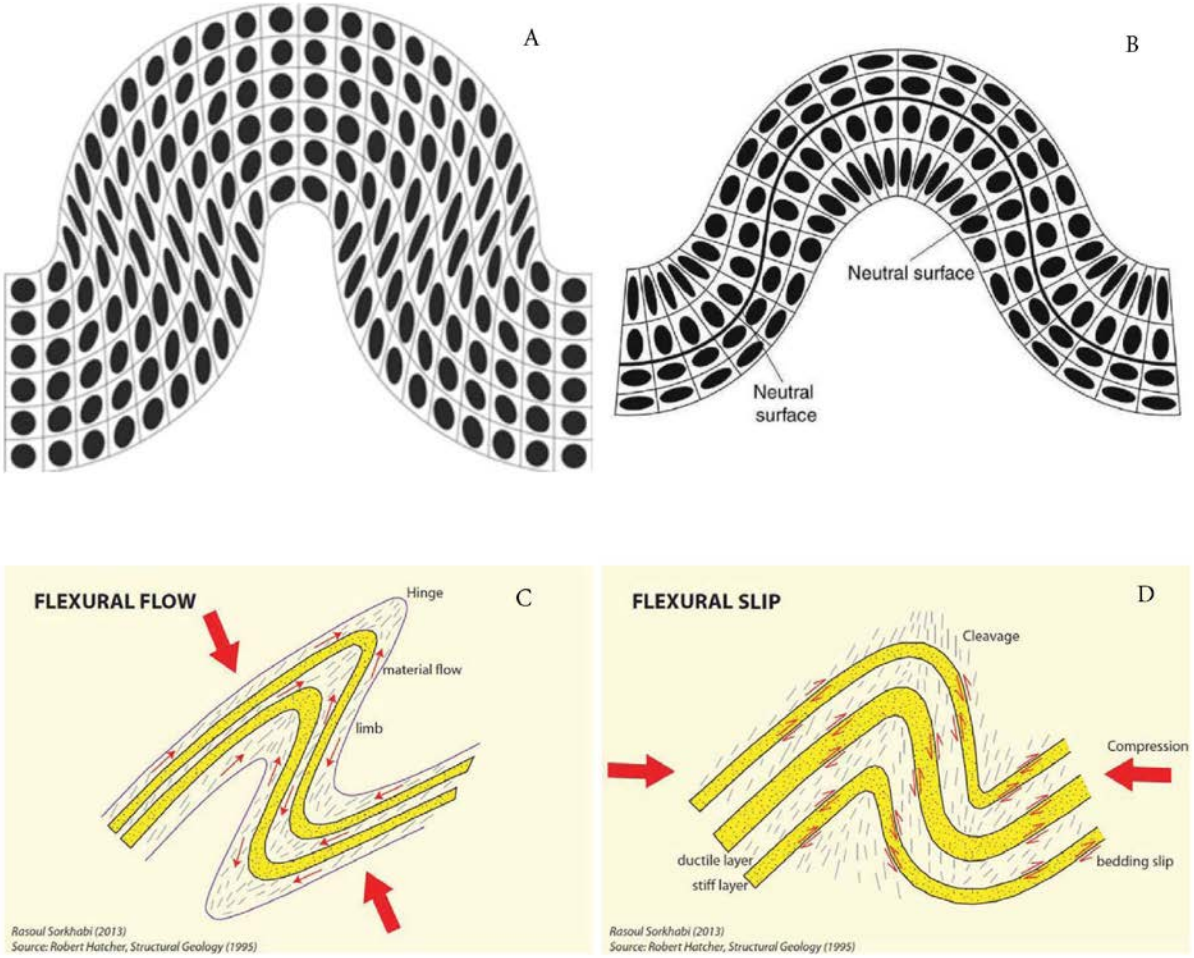

Figure 4.9 Fold models showing the difference in behavior at the microstructural level. A) Flexural slip or parallel folding retains bedding thickness but eventhough microstructural deformation occurs. B) neutral face folding involves changes in bedding thickness in various parts of the fold while retaining a neutral surface that experience no strain. C) Flexural flow is similar to neutral surface folding in that strain is partitioned differently in the hinges versus the limbs of the fold. D) Alternate illustration of a flexural slip fold. Notice bedding thickness continuity.

4.5.2 Implications for Extrusion Models.

Extrusion models were tested by investigating the tectonostratigraphy throughout the transect. The wedge extrusion and channel flow models predict infrastructure emplacement at the ground within the proposed transect to coincide with along strike exposures to the northwest and southeast (Figure 4.1). However this observation was not made. Along the transect only brittle – low temperature deformation and lithologies were observed. Rocks we consider infrastructure rocks, were observed in lower elevations cut by the east-west flowing Chandra River (Figure 4.1) but never cross-cut the stratigraphic surface of the THS rocks. This relationship agrees with the field relationships seen at Rhotang pass. (Webb et al., 2011). There the THS rocks sit subhorizontally above infrastructure rocks. Considering Rhotang pass lies just south of the Chandra River; no THS rocks were observed being crosscut by infrastructure rocks, the conclusion is made that wedge extrusion and channel flow are not viable models for infrastructure emplacement.

4.5.3 Greater Indian Basin Model Implications

An important prediction of the GIB model requires two suture zones within the Himalaya representing the rifted components of the northern Indian margin; 1) collision of the rifted Tethyan subcontinent followed by; 2) the collision of the Indian continent, which should place the suture zone within or beneath the GHC. The Indus Suture Zone represents the location of the first collision, while the second has no confirmed location. The result of this study hasn't confirmed prospect for the second suture zone. Evidence of a subduction zone such as ophiolites, mélange, subduction related molasses and flysch were not observed throughout the transect south of the Indus Suture Zone. The confirmed geometry of the continuous THS overlying the GHC as expressed in the Tectonic Wedging model does not predict a suture zone

as well. Though a cryptic suture zone may exist. Additionally the shortening estimates of the GIB model were not supported by our shortening and strain analyses. We conclude that the geology of the THC does not support the predictions of the Greater Indian Basin model. Future investigations involving assessing the shortening budget with the assistance of microstructural analysis should be highly detailed on the microstructural level. As discussed above there is inherent uncertainty that must be considered, but it is possible that much insight will be gained about how shortening relates to the geo-micromechanics of rocks on a meso-scale.

CHAPTER 5
SUMMARY AND CONCLUSIONS

This dissertation consists of projects that investigate the low and high temperature deformation that took place during various stages of Himalayan development. Two projects investigated the UHP record of the Himalaya to gain a better understanding of Himalayan UHP timing and collision timing involving the Indian continent (Chapter 2 and 3). To approach these questions, mapping, petrologic and geochronologic investigations were conducted. The final project looked investigate how the geometry of the low and high grade rocks that make up the Himalaya were emplaced, as well as assessing the shortening that was involved (Chapter 4). It involved field mapping in two regional field areas, microstructural analysis, and line-length balancing efforts. Below, I summarize the main conclusions of these chapters.

5.1 UHP Metamorphism in the Himalaya

Sampling, and U-Pb age analyses of zircon, rutile and zircon provided a relatively large data set compared to previous UHP work in the Tso Morari, UHP terrane in NW Himalaya Ladakh, India. Previous work, predicted a 53 Ma UHP age and a 50 UHP age informed by U-Pb zircon analyses. In chapter 1, U-Pb geochronology along with coupled Rare Earth Element analyses were conducted to provide an UHP age of ~46 Ma. Consistent with the other UHP terrane in the Himalayan, Kaghan Valley. Rutile analyzed in chapter 3 provided two older U-Pb ages ~50 and ~47 Ma. This has been interpreted as prograde-prograde ages. The amount of analyses taken in all the studies leads us to favor the ~46 Ma UHP age informed by the zircon from chapter 2. The possibility of prograde rutile in the region is profound and allows the timing of metamorphic events in Tso Morari to be constrained further. Additionally, the apparent contemporaneous nature of Tso Morai and Kaghan Valley UHP suggests contemporaneous collision timing along the NW Indian margin in the Cenozoic.

5.2 GIB and Himalayan Development Models

Structural mapping, microstructural analysis and line-length balancing was conducted on rocks along a transect from Chamba region to the Tso Morari region. The purpose was to test the two collision GIB model as well as the emplacement of the high grade infrastructure relative to its overlying superstructure. The tectonic wedging was the most consistent with the geology that was mapped, in that there was no evidence of the GHC cross cutting the THS along the investigated transect. This relationship along with line length balancing in the NW Himalayan region showed no evidence in support of the GIB model. With the intact low-grade THS along the transect, the plausibility of a collision within or beneath it is not consistent with our field mapping.

REFERENCES

Beaumont, C., Jamieson, R.A., Nguyen, M.H. and Lee, B., 2001. Himalayan tectonics explained by extrusion of a low-viscosity crustal channel coupled to focused surface denudation. *Nature*, *414*(6865), pp.738-742.

Beaumont, C., Jamieson, R.A., Nguyen, M.H. and Medvedev, S., 2004. Crustal channel flows: 1. Numerical models with applications to the tectonics of the Himalayan-Tibetan orogen. *Journal of Geophysical Research: Solid Earth*, *109*(B6).

Beck, R.A., Sinha, A., Burbank, D.W., Sercombe, W.J., and Khan, A.M., 1998, Climatic, oceanographic, and isotopic consequences of the Paleocene India-Asia collision, in Aubry, M.P., et al., eds., Late Paleocene–early Eocene climatic and biotic events in the marine and terrestrial records: New York, Columbia University Press, p. 103–117.

Brookfield, M.E., 1998, The evolution of the great river systems of southern Asia during the Cenozoic India-Asia collision: Rivers draining southwards: Geomorphology, v. 22, p. 285–312, doi:10.1016/S0169-555X(97)00082-2.

Burchfiel, B.C. and Royden, L.H., 1985. North-south extension within the convergent Himalayan region. *Geology*, *13*(10), pp.679-682.

Burchfiel, B.C., Zhiliang, C., Hodges, K.V., Yuping, L., Royden, L.H., Changrong, D. and Jiene, X., 1992. The South Tibetan detachment system, Himalayan orogen: Extension contemporaneous with and parallel to shortening in a collisional mountain belt. *Geological Society of America Special Papers*, *269*, pp.1-41

Butler, J.P., Jamieson, R.A., Steenkamp, H.M. and Robinson, P., 2013. Discovery of coesite–eclogite from the Nordøyane UHP domain, Western Gneiss Region, Norway: field relations, metamorphic history, and tectonic significance. *Journal of Metamorphic Geology*, *31*(2), pp.147-163.

Cai, F., Ding, L., and Yue, Y., 2011, Provenance analysis of Upper Cretaceous strata in the Tethys Himalaya, southern Tibet: Implications for timing of India-Asia collision: Earth and Planetary Science Letters, v. 305, p. 195–206, doi:10.1016/j.epsl.2011.02.055.

Chatterjee, N. and Jagoutz, O., 2015. Exhumation of the UHP Tso Morari eclogite as a diapir rising through the mantle wedge. *Contributions to Mineralogy and Petrology*, *169*(1), pp.1-20.

Cherniak, D.J., 1993. Lead diffusion in titanite and preliminary results on the effects of radiation damage on Pb transport. *Chemical Geology*, *110*(1), pp.177-194.de Sigoyer J., Guillot, S., Lardeaux, J.M., Mascle, G., 1997. Glaucophane-bearing eclogites in the Tso Morari dome (eastern Ladakh, NW Himalaya). European Journal of Mineralogy, 9, 1073-1083

Clyde, W.C., Khan, I.H., and Gingerich, P.D., 2003, Stratigraphic response and mammalian dispersal during initial India-Asia collision: Evidence from the Ghazij Formation, Balochistan, Pakistan: Geology, v. 31, p. 1097–1100, doi:10.1130/G19956.1.

Connolly, J.A.D., 1990. Multivariable phase diagrams; an algorithm based on generalized thermodynamics. *American Journal of Science*, *290*(6), pp.666-718.

Corfu, F., Ravna, E.J.K., Kullerud, K., A Late Ordovician U-Pb age for the Tromsø Nappe eclogites, Uppermost Allochthon of the Scandinavian Caledonides. Contrib. Mineral Petrol. 145, 502-513 (2003)Ludwig, K.R., User's Manual for Isoplot 3.00 a Geochronological Toolkit for Microsoft Excel (2003)

Clift, P.D., Giosan, L., Blusztajn, J., Campbell, I.H., Allen, C., Pringle, M., Tabrez, A.R., Danish, M., Rabbani, M.M., Alizai, A. and Carter, A., 2008. Holocene erosion of the Lesser Himalaya triggered by intensified summer monsoon. *Geology*, *36*(1), pp.79-82.

Corfield, R.I. and Searle, M.P., 2000. Crustal shortening estimates across the north Indian continental margin, Ladakh, NW India. *Geological Society, London, Special Publications*, *170*(1), pp.395-410.

Dahlen, F.A., 1990. Critical taper model of fold-and-thrust belts and accretionary wedges. *Annual Review of Earth and Planetary Sciences*, *18*, p.55.

Davis, D., Suppe, J. and Dahlen, F.A., 1983. Mechanics of fold-and-thrust belts and accretionary wedges. *Journal of Geophysical Research: Solid Earth*, *88*(B2), pp.1153-1172.

DeCelles, P.G., Robinson, D.M., Quade, J., Ojha, T.P., Garzione, C.N., Copeland, P. and Upreti, B.N., 2001. Stratigraphy, structure, and tectonic evolution of the Himalayan fold-thrust belt in western Nepal. *Tectonics*,*20*(4), pp.487-509.

DeCelles, P.G., Kapp, P., Quade, J. and Gehrels, G.E., 2011. Oligocene–Miocene Kailas basin, southwestern Tibet: Record of postcollisional upper-plate extension in the Indus-Yarlung suture zone. *Geological Society of America Bulletin*, *123*(7-8), pp.1337-1362.

DeCelles, P.G., Kapp, P., Gehrels, G.E., and Ding, L., 2014, Paleocene-Eocene foreland basin evolution in the Himalaya of southern Tibet and Nepal: Implications for the age of initial India-Asia collision, Tectonics, v. 33, doi:10.1002/2014TC003522.

de Sigoyer, J., Guillot, S., Lardeaux, J.-M., and Mascle, G., 1997, Glaucophane-bearing eclogites in the Tso Morari dome (eastern Ladakh, NW Himalaya): European Journal of Mineralogy, v. 9, p. 1073–1083.

de Sigoyer, J., Chavagnac, V., Blichert-Toft, J., Villa, I.M., Luais, B., Guillot, S., Cosca, M. and Mascle, G., 2000. Dating the Indian continental subduction and collisional thickening in the northwest Himalaya: Multichronology of the Tso Morari eclogites. *Geology*, *28*(6), pp.487-490.

de Sigoyer, J., Guillot, S., and Dick, P., 2004, Exhumation of the ultrahigh-pressure Tso Morari unit in eastern Ladakh (NW Himalaya): A case study: Tectonics, v. 23, TC3003, doi:10.1029/2002TC001492.

Dodson, M.H., 1973. Closure temperature in cooling geochronological and petrological systems. *Contributions to Mineralogy and Petrology*, *40*(3), pp.259-274.

Donaldson, D.G., Webb, A.A.G., Menold, C.A., Kylander-Clark, A.R. and Hacker, B.R., 2013. Petrochronology of Himalayan ultrahigh-pressure eclogite. *Geology*, *41*(8), pp.835-838.

Dupont-Nivet, G., Lippert, P., van Hinsbergen, D.J.J., Meijers, M.J.M., and Kapp, P., 2010, Paleolatitude and age of the Indo-Asia collision: Paleomagnetic constraints: Geophysical Journal International, v. 182, p. 1189–1198, doi:10.1111/j.1365-246X.2010.04697.x.

Epard, J.-L., Steck, A., 2008. Structural development of The Tso Morari ultra-high pressure nappe of the Ladakh Himalaya. Tectonophysics 451, 242–264.

Epard, J.L. and Steck, A., 2004. The eastern prolongation of the Zanskar shear zone (western Himalaya). *Eclogae Geologicae Helvetiae*, *97*(2), pp.193-212.

Erslev, E.A., 1988. Normalized center-to-center strain analysis of packed aggregates. *Journal of Structural Geology*, *10*(2), pp.201-209.

Frank, W., Hoinkes, G., Miller, C., Purtscheller, F., Richter, W. and Thöni, M., 1973. Relations between metamorphism and orogeny in a typical section of the Indian Himalayas. *Tschermaks mineralogische und petrographische Mitteilungen*, *20*(4), pp.303-332.

Frank, W.O.L.F.G.A.N.G., Grasemann, B.E.R.N.H.A.R.D., Guntli, P.E.T.E.R. and Miller, C.H.R.I.S.T.I.N.E., 1995. Geological Map of the Kishtwar-Chamba-Kulu Region (NW Himalayas, India). *Jahrbuch der Geologischen Bundesanstalt*, *138*(2), pp.299-308.

Fuchs, G.E.R.H.A.R.D. and Linner, M.A.N.F.R.E.D., 1995. Geological traverse across the western Himalaya—a contribution to the geology of eastern Ladakh, Lahul, and Chamba. *Jahrbuch der Geologischen Bundesanstalt*, *138*, pp.665-685.

Gansser, A., 1964. Geology of the Himalayas.

Garzanti, E., Baud, A., and Mascle, G., 1987, Sedimentary record of the northward flight of India and its collision with Eurasia (Ladakh Himalaya, India): Geodinamica Acta, v. 1, p. 297–312.

Girard, M., 2001. *Metamorphism and tectonics of the transition between non metamorphic Tethyan Himalaya sediments and the North Himalayan Crystalline Zone (Rupshu area, Ladakh, NW India).* Section des Sciences de la terre de l'université.

Girard, M. and Bussy, F., 1999. Late Pan-African magmatism in the Himalaya: new geochronological and geochemical data from the Ordovician Tso Morari metagranites (Ladakh, NW India). *Schweizerische mineralogische und petrographische Mitteilungen*, *79*(3), pp.399-418.

Gleeson, T.P. and Godin, L., 2006. The Chako antiform: a folded segment of the Greater Himalayan sequence, Nar valley, Central Nepal Himalaya.*Journal of Asian Earth Sciences*, *27*(5), pp.717-734.

Godin, L., Grujic, D., Law, R.D. and Searle, M.P., 2006. Channel flow, ductile extrusion and exhumation in continental collision zones: an introduction. *Geological Society, London, Special Publications*, *268*(1), pp.1-23.

Guillot, S., De Sigoyer, J., Lardeaux, J.M. and Mascle, G., 1997. Eclogitic metasediments from the Tso Morari area (Ladakh, Himalaya): evidence for continental subduction during India-Asia convergence. *Contributions to Mineralogy and Petrology*, *128*(2-3), pp.197-212.

Guillot, S., Garzanti, E., Baratoux, D., Marquer, D., Mahéo, G., and de Sigoyer, J., 2003, Reconstructing the total shortening history of the NW Himalaya: Geochemistry Geophysics Geosystems, v. 4, 1064, doi:10.1029/2002GC000484.

Guillot, S., Replumaz, A., Hattori, K.H., and Strzerzynski, P., 2007, Initial geometry of western Himalaya and ultrahigh-pressure metamorphic evolution: Journal of Asian Earth Sciences, v. 30, p. 557–564, doi:10.1016/j.jseaes.2007.01.004.

Hacker, B.R. and Gerya, T.V., 2013. Paradigms, new and old, for ultrahigh-pressure tectonism. *Tectonophysics*, *603*, pp.79-88.

Harrison, T.M., Yin, A., Grove, M., Lovera, O.M., Ryerson, F.J. and Zhou, X., 2000. The Zedong Window: A record of superposed Tertiary convergence in southeastern Tibet. *Journal of Geophysical Research: Solid Earth*,*105*(B8), pp.19211-19230

He, D., Webb, A.A.G., Larson, K.P., Martin, A.J. and Schmitt, A.K., 2015. Extrusion vs. duplexing models of Himalayan mountain building 3: duplexing dominates from the Oligocene to Present. *International Geology Review*,*57*(1), pp.1-27.

Heim, A. and Gansser, A., 1939. Central Himalaya.

Hodges, K.V., Parrish, R.R., Housh, T.B., Lux, D.R., Burchfiel, B.C., Royden, L.H. and Chen, Z., 1992. Simultaneous Miocene extension and shortening in the Himalayan orogen. *Science*, *258*(5087), pp.1466-1470.

Hodges, K.V., Parrish, R.R. and Searle, M.P., 1996. Tectonic evolution of the central Annapurna range, Nepalese Himalayas. *Tectonics*, *15*(6), pp.1264-1291

Hodges, K.V., 2000. Tectonics of the Himalaya and southern Tibet from two perspectives. *Geological Society of America Bulletin*, *112*(3), pp.324-350.Hodges, K.V., Hurtado, J.M. and Whipple, K.X., 2001. Southward extrusion of Tibetan crust and its effect on Himalayan tectonics. *Tectonics*, *20*(6), pp.799-809.

Jessup, M.J., Newell, D.L., Cottle, J.M., Berger, A.L. and Spotila, J.A., 2008. Orogen-parallel extension and exhumation enhanced by denudation in the trans-Himalayan Arun River gorge, Ama Drime Massif, Tibet-Nepal.*Geology*, *36*(7), pp.587-590.

Kaneko Y, Katayama,I, Yamamotot, H, Misawa, K, Ishikawa, M, Rehman, H.U., Kausar, A.B., Shiraishi, K., 2003. Timing of Himalayan Ultrahigh-pressure metamorphism: sinking rate

and subduction angle of the Indian continental crust beneath Asia. Journal of Metamorphic geology 21, 589-599

Kellett, D.A. and Grujic, D., 2012. New insight into the South Tibetan detachment system: Not a single progressive deformation. *Tectonics*, *31*(2).

Kohn, M.J., 2008. PTt data from central Nepal support critical taper and repudiate large-scale channel flow of the Greater Himalayan Sequence.*Geological Society of America Bulletin*, *120*(3-4), pp.259-273.

Konrad-Schmolke, M., O'Brien, P.J., de Capitani, C., and Carswell, D.A., 2008, Garnet growth at high- and ultra-high pressure conditions and the effect of element fractionation on mineral modes and composition: Lithos, v. 103, p. 309–332, doi:10.1016/j.lithos.2007.10.007.

Kylander-Clark, A.R.C., Hacker, B.R. and Mattinson, J.M., 2008. Slow exhumation of UHP terranes: titanite and rutile ages of the Western Gneiss Region, Norway. *Earth and Planetary Science Letters*, *272*(3), pp.531-540.

Kylander-Clark, A.R., Hacker, B.R. and Mattinson, C.G., 2012. Size and exhumation rate of ultrahigh-pressure terranes linked to orogenic stage.*Earth and Planetary Science Letters*, *321*, pp.115-120.

Jackson, S. E., Pearson, N. J., Griffin, W. L., Belousova, E. A., The application of laser ablation-inductively coupled plasma-mass spectrometry to in situ U-Pb zircon geochronology. Chemical Geology 211, 47-69 (2004).

Le Fort, P., 1975. Himalayas: the collided range. Present knowledge of the continental arc. *American Journal of Science*, *275*(1), p.44.

Leech, M.L., Singh, S., Jain, A.K., Klemperer, S.L. and Manickavasagam, R.M., 2005. The onset of India–Asia continental collision: early, steep subduction required by the timing of UHP metamorphism in the western Himalaya. *Earth and Planetary Science Letters*, *234*(1), pp.83-97.

Leech, M.L., Singh, S., and Jain, A.K., 2007, Continuous metamorphic zircon growth and interpretation of U-Pb SHRIMP dating: An example from the Western Himalaya: International Geology Review, v. 49, p. 313–328, doi:10.2747/0020-6814.49.4.313.

Lister, G.S., Forster, M.A., and Rawling, T.J., 2001, Episodicity during orogenesis, in Miller, J.A., et al., eds., Continental reactivation and reworking: Geological Society of London Special Publication 184, p. 89–113, doi:10.1144/GSL.SP.2001.184.01.06.

Long, S. and McQuarrie, N., 2010. Placing limits on channel flow: Insights from the Bhutan Himalaya. *Earth and Planetary Science Letters*, *290*(3), pp.375-390.

Long, S., McQuarrie, N., Tobgay, T. and Grujic, D., 2011. Geometry and crustal shortening of the Himalayan fold-thrust belt, eastern and central Bhutan. *Geological Society of America Bulletin*, pp.B30203-1.

Ludwig, K.R., 2003. *User's manual for Isoplot 3.00: a geochronological toolkit for Microsoft Excel* (No. 4). Kenneth R. Ludwig.

Ludwig, K.R., 2009. Isoplot 4.1. A geochronological toolkit for Microsoft Excel. *Berkeley Geochronology Center Special Publication*, *4*, p.76.

Mahéo, G., Bertrand, H., Guillot, S., Villa, I.M., Keller, F., and Capiez, P., 2004, The south Ladakh ophiolites (NW Himalaya, India): An intraoceanic tholeiitic origin with implication for the closure of the Neo-Tethys: Chemical Geology, v. 203, p. 273–303, doi:10.1016/j.chemgeo.2003.10.007.

McElroy, R., Cater, J., Roberts, I., Peckham, A. and Bond, M., 1990. The structure and stratigraphy of SE Zanskar, Ladakh Himalaya. *Journal of the Geological Society*, *147*(6), pp.989-997.

Mukherjee, B.K. and Sachan, H.K., 2001. Discovery of coesite from Indian Himalaya: a record of ultra-high pressure metamorphism in Indian continental crust. *CURRENT SCIENCE-BANGALORE-*, *81*(10), pp.1358-1360.

Mukherjee, B.K. and Sachan, H.K., 2009. Fluids in coesite-bearing rocks of the Tso Morari Complex, NW Himalaya: evidence for entrapment during peak metamorphism and subsequent uplift. *Geological Magazine*, *146*(06), pp.876-889.

Najman, Y., 2006, The detrital record of orogenesis: A review of approaches and techniques used in the Himalayan sedimentary basins: Earth-Science Reviews, v. 74, p. 1–72, doi:10.1016/j.earscirev.2005.04.004.

Najman, Y., Appel, E., Boudagher-Fadel, M., Bown, P., Carter, A., Garzanti, E., Godi, L., Han, J., Liebke, U., Oliver, G., Parrish, R., and Vezzoli, G., 2010, Timing of India-Asia collision: Geological, biostratigraphic, and paleomagnetic constraints: Journal of Geological Research, v. 115, B12416, doi:10.1029/2010JB007673.

Nanda, M.M. and Singh, M.P., 1976. Stratigraphy and sedimentation of the Zanskar area, Ladakh and adjoining parts of the Lahaul region of Himachal Pradesh. *Him. Geol*, *6*, pp.365-388.

Parrish, R.R., Gough, S.J., Searle, M.P., and Waters, D.J., 2006, Plate velocity exhumation of ultrahigh-pressure eclogites in the Pakistan Himalaya: Geology, v. 34, p. 989–992, doi:10.1130/G22796A.1.

Paton, C., Woodhead, J.D., Hellstrom, J.C., Hergt, J.M., Greig, A. and Maas, R., 2010. Improved laser ablation U-Pb zircon geochronology through robust downhole fractionation correction. *Geochemistry, Geophysics, Geosystems*, *11*(3).

O'Brien, P.J., 2006, The age of deep, steep continental subduction in the NW Himalaya: Relating zircon growth to metamorphic history: Comment on The onset of India-Asia continental collision: Early, steep subduction required by the timing of UHP metamorphism in the western Himalaya: Earth and Planetary Science Letters, v. 245, p. 814–816, doi:10.1016/j.epsl.2006.03.033.

O'Brien, P.J., Zotov, N., Law, R., Khan, M.A., and Jan, M.Q., 2001, Coesite in Himalayan eclogite and implications for models of India-Asia collision: Geology, v. 29, p. 435–438, doi:10.1130/0091-7613(2001)029<0435:CIHEAI>2.0.CO;2.

Rattan, S.S., 1973. Stratigraphy and sedimentation of the Chamba area, western Himachal Pradesh. *Him. geol*, *3*, pp.231-248.

Raymo, M.E., Ruddiman, W.F., and Froelich, P.N., 1988, Influence of the late Cenozoic mountains building on ocean geochemical cycles: Geology, v. 16, p. 649–653, doi:10.1130/0091-7613(1988)016<0649:IOLCMB>2.3.CO;2.

Raymo, M.E., and Ruddiman, W.F., 1992, Tectonic forcing of late Cenozoic climate: Nature, v. 359, p. 117–122, doi:10.1038/359117a0.

Robinson, D.M., DeCelles, P.G. and Copeland, P., 2006. Tectonic evolution of the Himalayan thrust belt in western Nepal: Implications for channel flow models. *Geological Society of America Bulletin*, *118*(7-8), pp.865-885.

Rowley, D.B., 1996, Age of collision between India and Asia: A review of the stratigraphic data: Earth and Planetary Science Letters, v. 145, p. 1–13, doi:10.1016/S0012-821X(96)00201-4.

Sachan, H.K., Mukherjee, B.K., Ogasawara, Y., Maruyama, S., Ishida, H., Atsumi, M.U.K.O. and Yoshioka, N., 2004. Discovery of coesite from Indus Suture Zone (ISZ), Ladakh, India Evidence for deep subduction. *European Journal of Mineralogy*, *16*(2), pp.235-240.

Schlup, M., Carter, A., Cosca, M. and Steck, A., 2003. Exhumation history of eastern Ladakh revealed by 40Ar/39Ar and fission-track ages: the Indus River–Tso Morari transect, NW Himalaya. *Journal of the Geological Society*,*160*(3), pp.385-399.

Schoene, B., Condon, D.J., Morgan, L. and McLean, N., 2013. Precision and accuracy in geochronology. *Elements*, *9*(1), pp.19-24.

Searle, M.P., Stephenson, B., Walker, J. and Walker, C., 2007. Restoration of the Western Himalaya: implications for metamorphic protoliths, thrust and normal faulting, and channel flow models. *Episodes*, *30*(4), p.242.

Searle, M.P., 2010. Low-angle normal faults in the compressional Himalayan orogen; Evidence from the Annapurna–Dhaulagiri Himalaya, Nepal.*Geosphere*, *6*(4), pp.296-315.

Slama, J., Kosler, J., and Condon, D.J.,Plesovice zircon–A new natural reference material for U-Pb and Hf isotopic microanalysis: Chemical Geology, v. 249, p, 1- 35 (2008)

Spencer, K.J., Hacker, B.R., Kylander-Clark, A.R.C., Andersen, T.B., Cottle, J.M., Stearns, M.A., Poletti, J.E. and Seward, G.G.E., 2013. Campaign-style titanite U–Pb dating by laser-ablation ICP: implications for crustal flow, phase transformations and titanite closure. *Chemical Geology*, *341*, pp.84-101.

Spring, L., Bussy, F., Vannay, J.C., Huon, S. and Cosca, M.A., 1993. Early Permian granitic dykes of alkaline affinity in the Indian High Himalaya of Upper Lahul and SE Zanskar:

geochemical characterization and geotectonic implications. *Geological Society, London, Special Publications*, *74*(1), pp.251-264.

Srivastava, P. and Mitra, G., 1994. Thrust geometries and deep structure of the outer and lesser Himalaya, Kumaon and Garhwal (India): Implications for evolution of the Himalayan fold-and-thrust belt. *Tectonics*, *13*(1), pp.89-109.

St-Onge, M.R., Rayner, N., Palin, R.M., Searle, M.P. and Waters, D.J., 2013. Integrated pressure–temperature–time constraints for the Tso Morari dome (Northwest India): implications for the burial and exhumation path of UHP units in the western Himalaya. *Journal of Metamorphic Geology*, *31*(5), pp.469-504.

Steck, A., 2003. Geology of the NW Indian Himalaya. *Eclogae Geologicae Helvetiae*, *96*(2), pp.147-196.

StoLiczka, F., 1865. Geological sections across the Himalayan mountains, Mem. *GSIV pt*, *1*.

Tropper, P. and Hauzenberger, C., 2015. How well do pseudosection calculations reproduce simple experiments using natural rocks: an example from high-high-granulites of the Bohemian Massif P T P. *Austrian Journal of Earth Sciences*, *108*, p.1.

Warren, C.J., Grujic, D., Cottle, J.M. and Rogers, N.W., 2012. Constraining cooling histories: rutile and titanite chronology and diffusion modelling in NW Bhutan. *Journal of Metamorphic Geology*, *30*(2), pp.113-130.

Webb, A.A.G., Yin, A., Harrison, T.M., Célérier, J. and Burgess, W.P., 2007. The leading edge of the Greater Himalayan Crystalline complex revealed in the NW Indian Himalaya: Implications for the evolution of the Himalayan orogen. *Geology*, *35*(10), pp.955-958.

Webb, A.A.G., Schmitt, A.K., He, D. and Weigand, E.L., 2011. Structural and geochronological evidence for the leading edge of the Greater Himalayan Crystalline complex in the central Nepal Himalaya. *Earth and Planetary Science Letters*, *304*(3), pp.483-495.

Webb, A.A.G., 2013. Preliminary balanced palinspastic reconstruction of Cenozoic deformation across the Himachal Himalaya (northwestern India).*Geosphere*, *9*(3), pp.572-587.

Wendt, I. and Carl, C., 1991. The statistical distribution of the mean squared weighted deviation. *Chemical Geology: Isotope Geoscience Section*, *86*(4), pp.275-285.

White, L.T., and Lister, G.S., 2012, The collision of India with Asia: Journal of Geodynamics, v. 56–57, p. 7–17, doi:10.1016/j.jog.2011.06.006.

Wiedenbeck, M., Allé, P., Corfu, F., Griffin, W. L., Meier, M., Oberli, F., Von Quadt, A., Roddick, J. C., Spiegel, W., Three Natural Zircon Standards for U-Th-Pb, Lu-Hf, Trace Element and REE Analyses. Geostandards Newsletter 19, 1-23 (1995).

Wilke, F.D., O'Brien, P.J., Gerdes, A., Timmerman, M.J., Sudo, M. and Khan, M.A., 2010. The multistage exhumation history of the Kaghan Valley UHP series, NW Himalaya, Pakistan from U-Pb and 40Ar/39Ar ages.*European Journal of Mineralogy*, *22*(5), pp.703-719.

Wilke, F.D., O'Brien, P.J., Schmidt, A. and Ziemann, M.A., 2015. Subduction, peak and multi-stage exhumation metamorphism: Traces from one coesite-bearing eclogite, Tso Morari, western Himalaya. *Lithos*, *231*, pp.77-91.

Valdiya, K.S., 1980. The two intracrustal boundary thrusts of the Himalaya.*Tectonophysics*, *66*(4), pp.323-348.

van Hinsbergen, D.J.J., Steinberger, B., Doubrovine, P.V., and Gassmöller, R., 2011a, Acceleration and deceleration of India-Asia convergence since the Cretaceous: Roles of mantle plumes and continental collision: Journal of Geophysical Research, v. 116, B06101, doi:10.1029/2010JB008051.

van Hinsbergen, D.J.J., Kapp, P., Dupont-Nivet, G., Lippert, P.C., DeCelles, P.G., and Torsvik, T.H., 2011b, Restoration of Cenozoic deformation in Asia and the size of greater India: Tectonics, v. 30, TC5003, doi:10.1029/2011TC002908.

Van Hinsbergen, D.J., Lippert, P.C., Dupont-Nivet, G., McQuarrie, N., Doubrovine, P.V., Spakman, W. and Torsvik, T.H., 2012. Greater India Basin hypothesis and a two-stage Cenozoic collision between India and Asia. *Proceedings of the National Academy of Sciences*, *109*(20), pp.7659-7664.

Vannay, J.C. and Steck, A., 1995. Tectonic evolution of the high Himalaya in upper Lahul (NW Himalaya, India). *Tectonics*, *14*(2), pp.253-263.

Yin, A., Harrison, T.M., Ryerson, F.J., Wenji, C., Kidd, W.S.F. and Copeland, P., 1994. Tertiary structural evolution of the Gangdese thrust system, southeastern Tibet. *Journal of Geophysical Research: Solid Earth*,*99*(B9), pp.18175-18201.

Yin, A., and Harrison, T.M., 2000, Geologic evolution of the Himalaya-Tibetan orogeny: Annual Review of Earth and Planetary Sciences, v. 28, p. 211–280, doi:10.1146/annurev.earth.28.1.211

Yin, A., 2006. Cenozoic tectonic evolution of the Himalayan orogen as constrained by along-strike variation of structural geometry, exhumation history, and foreland sedimentation. *Earth-Science Reviews*, *76*(1), pp.1-131

Yin, A., Dubey, C.S., Kelty, T.K., Webb, A.A.G., Harrison, T.M., Chou, C.Y. and Célérier, J., 2010. Geologic correlation of the Himalayan orogen and Indian craton: Part 2. Structural geology, geochronology, and tectonic evolution of the Eastern Himalaya. *Geological Society of America Bulletin*, pp.B26461-1.

Zhang, R., Murphy, M.A., Lapen, T.J., Sanchez, V. and Heizler, M., 2011. Late Eocene crustal thickening followed by Early-Late Oligocene extension along the India-Asia suture zone: Evidence for cyclicity in the Himalayan orogen. *Geosphere*, *7*(5), pp.1249-1268

Zhu, B., Kidd, W.S.F., Rowley, D.B., Currie, B.S., and Shafique, N., 2005, Age of initiation of the India-Asia collision in the east-central Himalaya: Journal of Geology, v. 113, p. 265–285, doi:10.1086/428805.

APPENDIX A: CHAPTER 2 SUPPLEMENTAL TABLES & FIGURES

Supplementary Table A1. Laser ablation multi-collector inductively coupled plasma mass spectrometry analyses of U-Th-Pb isotopes in zircon.

Sample		Elements (ppm)			Isotopic Ratios					Age			
		U	Th	Pb	$^{232}Th/^{238}U$	$^{238}U/^{206}Pb$	±2σ error	$^{207}Pb/^{206}Pb$	±2σ error	$^{206}Pb/^{238}U$ [a]	±2σ error	$^{207}Pb/^{235}U$	±2σ error
CM71710-4	1	18	1.3	2.7	0.074	68.0	5.74	0.445	0.046	47.0	6.4	650	40.0
	2	30	0.5	0.4	0.017	147	10.5	0.145	0.016	38.4	2.2	128	14.0
	3	9	n/a	1.0	n/a	80.0	13.4	0.380	0.121	46.6	14.4	510	140
	4	88	0.1	0.6	0.001	129	7.64	0.084	0.008	47.6	1.6	87.1	6.2
	5	70	1.4	0.4	0.020	123	7.67	0.072	0.009	50.4	2.0	79.9	8.7
	6	22	3.4	4.4	0.156	49.0	7.84	0.572	0.050	44.3	10.8	960	130
	7	20	1.1	3.6	0.056	61.4	4.69	0.444	0.037	52.2	5.8	714	48.0
	8	51	n/a	4.7	n/a	90.3	6.89	0.358	0.034	43.3	4.0	447	34.0
	9	26	2.8	2.3	0.110	89.4	6.21	0.398	0.063	40.1	6.1	478	40.0
	10	11	1.8	2.5	0.164	55.2	7.54	0.550	0.063	42.5	10.8	856	88.0
	11	21	2.6	3.3	0.126	65.4	6.08	0.457	0.041	47.5	6.4	685	68.0
	12	21	1.8	3.2	0.087	74.6	8.14	0.483	0.062	38.8	7.7	628	72.0
	13	17	2.7	2.0	0.155	82.6	10.4	0.443	0.044	38.9	6.3	540	68.0
	14	11	n/a	2.1	n/a	55.9	7.12	0.471	0.040	53.5	8.6	753	83.0
	15	26	2.3	3.8	0.088	68.4	4.48	0.446	0.032	46.7	4.4	664	27.0
	16	31	0.0	3.5	0.000	79.6	5.51	0.386	0.028	46.2	3.6	524	21.0
	17	24	0.4	0.4	0.016	127	7.89	0.134	0.014	45.0	1.9	136	12.0
	18	23	0.8	5.3	0.035	50.3	4.13	0.513	0.044	52.7	8.0	894	47.0
	19	80	5.1	9.8	0.064	109	6.62	0.215	0.023	46.6	2.3	236	24.0
	20	57	n/a	7.1	n/a	105	6.60	0.245	0.020	45.8	2.3	294	22.0
	21	94	8.9	19.8	0.095	107	7.17	0.339	0.033	38.0	3.0	372	38.0
	22	78	14.4	21.7	0.184	86.3	7.06	0.368	0.040	44.3	4.7	465	54.0
	23	47	1.0	7.0	0.021	87.2	8.50	0.283	0.028	51.7	5.0	378	45.0
	24	82	5.8	30.4	0.070	74.6	7.65	0.387	0.036	49.2	5.9	565	71.0
	25	35	n/a	0.5	n/a	119	9.16	0.137	0.028	47.8	3.4	140	29.0
	26	29	2.0	6.0	0.069	83.3	8.70	0.318	0.036	50.7	5.8	426	49.0
	27	63	18.4	14.0	0.293	89.3	9.84	0.385	0.041	41.3	5.5	488	69.0
	28	45	4.9	15.1	0.109	74.5	5.97	0.438	0.032	43.7	4.5	602	39.0
	29	54	6.2	8.2	0.114	94.1	7.43	0.264	0.030	49.6	4.0	330	42.0
	30	29	0.2	2.9	0.007	95.1	6.62	0.252	0.029	50.1	3.5	322	34.0
	31	62	8.0	9.2	0.129	99.5	8.13	0.272	0.031	46.2	3.9	325	43.0
	32	48	4.7	11.3	0.099	87.1	6.03	0.370	0.030	43.7	3.5	480	39.0
	33	144	2.3	4.1	0.016	124	7.23	0.123	0.013	46.7	1.6	131	15.0
	34	80	1.4	15.7	0.018	92.1	6.43	0.347	0.026	43.4	3.1	431	33.0
	35	27	1.1	19.6	0.041	45.2	5.22	0.606	0.048	41.9	9.8	1084	73.0
	36	76	26.3	7.7	0.346	104	6.54	0.223	0.020	47.8	2.4	265	21.0
	37	122	4.2	5.3	0.034	113	6.55	0.142	0.011	50.1	1.7	160	11.0
	38	115	1.4	1.2	0.012	134	7.52	0.096	0.008	45.0	1.2	94.5	6.4
	39	27	3.4	2.4	0.125	97.0	8.72	0.326	0.044	42.9	4.9	353	44.0
	40	34	1.1	7.2	0.032	82.6	7.24	0.390	0.031	44.1	4.4	506	39.0
	41	32	0.9	0.4	0.028	119	9.31	0.197	0.033	43.6	3.4	206	34.0
	42	49	3.8	15.7	0.078	69.9	5.69	0.379	0.031	53.4	5.0	566	53.0
	43	170	0.6	2.9	0.004	147	9.79	0.118	0.021	39.8	2.1	105	19.0
	44	73	2.2	14.6	0.030	91.8	7.54	0.342	0.036	43.9	4.3	400	42.0
	45	89	3.4	8.4	0.038	109.1	11.7	0.278	0.040	41.8	5.0	330	60.0
	46	40	n/a	0.5	n/a	124	8.32	0.163	0.021	44.2	2.4	166	19.0
	47	57	n/a	53.6	n/a	44.8	3.29	0.579	0.036	47.1	7.3	1036	42.0
	48	49	3.4	12.6	0.069	96.0	7.04	0.385	0.043	38.4	4.2	453	47.0
	49	24	n/a	11.7	n/a	66.7	10.3	0.465	0.046	45.6	8.8	684	91.0
	50	91	n/a	33.4	n/a	78.2	5.84	0.403	0.028	45.3	3.9	535	37.0
	51	279	5.7	8.3	0.020	135	7.17	0.105	0.009	44.0	0.9	104	7.1
	52	75	3.8	15.6	0.050	94.1	6.05	0.287	0.019	47.6	2.6	357	20.0
	53	116	1.9	28.6	0.016	91.5	5.39	0.317	0.020	46.3	2.4	400	21.0
	54	46	n/a	7.0	n/a	96.1	6.85	0.294	0.029	46.0	3.4	367	36.0
	55	36	2.1	10.1	0.059	85.9	5.30	0.408	0.029	40.7	3.2	516	23.0
	56	41	0.6	4.3	0.015	109	7.19	0.270	0.024	42.2	2.6	294	22.0
DD71710-2b	57	79	6.5	2.9	0.082	117	8.05	0.213	0.019	43.0	2.4	226	18.0
	58	62	9.4	2.7	0.152	117	8.91	0.219	0.023	42.7	2.9	233	25.0
	59	21	0.0	5.0	0.000	49.7	3.32	0.536	0.039	47.5	7.1	912	41.0
	60	22	0.5	8.5	0.023	38.2	2.59	0.637	0.036	39.9	8.4	1196	29.0
	61	71	5.3	9.5	0.075	74.3	4.70	0.439	0.026	42.6	3.4	596	23.0
	62	21	1.2	6.6	0.058	45.9	3.26	0.606	0.039	38.8	7.5	1066	45.0
	63	33	0.5	2.1	0.015	95.0	6.19	0.279	0.020	47.3	2.6	345	21.0
	64	29	7.6	1.5	0.259	112	6.83	0.252	0.020	42.1	2.1	272	16.0

Supplementary Table 1 *(continued)*

65	25	1.5	1.6	0.060	97.8	5.62	0.282	0.021	45.7	2.3	344	17.0
66	109	4.9	1.7	0.045	140	8.24	0.134	0.010	40.7	1.4	126	7.0
67	59	1.8	1.3	0.030	126	8.50	0.156	0.020	43.8	2.4	164	14.0
68	38	1.3	1.5	0.034	114	10.1	0.237	0.044	42.3	4.4	239	28.0
69	182	7.9	0.5	0.043	152	10.1	0.058	0.006	41.7	1.9	51.7	6.1
70	130	6.3	0.2	0.049	146	8.55	0.049	0.006	43.9	1.4	47.2	5.4
71	22	n/a	3.2	n/a	65.4	6.44	0.440	0.040	48.3	6.6	666	60.0
72	32	0.5	2.6	0.015	95.0	6.55	0.341	0.029	41.9	3.2	411	32.0
73	30	1.1	4.1	0.036	71.9	5.25	0.477	0.035	39.6	4.6	642	40.0
74	30	0.5	2.4	0.017	95.6	6.87	0.349	0.028	40.9	3.3	405	21.0
75	51	3.1	3.3	0.060	98.6	5.88	0.302	0.021	43.6	2.3	348	15.0
76	37	n/a	4.3	n/a	76.5	6.42	0.414	0.041	44.1	5.4	570	45.0
77	25	0.8	4.9	0.032	57.8	4.42	0.498	0.044	46.3	6.9	791	62.0
78	15	2.9	5.6	0.200	37.9	3.09	0.613	0.040	45.4	9.6	1203	63.0
79	44	2.1	2.9	0.048	89.5	8.42	0.299	0.030	48.3	4.8	382	38.0
80	17	n/a	1.4	n/a	87.3	6.49	0.337	0.034	46.0	4.1	423	33.0
81	23	0.7	1.0	0.030	114	12.0	0.229	0.022	43.0	4.3	239	20.0
82	13	1.4	5.1	0.112	35.6	4.78	0.670	0.064	35.0	15.7	1280	120
83	8	2.7	5.4	0.348	22.8	2.37	0.712	0.056	39.4	21.2	1715	79.0
84	15	0.4	3.0	0.028	52.4	6.57	0.544	0.049	43.8	9.4	881	94.0
85	39	0.4	2.6	0.010	103	7.19	0.311	0.030	41.0	3.2	354	30.0
86	67	4.2	4.3	0.063	107	7.12	0.319	0.023	38.9	2.5	349	23.0
87	29	2.7	3.8	0.094	75.2	6.79	0.440	0.035	42.0	5.0	587	28.0
88	34	4.2	2.0	0.124	95.0	6.19	0.275	0.020	47.7	2.7	336	19.0
89	61	3.4	0.5	0.056	137	8.03	0.098	0.009	43.7	1.4	92.1	6.3
90	32	1.8	3.8	0.056	76.6	5.49	0.440	0.030	41.2	3.9	589	30.0
91	24	6.8	4.3	0.285	63.7	7.23	0.492	0.039	42.8	6.8	732	72.0
92	9	0.6	4.3	0.071	25.7	5.76	0.714	0.089	34.3	29.8	1550	170
93	16	1.4	3.7	0.088	55.6	4.63	0.572	0.070	37.1	10.9	882	71.0
94	11	0.3	4.3	0.028	33.1	4.59	0.651	0.045	42.4	12.9	1320	100
95	41	0.5	0.3	0.012	127	8.00	0.090	0.011	47.7	1.9	96.0	11.0
96	17	1.7	0.2	0.098	136	9.25	0.132	0.021	42.1	2.3	126	20.0
97	78	7.3	5.2	0.094	121	7.46	0.127	0.014	47.7	2.0	137	15.0
98	73	3.6	26.8	0.050	74.6	6.16	0.401	0.029	46.7	4.5	541	36.0
99	58	6.5	31.4	0.112	62.2	3.83	0.467	0.028	47.2	4.2	708	26.0
100	46	9.5	17.2	0.207	75.5	4.66	0.400	0.024	46.2	3.2	545	21.0
101	36	0.7	4.5	0.020	96.0	7.74	0.225	0.023	51.5	3.8	287	27.0
102	36	6.6	24.8	0.185	49.3	4.60	0.554	0.036	44.9	7.2	936	68.0
103	119	3.1	18.7	0.026	103.8	7.18	0.271	0.022	43.9	2.7	311	27.0
104	47	n/a	19.7	n/a	71.2	4.85	0.464	0.035	41.5	4.6	628	35.0
105	34	n/a	8.1	n/a	85.3	5.99	0.331	0.027	47.7	3.5	414	27.0
106	103	5.1	2.5	0.049	142	8.34	0.101	0.013	42.2	1.5	98.0	13.0
107	54	17.2	16.2	0.321	84.6	5.49	0.326	0.023	48.5	3.1	425	24.0
108	65	4.1	9.7	0.063	102	8.71	0.302	0.040	42.2	4.4	342	49.0
109	52	0.6	39.7	0.012	50.8	3.62	0.522	0.031	48.8	5.8	898	36.0
110	23	n/a	14.2	n/a	63.3	6.09	0.473	0.043	45.6	6.9	740	64.0
111	125	18.4	76.3	0.148	59.1	4.44	0.482	0.031	47.5	5.2	764	48.0
112	114	10.2	21.8	0.089	101	7.50	0.281	0.023	44.5	3.1	335	31.0
113	465	22.4	23.0	0.048	144	8.61	0.137	0.015	39.5	1.6	123	11.0
114	145	8.7	33.2	0.060	88.5	9.00	0.310	0.033	47.9	5.3	400	57.0
115	101	10.3	12.7	0.102	115	6.95	0.219	0.018	43.3	1.9	239	16.0
116	34	2.6	27.7	0.077	51.8	3.93	0.552	0.036	43.0	6.4	917	44.0
117	57	2.8	60.1	0.049	39.2	5.15	0.628	0.044	40.7	10.8	1180	110
118	109	6.5	12.7	0.060	108	7.58	0.232	0.028	45.0	3.1	261	35.0
119	78	2.6	16.6	0.033	88.5	11.1	0.362	0.053	43.0	7.0	463	87.0
120	129	5.7	24.1	0.044	97.2	5.99	0.279	0.020	46.3	2.4	342	22.0
121	62	n/a	57.0	n/a	41.3	6.00	0.620	0.057	40.2	12.9	1110	150
122	70	n/a	28.9	n/a	70.1	4.71	0.399	0.027	49.9	4.0	585	31.0
123	49	3.7	15.6	0.075	79.7	5.60	0.362	0.028	47.8	3.8	478	33.0
124	118	7.1	15.7	0.060	99.1	8.48	0.263	0.031	46.7	4.2	324	45.0
125	35	5.4	18.7	0.156	62.1	5.26	0.482	0.035	45.2	5.7	723	54.0
126	104	24.9	28.7	0.240	94.1	6.34	0.336	0.030	42.8	3.3	410	32.0
127	23	2.8	0.6	0.122	126	13.8	0.193	0.041	41.2	4.8	166	30.0
128	54	6.0	20.7	0.110	72.2	5.55	0.404	0.028	47.9	4.4	578	40.0
129	72	1.2	75.2	0.017	42.0	3.52	0.596	0.037	44.3	8.2	1089	50.0
130	55	6.1	20.7	0.112	74.5	4.92	0.394	0.026	47.5	3.6	550	28.0
131	71	1.1	35.6	0.016	66.8	5.02	0.471	0.033	43.4	4.9	672	45.0
132	77	4.6	16.8	0.060	103	6.54	0.326	0.025	39.9	2.6	366	20.0
133	155	8.5	10.7	0.055	117	8.17	0.142	0.018	48.3	2.7	160	20.0
134	40	0.1	38.9	0.002	44.2	4.16	0.579	0.040	45.3	8.5	1040	61.0
135	101	15.0	6.3	0.149	129	7.78	0.163	0.019	42.3	1.9	160	16.0
136	37	0.9	24.9	0.025	55.6	4.39	0.548	0.036	40.7	6.2	852	53.0

Note:Both samples were analyzed 09/01/2011 and 02/17/2012, for which the error in standard deviation is (2σ). Common Pb is corrected by projecting a line through all analyses to $^{207}Pb/^{206}Pb$ and $^{238}U/^{206}Pb$ on the Tera-Wasserburg Concordia diagram (Figure 2). [a] Age corrected for ^{207} Pb

Supplementary Table A2

Laser ablation single-collector inductively coupled plasma mass spectrometry analyses of rare earth elements in zircon.

Sample	Analysis	La	Ce	Pr	Nd	Sm	Eu	Gd	Tb	Dy	Ho	Er	Tm	Yb	Lu
CM71710-4	2	4.000	0.30	0.00	0.00	2	10	12.0	21.0	14.0	21.0	18.0	14.0	20.0	15.0
	4	6.000	1.40	0.00	0.00	26.0	56	84.0	54.0	37.0	30.0	34	35	37	39
	7	9.000	0.70	4.50	0.00	9.0	15	38.0	21.0	16.0	15.0	18	13	16	21
	9	11.000	0.50	0.00	0.00	9.0	15	15.0	18.0	12.0	12.0	14.0	14.0	18.0	26.0
	13	15.000	0.30	0.00	1.10	5.0	7	14.0	11.0	11.0	12.0	14	14	29	31
	17	19.000	1.00	0.00	1.10	11.0	20	28.0	22.0	19.0	15.0	12.0	19.0	20.0	28
	18	20.000	0.20	0.00	0.00	3.0	3	10.0	6.0	9.0	9.0	8.0	11.0	12.0	28.0
	19	0.173	5.87	0.77	1.72	22	36	94.2	109.7	146.2	173.4	275	335	551	776
	20	n/a	0.43	0.21	0.80	12	25	48.4	41.8	38.4	36.2	43.2	38.1	58.6	65.0
	21	0.007	2.50	0.44	0.37	10	46	68.5	36.7	32.4	24.9	42.8	53.6	98.5	159
	22	0.030	1.11	0.20	1.30	6.5	14	51.1	40.5	58.6	90.2	240	352	537	714
	23	0.147	5.81	1.42	2.97	5.5	13	20.1	19.6	23.3	21.2	29.0	26.8	48.0	54.9
	24	0.214	7.35	2.85	7.39	42	42	62.2	50.3	47.4	41.8	47.7	69.2	75.4	95.8
	25	0.029	0.58	0.57	n/a	8.6	23	56.7	52.7	86.2	91.2	121	134	154	156
	26	0.054	0.58	0.45	0.35	6.4	20	33.6	40.7	49.2	59.4	79.2	76.8	83.6	101
	27	0.050	0.95	0.63	0.35	7.0	17	20.8	33.2	27.9	26.8	37.4	41.4	51.5	76.2
	28	0.041	0.69	0.19	0.46	10	18	27.3	30.4	54.1	82.6	111	130	211	247
	29	0.009	3.39	0.41	1.04	17	22	84.4	135	237	374	710	1226	2394	2926
	30	0.050	0.24	0.17	0.19	1.6	6.2	14.3	15.1	16.4	14.0	15.4	15.8	16.6	26.5
	31	0.010	1.00	0.20	0.81	4.7	16	49.2	44.2	64.3	117.6	242	384	731	1099
	32	0.014	0.61	0.22	1.01	9.4	26	37.6	41.6	34.6	41.5	47.9	70.8	65.6	78.3
	33	0.038	1.40	n/a	0.61	13	42	75.5	66.9	64.8	68.1	70.7	67.0	80.4	61.9
	34	n/a	1.49	0.41	0.74	4.1	24	42.9	27.3	34.7	29.8	34.5	33.8	38.0	34.5
	35	0.031	0.35	0.38	0.42	4.9	12	20.0	22.3	24.4	31.4	33.4	34.7	38.9	49.1
	36	0.059	0.82	0.35	0.84	4.1	13	22.1	18.4	11.6	19.2	30.9	46.9	81.9	130
	37	0.003	0.60	0.36	0.62	6.9	16	31.1	47.9	70.1	116	229	300	379	428
	38	0.043	1.40	0.77	0.90	19	57	82.3	75.7	62.0	64.3	97.7	134	173	171
	39	0.021	1.61	0.35	0.73	10	24	40.5	43.7	37.3	37.3	49.8	42.6	48.3	50.3
	40	0.039	0.58	0.19	0.56	6.4	27	51.6	48.6	60.7	69.8	92.2	92.0	108	117
	41	0.061	2.12	0.32	n/a	4.1	14	25.3	28.9	39.8	49.8	60.1	58.6	61.9	74.7
	42	0.025	0.33	0.12	0.39	4.5	21	46.9	52.5	37.6	34.1	28.4	37.0	30.3	37.3
	43	0.031	0.22	0.14	0.47	4.1	12	20.1	19.5	18.4	17.7	24.1	24.8	28.3	36.2
	44	n/a	1.43	0.65	0.90	13	53	92.9	68.6	54.1	45.0	54.4	50.2	47.3	51.9
	45	0.049	0.43	0.17	0.69	5.7	16	34.6	27.4	29.3	32.1	88.6	176	304	537
	46	0.003	0.98	0.27	1.04	16	35	63.6	59.2	43.8	45.6	61.1	76.6	172	240
	47	n/a	0.75	0.08	0.60	6.9	24	43.3	54.2	70.8	89.3	107	110	158	173
	48	0.003	1.00	0.18	0.50	5.0	20	42.0	40.0	56.2	65.5	82.9	67.8	68.1	67.8
	49	n/a	0.39	0.37	0.29	4.8	13	20.0	24.7	20.6	13.3	25.4	22.6	24.2	30.9
	50	0.030	0.34	0.12	0.01	.6	7.9	15.3	8.23	10.0	10.5	15.8	13.8	21.9	33.6
	51	n/a	1.02	0.14	0.54	11	35	49.7	43.3	43.9	44.3	50.4	52.0	59.2	66.7
	52	0.045	2.20	n/a	0.73	21	57	108	77.0	52.5	35.3	34.2	34.4	38.0	44.0
	53	0.081	0.71	0.09	0.17	10	34	55.9	50.5	42.4	35.9	37.7	43.8	44.3	63.6
	54	0.020	0.64	0.13	0.18	13	42	56.9	49.8	35.4	33.3	38.9	36.2	44.0	49.6
	55	n/a	0.75	0.17	0.46	7.5	18	29.8	27.9	26.0	32.0	30.8	26.0	39.8	42.1
	56	0.014	0.45	0.10	0.98	4.4	11	15.9	22.0	20.2	21.7	25.0	24.1	36.2	43.2

Supplementary Figure A1. Figure is a probability density function modified from Leech et al., 2005. The ages are reported with their respective MSWD values. The interpreted UHP age of 53.3 ± 0.7 Ma has an MSWD of 0.20 which suggests either over-estimation of analytical uncertainties or under-sampling (Wendt and Carl, 1991).

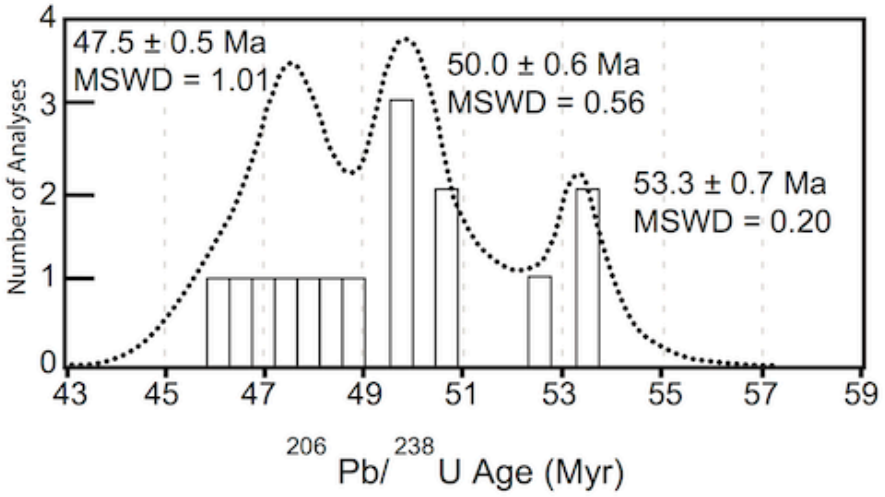

Supplementary Figure A2 A. Representative image of CM71710-4 thin section. Boxes represent areas of photomicrographs in Fig A2 D-AA, the numbers correspond to the name of the zircon dated within each specified subregion (see Figure A2 D-AA and Table A1).

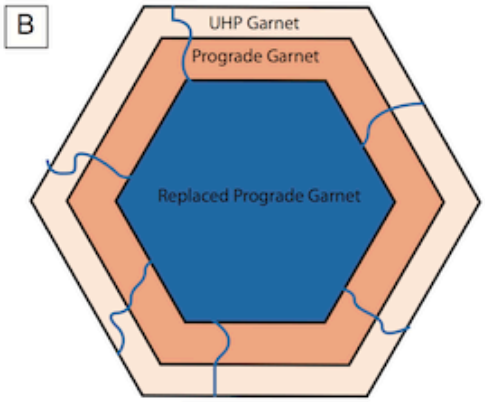

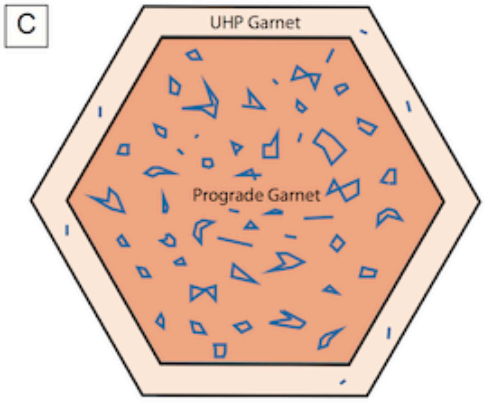

Supplementary Figure A2 continued. Cartoons illustrating garnet textures seen in Tso Morari eclogites (including the dated samples), following detailed descriptions by O'Brien (2006) and Konrad-Schmolke et al. (2008). B) Atoll garnet structure. Here there are three major zones: a rim of Mg-rich UHP garnet (in which previous workers have identified coesite), a core of Ca-rich prograde garnet, and a central zone in which Ca-rich prograde garnet has been replaced by HP-UHP minerals. C) Garnet with Ca-rich, inclusion-rich, idioblastic core (prograde) and Mg-rich, inclusion-poor rim (UHP).

Supplementary Figure A2 continued (Zircon 3)

Zircon included in UHP garnet

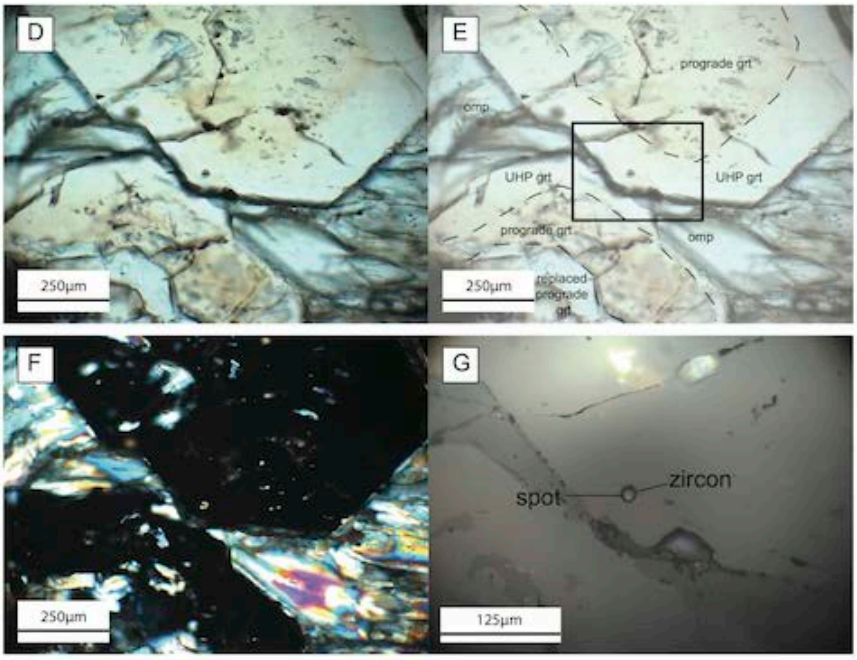

Figure A2 continued (Zircon 3): D is a TL image of the sample; E is an annotated version of D; F is XPL image; G is a reflected light image. grt = garnet; omp= omphacite; Spot signals where zircon was shot.

Supplementary Figure A2 continued (Spot 26)

Zircon included in UHP garnet

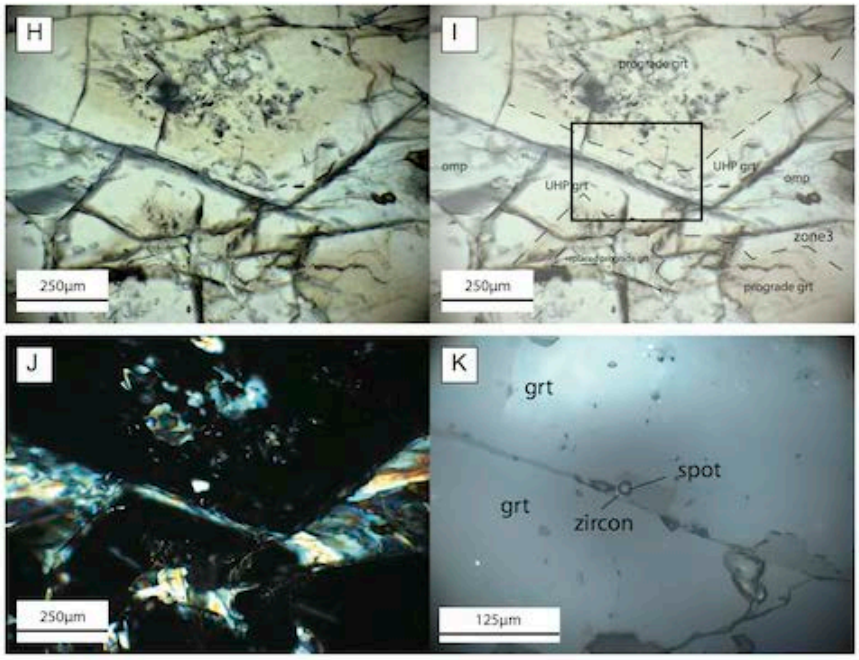

Figure A2 continued (Spot 26): H is a TL image of the sample; I is an annotated version of H.; J is XPL image; K is a reflected light image; grt = garnet; omp= omphacite; Spot signals where zircon was shot.

Supplementary Figure A2 continued (Spot 21)

Zircon inlcluded in omphacite

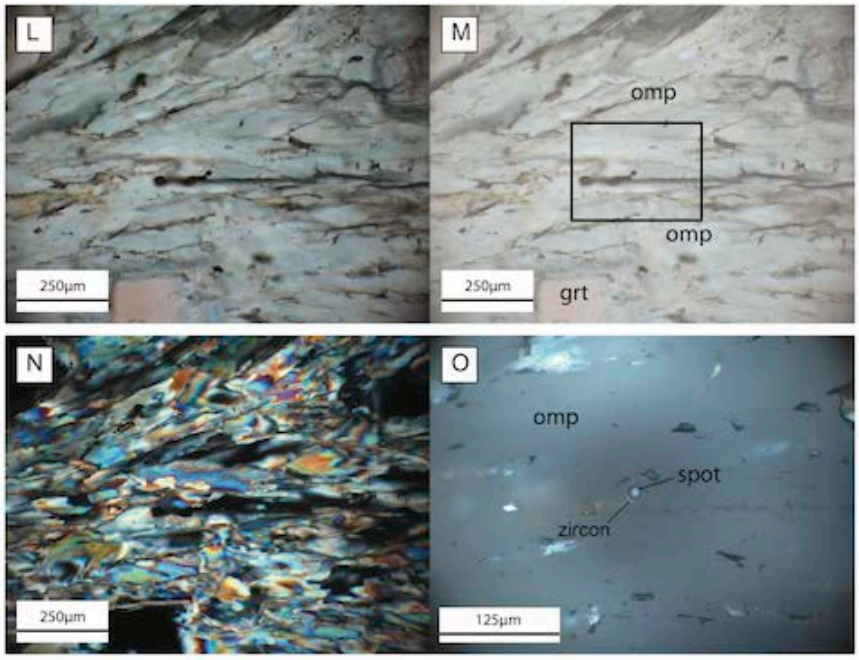

Figure A2 continued (Spot 21): L is a TL image of the sample; M is an annotated version of L; N is XPL image; M is a reflected light image; grt = garnet; omp= omphacite; rut = rutile. Spot signals where zircon was shot.

Supplementary Figure A2 continued (Spot 27)

Zircon included in omphacite

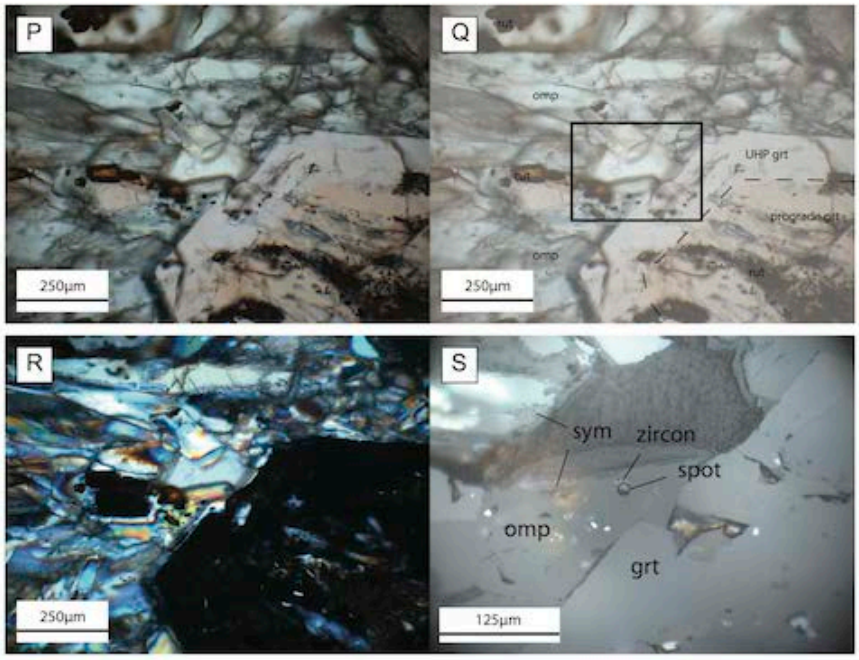

Figure A2 continued (Spot 27): P is a TL image of the sample; Q is an annotated version of P; R is XPL image; S is a reflected light image; grt = garnet; omp= omphacite; sym = symplectite rut = rutile. Spot signals where zircon was shot.

Supplementary Figure A2 continued (Zircon 8)

Zircon in matrix

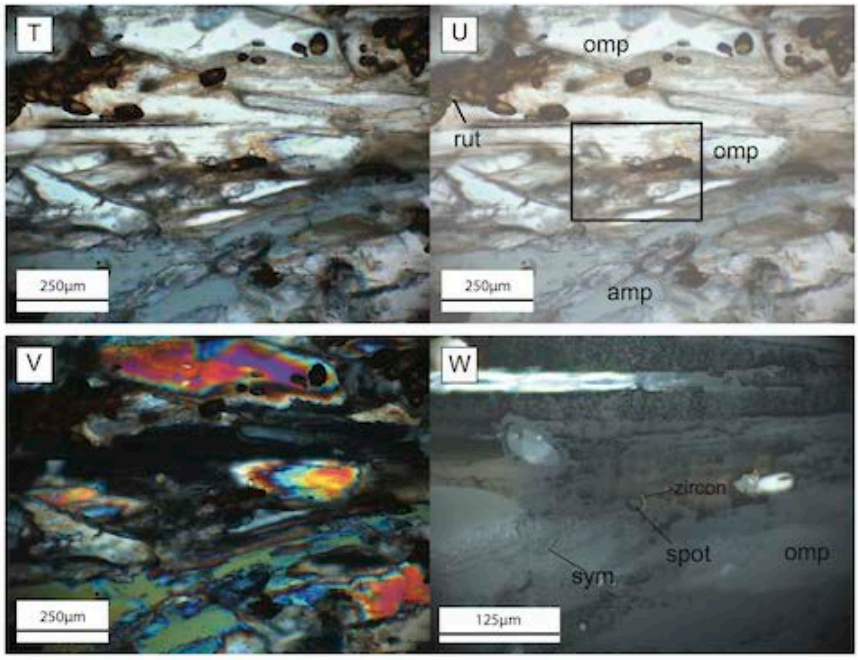

Figure A2 continued (Spot 8): T is a TL image of the sample; U is an annotated version of T; V is XPL image; W is a reflected light image. amp = amphibole; omp= omphacite; sym = symplectite rut = rutile. Spot signals where zircon was shot.

Supplementary Figure A2 continued (Spot 24)

Zircon in the matrix

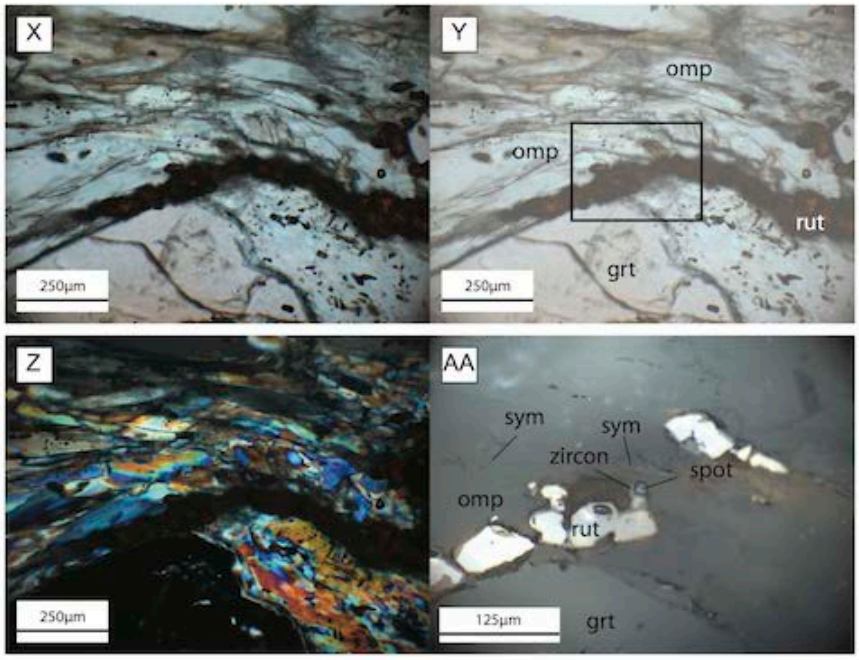

Figure A2 continued (Spot 24): X is a TL image of the sample; Y is an annotated version of X; Z is XPL image; AA is a reflected light image; grt = garnet; omp= omphacite; sym = symplectite; rut = rutile. Spot signals where zircon was shot.

Supplementary Figure A3 Cathodoluminescence zircon images from CM71710-4 and DD71710-2b eclogites. Images show zoning characteristics of analysed and representative zircons. Cathodluminescense of zircon can reveal the internal structure of the mineral and distinguish between homegenous and heterogenous crystallization. The majority of the images exhibit irregular patchy zoning similar to "auroral lights" zoning (Corfu et al., 2003) indicative of a high pressure event. Images A-B of A3 are of analyzed spots which generally show oscillatory zoning with possibility of recrystallization indicative of brighter illumination regions in the grain. Images with defined cores can be interpreted to have older and younger generations of growth.

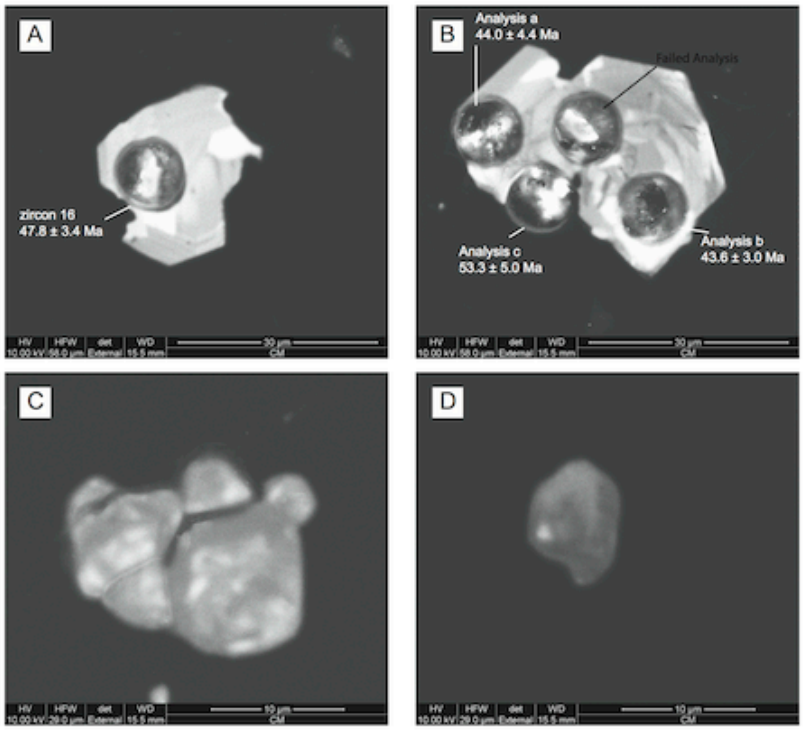

Supplementary Figure A3 - Cathodoluminescense Images in CM71710-4. A) CL image of zircon shot in analysis 16 = 47.8 ± 3.4 Ma . Image shows possible recrystallization in brighter areas outside of spot diameter. Zoning is generally oscillatory. B) CL image of zircon shot in analyses 31-33. Fourth image analysis in the center of the image was not within detection limits of the rest of the analyses. "Analysis a" has a 207-Pb-corrected age of 44.0 ± 4.4 Ma; "Analysis b" = 43.6 ± 3.0 Ma; "Analysis c" 53.3 ± 5.0 Ma. Zoning appears to be heterogeneously patchy. C) CL image of zircon cluster included in UHP garnet rim. Zoning is irregular and patchy . D) CL image of zircon included in UHP garnet rim. Zoning is irregular and patchy with weak illuminescence.

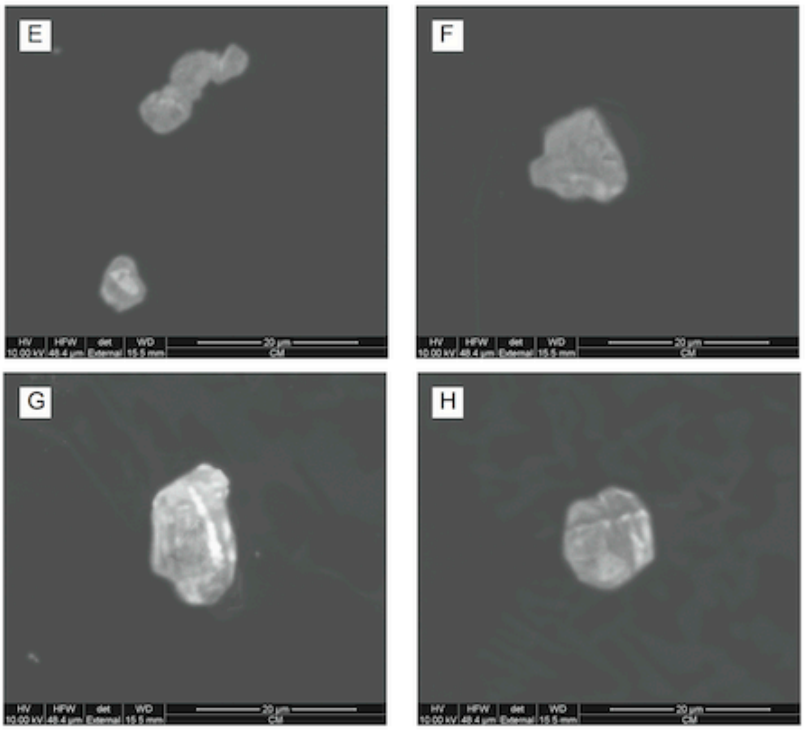

Supplementary Figure A3 continued - Cathodoluminescense Images in DD71710-2b. E) CL image of zircon cluster included in UHP garnet. Zoning is irregular patchy. Lone zircon appears to have a distinct core. F) CL image of zircon included in UHP garnet. Zoning is irregularly patchy. G) CL image of zircon in matrix near symplectite. Zoning is irregularly patchy with possible metamictization. H) CL image of zircon in the matrix near symplectite. Zoning is irregularly patchy with possible metamictization.

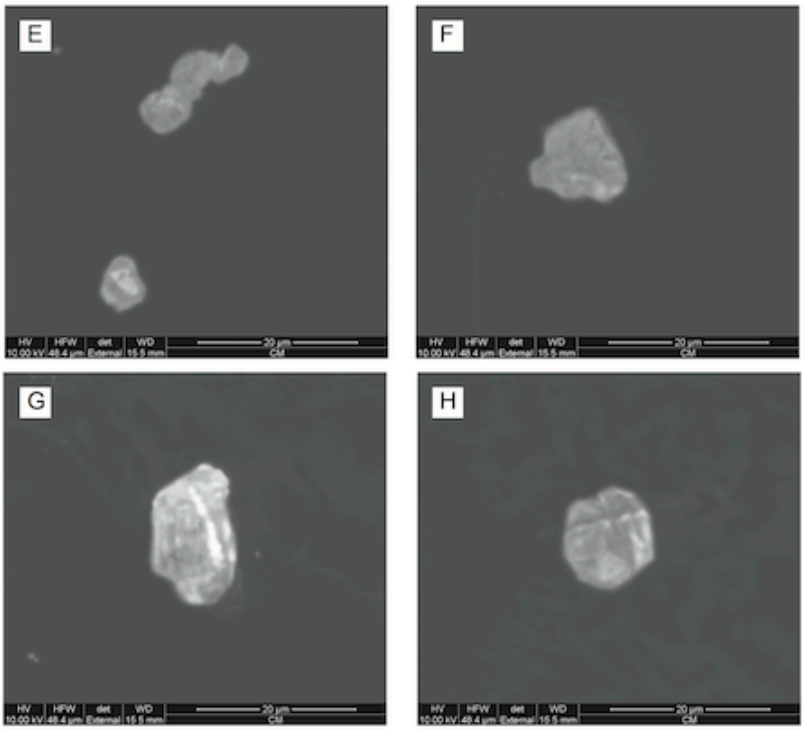

Supplementary Figure A3 continued - Cathodoluminescense Images in DD71710-2b. E) CL image of zircon cluster included in UHP garnet. Zoning is irregular patchy. Lone zircon appears to have a distinct core. F) CL image of zircon included in UHP garnet. Zoning is irregularly patchy. G) CL image of zircon in matrix near symplectite. Zoning is irregularly patchy with possible metamictization. H) CL image of zircon in the matrix near symplectite. Zoning is irregularly patchy with possible metamictization.

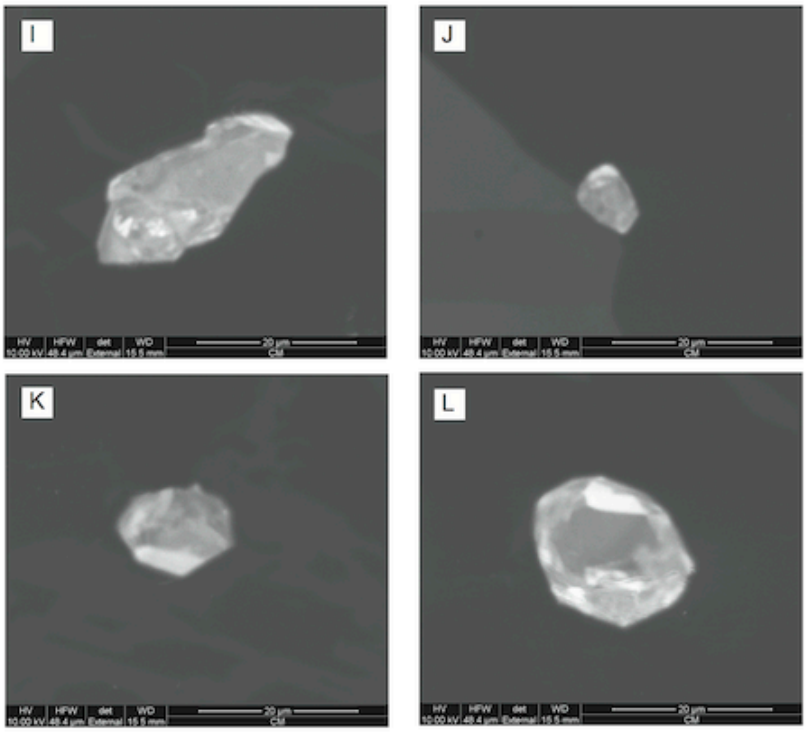

Supplementary Figure A3 continued - Cathodoluminescense Images in DD71710-2b. I) CL image of zircon in the matrix with irregular and patchy zoning. J) CL of a zircon in the matrix near garnet/ompachite grain boundary with irregular patchy zoning. K) CL of zircon near a rutile grain in matrix. Zoning is generally patchy besides the lower end of the grain which exhibits higher contrast. L) CL of zircon in the matrix. The grain exhibits a core and a possible zone of recrystallization, indicative of the higher contrast region at the top of the grain.

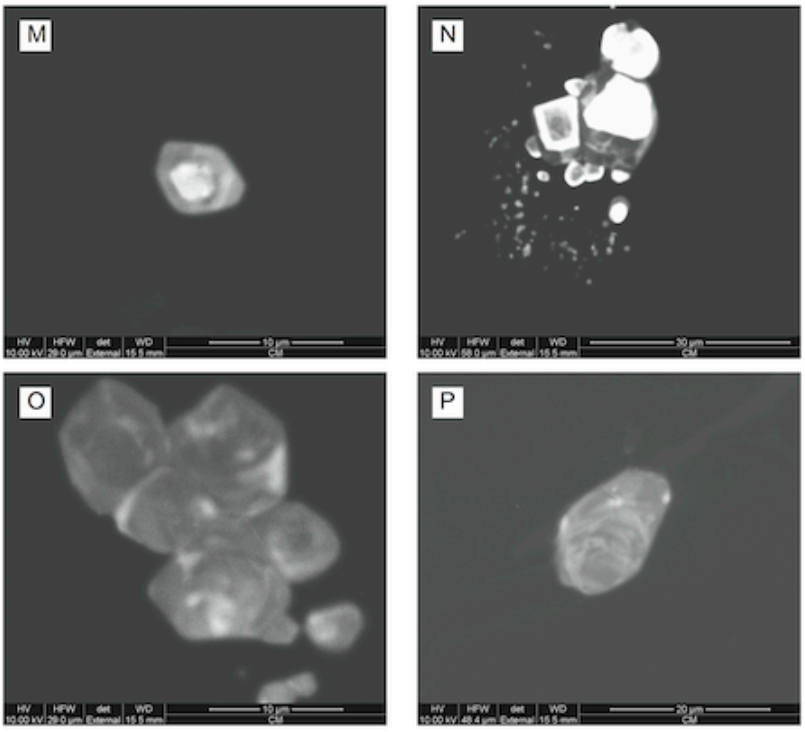

Supplementary Figure A3 Cathodoluminescense Images in CM71710-4 (M-O) and DD71710-2b (P). M) CL image of zircon grain included in UHP garnet. Zoning appears heterogeneous with a distinct core and metamorphic rim. N) CL image of zircon cluster in the matrix with defined areas of metamorphic rim growth indicative of the darker contrast. O) CL image of zircon cluster with irregular patchy zoning near garnet grain boundary. P) CL image of zircon included in omphacite with indistinct patchy zoning.

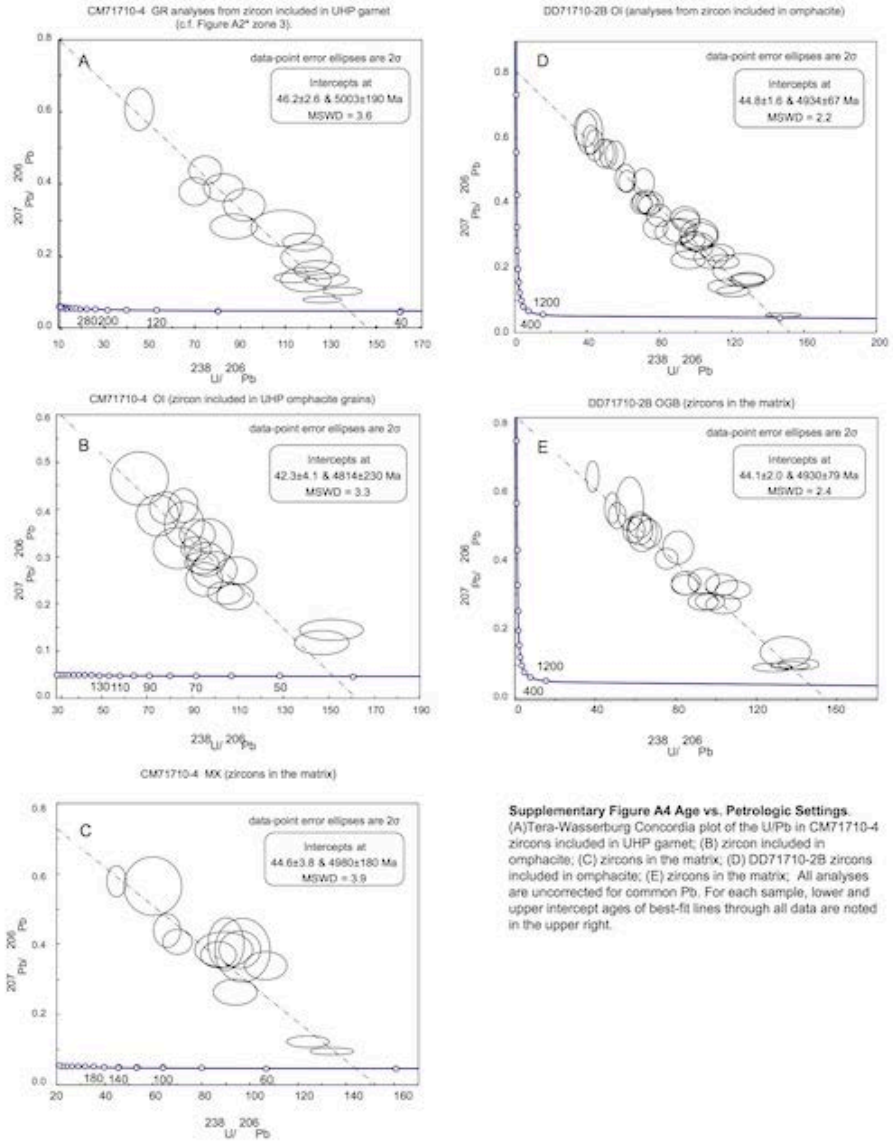

Supplementary Figure A4 Age vs. Petrologic Settings. (A)Tera-Wasserburg Concordia plot of the U/Pb in CM71710-4 zircons included in UHP garnet; (B) zircon included in omphacite; (C) zircons in the matrix; (D) DD71710-2B zircons included in omphacite; (E) zircons in the matrix; All analyses are uncorrected for common Pb. For each sample, lower and upper intercept ages of best-fit lines through all data are noted in the upper right.

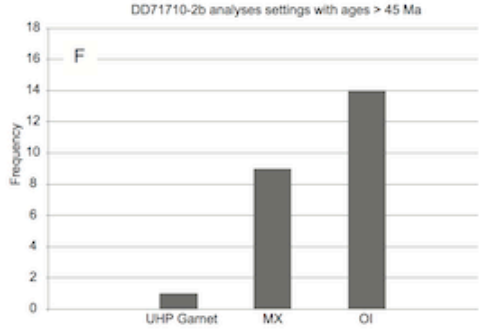

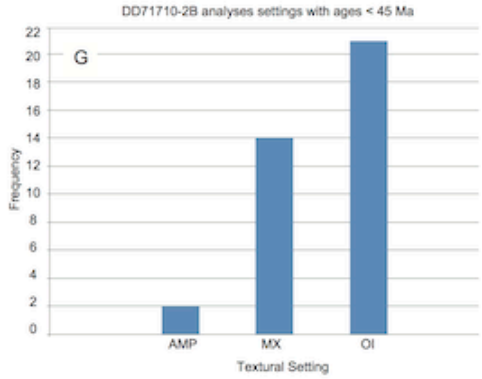

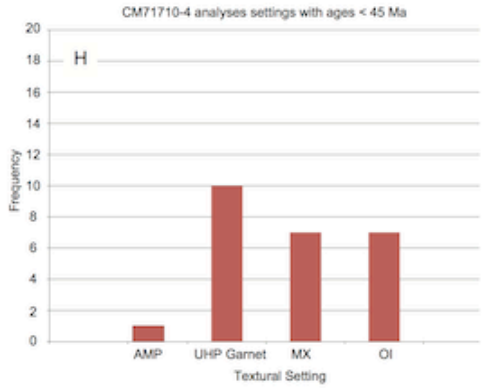

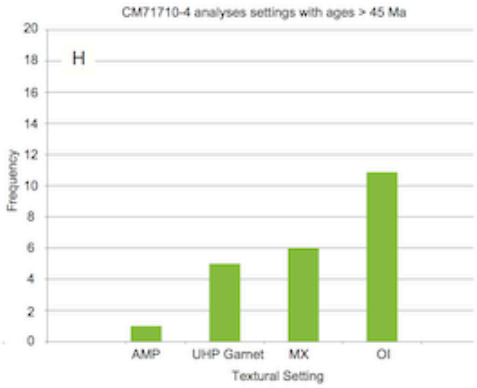

Supplementary Figure A4 continued. Age vs. Petrologic Setting. F) Petrologic settings of analysed zircons from DD71710-2b with ages > 45 Ma. UHP garnet = zircon included in UHP garnet; OI = zircon included in omphacite; MX = matrix zircon. G) Petrologic settings of analysed zircons from DD71710-2b with ages < 45 Ma. AMP = zircon included in amphibole. H) Petrologic settings of analysed zircons from CM71710-4 with ages < 45 Ma I) Petrologic settings of analysed zircons from CM71710-4 with ages > 45 Ma.

Table A3. UHP age vs. timing of collision. The timing of collision can be estimated from the age of UHP metamorphism (see examples from Leech et al., 2005; Guillot et al., 2007). The collision age is predicted as a function of UHP depth, UHP age, the convergence rate, and slab dip. This table shows an example of such a calculation, using the simplified equation below from Leech et al. (2005). 100 km is the assumed depth of UHP metamorphism, UHP age estimates are consistent with new results, convergence rates bracket the fastest and slowest rates between 52 Ma and 46 Ma from White and Lister (2012), and single slab dips are assumed. The table yields a maximum collision age of 50.1 Ma, but other assumed slab geometries could increase this estimate by ~1 m.y. (cf. Leech et al., 2005; Guillot et al., 2007). Therefore we interpret the maximum collision age to be ~51 Ma. The minimum collision age is ~47 Ma, i.e., collision cannot post-date eclogite facies metamorphism. The maximum collision age is determined assuming the preserved UHP material represents the leading edge of the subducting continent; all interpretations rest on the assumption that the over-riding plate was Asia (rather than an island arc or micro-continent).

$$\text{Timing of Collision} = \frac{\text{Depth of UHPM}}{(\text{Convergence Rate} \times \text{Sin}(\text{Slap Dip}))} + \text{Age of UHPM}$$

Depth of UHPM	Convergence Rate	Slab Dip	Collision Age (UHP at 46 Ma)	Collision Age (UHP at 47 Ma)
100	69	28	49.1	50.1
100	69	35	48.5	49.5
100	69	41	48.2	49.2
100	150	28	47.4	48.4
100	150	35	47.2	48.2
100	150	41	47.0	48.0

APPENDIX B: CHAPTER 3 SUPPLEMENTAL TABLES

	Analysis	Elements (ppm)*		Isotopic Ratios				Apparent Age			
		U	Pb	$^{238}U/^{206}Pb$	±2σ error	$^{207}Pb/^{206}Pb$	±2σ error	$^{206}Pb/^{238}U$	±2σ error	$^{207}Pb/^{235}U$	±2σ error
DD080410-2b	1	8	90	125.5	6.9	0.09	0.017	51	3	93	26
	2	12	175	116.7	10.8	0.10	0.023	55	5	118	43
	3	8	217	84.0	21.9	0.19	0.069	76	19	280	130
	4	8	72	98.1	4.3	0.25	0.019	65	3	306	30
	5	8	6	114.0	4.7	0.15	0.015	56	2	165	18
	6	6	9	84.0	9.9	0.23	0.034	76	9	338	74
	7	7	5	112.4	6.8	0.13	0.014	57	4	146	26
	8	7	2	92.1	4.7	0.21	0.018	70	4	284	31
	9	9	5	117.9	8.2	0.08	0.013	54	4	97	25
	10	7	10	104.2	14.1	0.13	0.023	62	8	173	55
	11	9	8	122.5	12.9	0.08	0.027	52	5	101	50
	12	10	4	127.9	5.9	0.07	0.009	50	2	76	13
	13	8	4	127.6	6.0	0.07	0.010	50	2	77	18
	14	9	7	127.2	9.2	0.07	0.018	51	4	80	34
	15	8	1	122.1	6.1	0.09	0.010	53	3	101	20
	16	6	4	101.6	7.4	0.19	0.020	63	5	239	40
	17	6	26	119.2	8.7	0.09	0.017	54	4	112	33
	18	8	11	117.9	12.2	0.09	0.026	54	6	112	50
	19	5	61	108.2	2.9	0.17	0.009	59	2	192	10
	20	8	3	114.9	5.5	0.14	0.017	56	3	164	26
	21	16	-1	122.5	4.8	0.08	0.006	52	2	87	9
DD071910-1b	1	9	1	126.3	5.4	0.061	0.006	51	2	65	6
	2	8	1	138.1	6.1	0.064	0.007	47	2	62	6
	3	9	4	131.9	5.4	0.068	0.006	49	2	70	7
	4	4	3	135.3	11.4	0.060	0.018	47	4	61	20
	5	4	3	130.2	6.4	0.053	0.013	49	2	55	14
	6	4	3	130.4	5.3	0.066	0.008	49	2	69	9
	7	5	1	129.9	7.6	0.065	0.009	50	3	67	9
	8	5	1	128.7	5.8	0.055	0.008	50	2	58	8
	9	6	2	131.2	5.3	0.057	0.006	49	2	58	6
	10	6	2	137.0	6.6	0.057	0.007	47	2	55	6
	11	12	0	130.9	7.2	0.071	0.006	49	3	72	7
	12	12	-1	122.0	5.4	0.068	0.007	53	2	74	7
	13	11	0	126.4	5.8	0.069	0.005	51	2	73	6
	14	7	4	128.4	6.1	0.063	0.007	50	2	65	8
	15	7	4	141.8	9.9	0.062	0.010	45	3	60	10
	16	7	4	129.9	6.6	0.066	0.010	49	3	69	11
	17	7	2	133.7	6.3	0.065	0.005	48	2	66	6
	18	7	5	130.7	8.9	0.064	0.007	49	3	66	8
	19	6	4	127.9	6.5	0.072	0.010	50	3	75	10
	20	7	7	132.8	6.5	0.059	0.006	48	2	61	8
	21	6	7	131.4	7.8	0.073	0.015	49	3	77	21
	22	7	9	131.6	7.8	0.073	0.010	49	3	74	8
	23	6	9	130.0	14.2	0.071	0.015	49	5	74	19
	24	7	8	135.1	8.2	0.063	0.012	48	3	63	14
	25	6	8	137.7	5.5	0.057	0.007	47	2	56	8
	26	7	7	135.5	4.2	0.064	0.007	47	2	65	7
	27	7	7	144.7	6.1	0.064	0.008	44	2	60	8
	28	7	7	145.3	5.3	0.061	0.005	44	2	57	5
	29	7	3	143.5	7.6	0.057	0.006	45	2	53	6
	30	6	3	143.1	6.8	0.064	0.007	45	2	61	7
	31	8	7	130.2	6.1	0.064	0.006	49	2	67	8
	32	9	5	132.6	4.6	0.059	0.005	48	2	60	5
	33	8	28	135.0	10.2	0.069	0.010	48	4	68	9
	34	7	28	127.7	7.3	0.064	0.008	50	3	68	11
	35	11	0	131.4	5.0	0.057	0.006	49	2	58	6
	36	7	2	132.5	6.5	0.059	0.007	49	2	60	7
	37	7	1	133.9	7.2	0.067	0.014	48	3	69	18
	38	7	2	127.9	6.5	0.062	0.006	50	3	65	7
	39	7	2	130.4	5.9	0.053	0.006	49	2	55	6
	40	6	2	129.9	5.7	0.050	0.010	50	2	51	9
	41	8	3	124.1	7.2	0.060	0.006	52	3	65	8
	42	8	3	126.6	6.9	0.069	0.008	51	3	73	9
	43	7	3	137.9	4.6	0.060	0.006	47	2	59	7
	44	8	2	122.1	6.1	0.063	0.006	53	3	68	5
	45	8	2	138.7	7.3	0.056	0.008	46	3	56	11
	46	7	0	130.0	5.2	0.061	0.005	49	2	63	5
	47	8	4	133.5	8.7	0.072	0.008	48	3	72	8
	48	8	1	130.2	7.6	0.066	0.007	49	3	69	9
	49	8	2	136.1	5.2	0.059	0.005	47	2	59	6
	50	8	1	131.9	4.7	0.057	0.004	49	2	59	5
	51	9	2	130.7	5.8	0.063	0.007	49	2	66	10
	52	8	1	130.9	6.3	0.063	0.008	49	2	67	12

* No thorium values were detected.

Table 2. Summary of LA-ICP-MS analysis of U-Pb isotopes in titanite from sample DD71710-1c in the Tso Morari Geiss Dome

	Elements (ppm)			Isotopic Ratios					Apparent Age			
Analysis	U	Th	Pb	$^{232}Th/^{238}U$	$^{238}U/^{206}Pb$	±2σ error	$^{207}Pb/^{206}Pb$	±2σ error	$^{206}Pb/^{238}U$	±2σ error	$^{207}Pb/^{235}U$	±2σ error
1	25	1	0	0.030	38.04	1.20	0.625	0.017	167	5	1190	27
2	187	17	8	0.091	20.33	0.78	0.724	0.015	309	12	1790	36
3	78	5	3	0.059	24.81	0.86	0.717	0.015	255	9	1608	32
4	228	17	7	0.077	25.71	1.52	0.696	0.016	245	14	1537	49
5	281	20	3	0.069	60.17	1.48	0.517	0.011	106	3	776	14
6	33	1	1	0.026	24.88	1.05	0.683	0.016	254	11	1569	34
7	316	23	3	0.072	60.72	1.84	0.511	0.011	105	3	767	16
8	252	18	3	0.070	53.76	1.94	0.537	0.011	119	4	865	21
9	252	18	4	0.070	46.73	2.84	0.558	0.014	136	8	966	44
10	292	21	3	0.073	57.64	1.79	0.518	0.011	111	3	803	18
11	235	13	10	0.057	20.28	0.58	0.725	0.015	310	9	1783	24
12	218	12	11	0.055	17.83	0.70	0.740	0.015	352	14	1910	34
13	204	17	4	0.081	37.02	1.18	0.646	0.014	172	5	1242	23
14	250	18	3	0.072	50.86	1.73	0.545	0.012	126	4	920	22
15	339	25	3	0.074	66.09	1.88	0.479	0.010	97	3	704	15
16	240	18	4	0.073	43.59	1.54	0.612	0.013	146	5	1095	25
17	301	22	3	0.072	61.20	1.57	0.503	0.011	105	3	774	15
18	290	20	6	0.069	36.82	1.02	0.638	0.013	173	5	1244	21
19	309	20	3	0.063	61.61	1.67	0.501	0.011	104	3	769	15
20	278	11	4	0.038	49.12	1.69	0.569	0.012	130	4	977	22
21	299	21	3	0.070	58.48	1.64	0.518	0.011	109	3	823	16
22	296	7	5	0.024	45.07	1.28	0.591	0.012	142	4	1062	19
23	244	7	8	0.027	25.25	0.77	0.694	0.014	250	7	1606	25
24	300	20	4	0.067	47.37	1.39	0.572	0.012	135	4	1015	19
25	315	21	3	0.068	60.02	1.55	0.506	0.011	107	3	786	14
26	322	22	4	0.068	48.71	1.61	0.559	0.012	131	4	969	22
27	304	22	3	0.071	58.31	1.46	0.512	0.011	110	3	813	15
28	289	19	15	0.066	16.81	0.54	0.738	0.015	372	12	1993	28
29	306	20	5	0.067	40.65	1.65	0.609	0.013	157	6	1144	30
30	205	30	11	0.145	16.72	0.87	0.735	0.016	374	19	1973	49
31	307	20	7	0.064	35.24	1.01	0.641	0.013	180	5	1281	22
32	272	7	4	0.024	48.76	1.33	0.573	0.012	131	4	992	17
33	306	10	3	0.033	59.56	1.67	0.507	0.011	107	3	799	17
34	355	23	3	0.063	65.88	2.08	0.473	0.010	97	3	703	17
35	237	4	5	0.018	37.09	0.89	0.630	0.013	172	4	1232	17
36	294	20	3	0.067	58.28	1.60	0.518	0.011	110	3	817	18
37	84	2	6	0.027	12.77	0.52	0.758	0.016	488	19	2270	38
38	310	17	5	0.054	41.61	0.94	0.600	0.012	153	3	1115	16
39	366	22	3	0.059	61.27	1.54	0.493	0.010	104	3	765	15
40	152	6	13	0.042	11.36	0.36	0.779	0.016	543	17	2396	28
41	315	22	3	0.071	61.65	1.63	0.501	0.011	104	3	763	15
42	201	16	6	0.079	28.74	0.83	0.668	0.014	220	6	1456	24
43	288	19	3	0.067	56.40	1.40	0.530	0.011	113	3	847	15
44	204	15	5	0.076	31.28	0.76	0.673	0.014	203	5	1403	21
45	218	11	6	0.052	30.86	0.94	0.663	0.014	206	6	1394	24
46	195	14	12	0.070	15.06	0.50	0.764	0.016	414	13	2093	31
47	253	17	4	0.065	41.70	1.30	0.594	0.013	153	5	1082	22
48	199	12	3	0.061	43.48	1.30	0.603	0.013	147	4	1067	21
49	103	8	6	0.076	15.31	1.03	0.752	0.017	407	26	2053	65

APPENDIX C: CHAPTER 4 SUPPLEMENTAL FIGURE

Appendix Figure 4.1 Cross sections of Transect AB, CD and EF

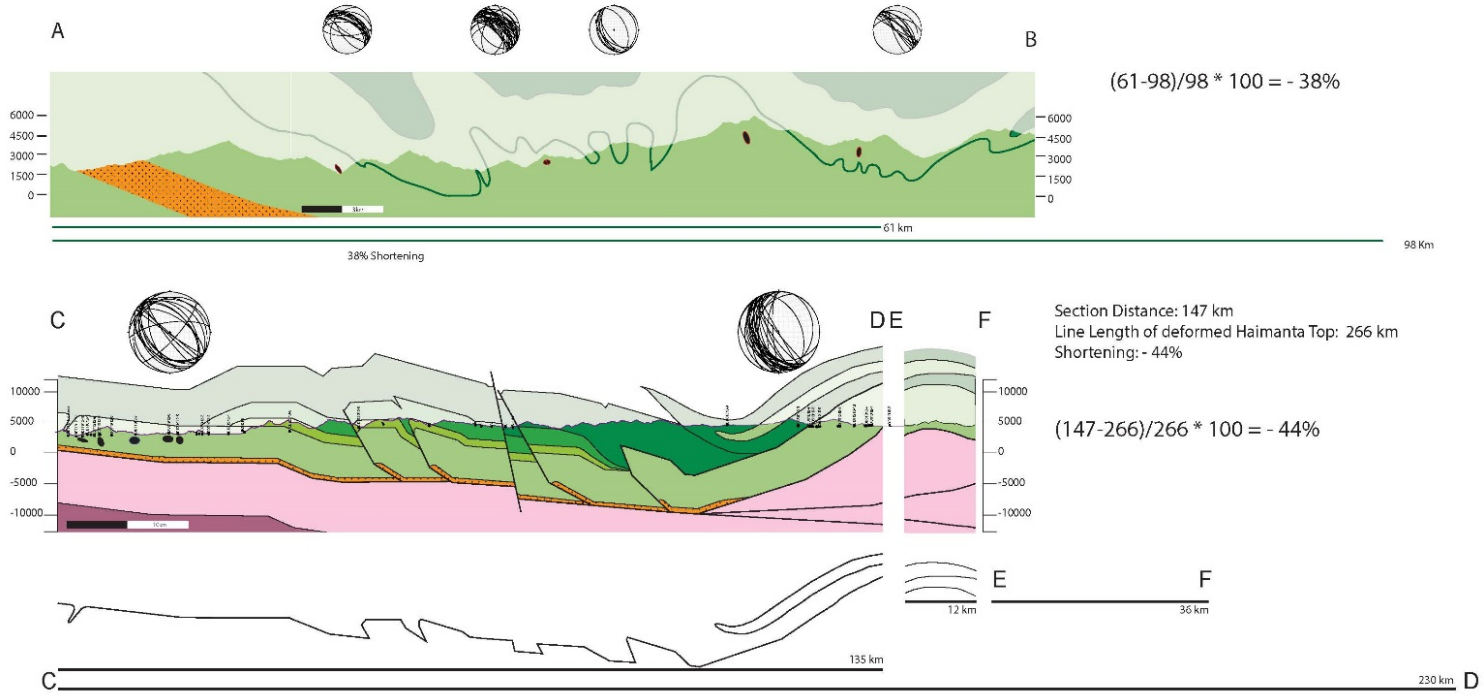

VITA

Dennis Donaldson was born in 1985, in Stuttgart, Germany. After various military related relocations his family and he finally settled in central Virginia. After graduating high school in 2003, he enrolled Virginia State University, where he earned a Bachelor of Science degree in physics in 2009. In August, 2009 following his undergraduate studies, he entered the Ph.D. program with structural geology and tectonics research group at Louisiana State University. He has been a research assistant in the group for six years. During his Ph.D. study he has held summer internships with National Energy Technology Laboratory, operated by the Department of Energy's Office of Fossil Fuel. Upon completion of his Ph.D. program, Dennis will continue working with the National Energy Technology Laboratory.